frontiers in Earth Science

ORIGINAL RESEARCH
published: 29 March 2022
doi: 10.3389/feart.2022.813396

Late Glacial and Holocene Palaeolake History of the Última Esperanza Region of Southern Patagonia

Stephen J. Roberts[1], Robert D. McCulloch[2], Joseph F. Emmings[3], Sarah J. Davies[4], Wim Van Nieuwenhuyze[5], Mieke Sterken[5], Katrien Heirman[6], Jeroen Van Wichelen[5,7], Carolina Diaz[8], Evelien Van de Vyver[5,9], Alex Whittle[1], Wim Vyverman[5], Dominic A. Hodgson[1] and Elie Verleyen[5]*

[1]British Antarctic Survey, Natural Environment Research Council, Cambridge, United Kingdom, [2]Centro de Investigación en Ecosistemas de la Patagonia (CIEP), Coyhaique, Chile, [3]British Geological Survey, Nottingham, United Kingdom, [4]Department of Geography and Earth Sciences, Aberystwyth University, Aberystwyth, United Kingdom, [5]Protistology and Aquatic Ecology, Ghent University, Gent, Belgium, [6]TNO—Geological Survey of the Netherlands, Utrecht, Netherlands, [7]Research Institute for Nature and Forest, Herman Teirlinckgebouw, Brussels, Belgium, [8]Institute of Ecology and Biodiversity (IEB), Universidad de Chile, Santiago, Chile, [9]Flanders Environment Agency, Aalst, Belgium

OPEN ACCESS

Edited by:
Bethan Joan Davies, Royal Holloway, University of London, United Kingdom

Reviewed by:
Patricio Iván Moreno, University of Chile, Chile
Olga Solomina, Institute of Geography (RAS), Russia

****Correspondence:***
Stephen J. Roberts
sjro@bas.ac.uk

Specialty section:
This article was submitted to Quaternary Science, Geomorphology and Paleoenvironment, a section of the journal Frontiers in Earth Science

Received: *11 November 2021*
Accepted: *10 February 2022*
Published: *29 March 2022*

Citation:
Roberts SJ, McCulloch RD, Emmings JF, Davies SJ, Van Nieuwenhuyze W, Sterken M, Heirman K, Van Wichelen J, Diaz C, Van de Vyver E, Whittle A, Vyverman W, Hodgson DA and Verleyen E (2022) Late Glacial and Holocene Palaeolake History of the Última Esperanza Region of Southern Patagonia. Front. Earth Sci. 10:813396. doi: 10.3389/feart.2022.813396

We undertook multi-proxy analyses on two sediment cores from Lago Pato, a small lake basin at 51°S topographically separated from Lago del Toro in Torres del Paine (TdP), to provide insights into glacier dynamics and lake-level change in the TdP and Última Esperanza region over the last ~30,000 cal a BP (30 ka). Lago Pato is situated in a region overridden by the Southern Patagonian Ice Field during the Last Glacial and in a transitional climatic zone of Southern Patagonia sensitive to seasonal- to millennial-scale changes in the Southern Hemisphere Westerly Winds (SWW). Results show that a deep ice-dammed and enlarged palaeolake encompassed Lago del Toro and Lago Pato c. 30–20 ka after the ice had retreated from local-Last Glacial Maximum (l-LGM) limits at c. 48–34 ka and during the build-up to the global-Last Glacial Maximum (g-LGM), c. 26–19 ka. Gaps in both sediment records between c. 20–13.4 ka and c. 20–10 ka suggest hiatuses in sediment accumulation during the g-LGM and Antarctic Cold Reversal (ACR) readvances and/or removal by lake lowering or flushing during the Late Glacial–early Holocene. The palaeolake level dropped from >100 m a.s.l. to ~40–50 m a.s.l. towards the end of the ACR c. 13.4–13.0 ka, creating a shallower glaciolacustrine environment dammed by an ice tongue in the Estancia Puerto Consuelo–Última Esperanza fjord. Further lowering of the enlarged palaeolake level occurred when the ice thinned to <40 m a.s.l., eventually isolating Lago Pato from Lago del Toro and glaciogenic sediment input at c. 11.7 ka. After isolation, the ecology and water levels in Lago Pato became sensitive to regional climate shifts. The shallow, stable, and highly anoxic environment that developed after c. 11.7 ka is associated with weaker (or poleward shifted) SWW at 51°S and was replaced at c. 10 ka by an increasingly productive shallow-littoral lake with a variable lake-level and periodic shifts in anoxic-oxic bottom water conditions and ratios of benthic-planktonic diatoms. A more open *Nothofagus* forest, established at c. 8.6–7.5 ka, and more arid conditions c. 7.5–5.7 cal ka BP are linked to another phase of weaker (or poleward shifted) SWW at 51°S. More persistently wet conditions from c. 5.7 ka, with extensive closed *Nothofagus* forests and planktonic diatoms dominant, are associated

with stronger (or equatorward shifted) SWW over 51°S. The abrupt return of benthic-to-tychoplanktonic diatoms after c. 3 ka reflects enhanced SWW at 51°S. Increasingly stable lacustrine and littoral wetland conditions established in the last ~500 years reflect weaker SWW and lasted until recent decades.

Keywords: Last Glacial Maximum (LGM), palaeoclimate, palaeolimnology, glaciation, lake-level changes, Patagonia, Southern Hemisphere westerly winds (SWW)

1 INTRODUCTION

The Southern Patagonian Ice Sheet reached its local-Last Glacial Maximum (l-LGM) at c. 48 ka [48,000 calibrated (cal) years before present (BP), where the present is 1950 CE], during Marine Isotope Stage 3 (MIS 3) (**Figure 1**), with secondary readvances at c. 39 ka and 34 ka (García et al., 2018). Outlet glaciers extended offshore to the west onto the continental shelf of the Pacific and crossed eastwards into Argentina and eastern valleys and fjords of the Última Esperanza province. Ice-lobes from the Cordillera Paine extended out beyond the eastern end of Lago del Toro forming complex terminal moraine systems, scouring deep lake basins such as Lago del Toro, while reaching their maximum advance limits at the l-LGM (limit A_1 in **Figure 2A**) (Sagredo et al., 2011; García et al., 2012; García et al., 2014; García et al., 2018; Davies et al., 2020). At the global-Last Glacial Maximum (g-LGM), c. 26.5–19 ka, the Southern Patagonian Ice Sheet was more than 200 km wide and over 1800 km long, yet it reached only half its maximum Marine Isotope Stage 3 extent due to milder winters and drier conditions associated with a weaker, broader, and equatorward shifted Southern Westerly wind belt that extended into the mid-latitudes (McCulloch and Davies, 2001; Kaplan et al., 2007; Kaplan et al., 2008; García et al., 2014; Darvill et al., 2015; Glasser et al., 2017; García et al., 2018; Davies et al., 2020; McCulloch et al., 2020).

The Southern Hemisphere Westerly Winds (SWW) are one of the main drivers of the global climate system, regulating the capacity of the Southern Ocean to absorb or release CO_2 through diffusion and biological uptake at the surface (Hodgson and Sime, 2010; Marshall and Speer, 2012) (**Figure 1A**). Recent global warming is thought to have led to an intensification and/or poleward shift in the mean annual position of the core SWW belt, and this is either reducing (Le Quere et al., 2007) or increasing (Landschützer et al., 2016) the capacity of surface waters in the Southern Ocean to absorb atmospheric CO_2. The "reducing hypothesis" is supported by recent observational and palaeo data, which shows a substantial rise in CO_2 during the transition into the Holocene coincident with an increased ventilation of carbon from the deep Southern Ocean (Moreno et al., 2010; Fletcher and Moreno, 2012; Saunders et al., 2018), rising global sea levels (Spratt and Lisiecki, 2016), and rapid deglaciation of the South Patagonian Ice Field (Davies et al., 2020; Palacios et al., 2020).

Dating of moraines and shorelines; changes in basin topography (García et al., 2012; García et al., 2014; García et al., 2018); multi-proxy, isotopic, and pollen analysis of lake and marine sediment records (Huber et al., 2004; Fletcher and Moreno, 2012; Mayr et al., 2013; Zolitschka et al., 2013; Moreno et al., 2018; McCulloch et al., 2020; Moreno et al., 2021); and larger-scale regional data compilations (Glasser et al., 2008; Davies et al., 2020; Palacios et al., 2020) have been used to reconstruct past glacier extent and deglaciation in Patagonia (**Figure 3**), with many studies linking glacier advance and retreat to past changes in precipitation and SWW intensity and/or latitudinal position over Southern South America (**Figure 1**).

The Seno Última Esperanza province and the Parque Nacional Torres del Paine have a wide variety of outstanding glacial geomorphological features. Many palaeoenvironmental studies have also been undertaken in the region (**Figures 1**, **3**), but the timing, impact, and drivers of Late Glacial and Holocene deglaciation remain debated (Moreno et al., 2018; Davies et al., 2020). The lake level history of Lago del Toro and the Holocene vegetational history of the surrounding area are detailed and well-studied (**Figure 3**, reference nos. 7–15 for summary) (García et al., 2012; Solari et al., 2012; García et al., 2014; García et al., 2018; Moreno et al., 2018; Moreno et al., 2021). A large ice-dammed proglacial lake, palaeo-Lago Tehuelche, once covered Lago del Toro and Lago Sarmiento sometime after c. 38 ka but before c. 17.6–16.8 ka; that is, between the l-LGM and g-LGM (Sagredo et al., 2011; Moreno et al., 2012; García et al., 2014). After the g-LGM, another large ice-dammed palaeolake encompassed Lago del Toro as far south as the southern end of the Puerto Consuelo–Última Esperanza fjord between c. 18 and 10.2 ka (but possibly as late as c. 7.1 ka) (locations B_1, B_2 in **Figures 2A**, **3** reference nos. 7–10). This palaeolake has been associated with local glacier readvance stages B–D (Stages TDP-I–IV), phases of ice retreat associated with Meltwater Pulse 1A c. 14.7 ka, and following readvances during the Antarctic Cold Reversal (ACR: 14.5–12.9 ka) (Blunier et al., 1997; García et al., 2012; Solari et al., 2012; García et al., 2014; Davies et al., 2020).

Moraines along the northern shoreline of Lago del Toro, with maximum cosmogenic isotope ages of c. 24 ka, have been linked to the g-LGM advance, while ages of c. 14.5–12.5 ka from the innermost moraines to the north of Lago Sarmiento imply ice could have also readvanced to the eastern end of Lago del Toro during the ACR (García et al., 2014; Fogwill and Kubik, 2016; García et al., 2018). No post-LGM chronology has been established for these moraines or those along the southern margin of Lago del Toro, adjacent to Lago Pato (**Figures 2A,B**). Glacier advances were driven by the alignment of the SWW over 51–52°S, which persisted between c. 13.4 and 11.3 ka as ACR glaciers retreated, but then became weaker, more diffuse, or poleward shifted during the "Early Holocene Westerlies

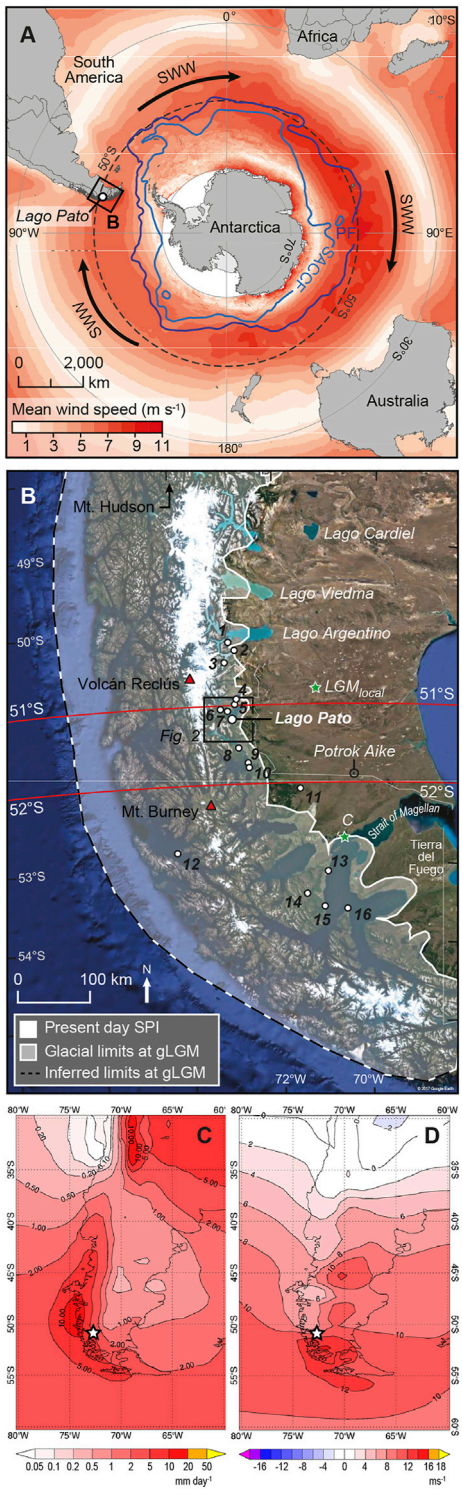

FIGURE 1 | (A) Location of Lago Pato in relation to the Southern Hemisphere Westerly Winds (SWW), the Southern Antarctic Circumpolar Current Front (SACCF), and the Polar Front (PF). **(B)** Location of Lago Pato, the extent of the global-Last Glacial Maximum (g-LGM) South Patagonian Ice Field, c. 20–25 ka (McCulloch et al., 2005; Davies et al., 2020). The green star marked LGM_{local} is the local-Last Glacial Maximum (l-LGM) (*Continued*)

FIGURE 1 | extent c. 48–34 ka (Glasser et al., 2008; García et al., 2014); the green star marked C is the ice-extent of Stage C advance in the Strait of Magellan (McCulloch et al., 2005). Red triangles are major volcanoes active during the Holocene. Key locations mentioned in the text and the sites of previous studies are as follows: 1, Peninsula Avellaneda; 2, Cerro Frías peat sequence; 3, Brazo Sur; 4, Vega Ñandú; 5, Pantano Margarita; 6, Lago Guanaco; 7, Meteorological Station; 8, Eberhard Site; 9, Pantano Dumestre; 10, Puerto Natales; 11, Río Rubens; 12, Lake Tamar; 13, Punta Arenas; 14, Puerto del Hambre; 15, Estancia Esmeralda II; 16, Isla Dawson. The background LANDSAT imagery in **(B)** courtesy of the U.S. Geological Survey (https://www.usgs.gov/centers/eros) generated in Google Earth, © Google. **(C,D)** ERA-INTERIM reanalysis (Dee et al., 2011) for **(C)** mean annual surface precipitation (mm per day; 1/6/1979–1/6/2017) and **(D)** zonal wind velocity (U on P at 850 hPa over the Andes; ms^{-1}; 1/6/1979–1/6/2017) over southern South America (30–60°S), covering the period up to when cores were taken from LP16. Lago Pato is located at the white star.

Minimum" (Mayr et al., 2013; Quade and Kaplan, 2017; Moreno et al., 2018; Zolitschka et al., 2018; McCulloch et al., 2020; Moreno et al., 2021).

To better understand changes in regional glacier dynamics and the nature and timing of climate changes, including the impact of changing SWW intensity over 51°S during the Late Glacial and Holocene, we present new data from two sediment records extracted from Lago Pato (S51°18.020′, W72°40.716′).

Lago Pato is a small, low altitude basin at 30–35 m a.s.l. located outside, but immediately adjacent to, moraines that run along the southern shoreline of Lago del Toro. It is located approximately mid-way between l-LGM and g-LGM maxima and present-day ice limits and in a transitional climatic zone east of the Andes (**Figures 1**, **2**). Previous studies and new geomorphological mapping of the area (**Figure 2**) show that Lago Pato would have been joined to Lago del Toro when lake levels were >40–50 m a.s.l. Using new geomorphological information collected in the field and high-resolution multi-proxy sedimentology and geochemistry (supported by fossil pollen and diatom evidence) from sediment records extracted from the present-day depocentre and a former littoral part of the basin within the catchment area of Lago Pato, we examine how regional deglaciation of the Última Esperanza region drove (palaeo) lake-level change within TdP. More specifically, we test the hypothesis that Lago Pato became isolated from Lago del Toro and glaciogenic sediment input when lake levels fell below the retaining sill following deglaciation and sometime after the Antarctic Cold Reversal (ACR: c. 14.6–12.8 ka). As Lago Pato is located within a transitional climatic zone east of the Andes, we also examine how deglaciation and isolation relate to broader climate changes during the Late Glacial and Holocene, particularly the variability of the SWW over ~51°S (as well as southern South America). Our key findings are summarised in **Figure 3** (reference no. 15) within the context of the existing glacial and climatic history of Southern Patagonia (reference nos. 1–14).

2 SITE DESCRIPTION AND BACKGROUND

Lago Pato is a relatively shallow (~4 m deep), well-mixed ellipsoidal freshwater lake, covering an area of approximately

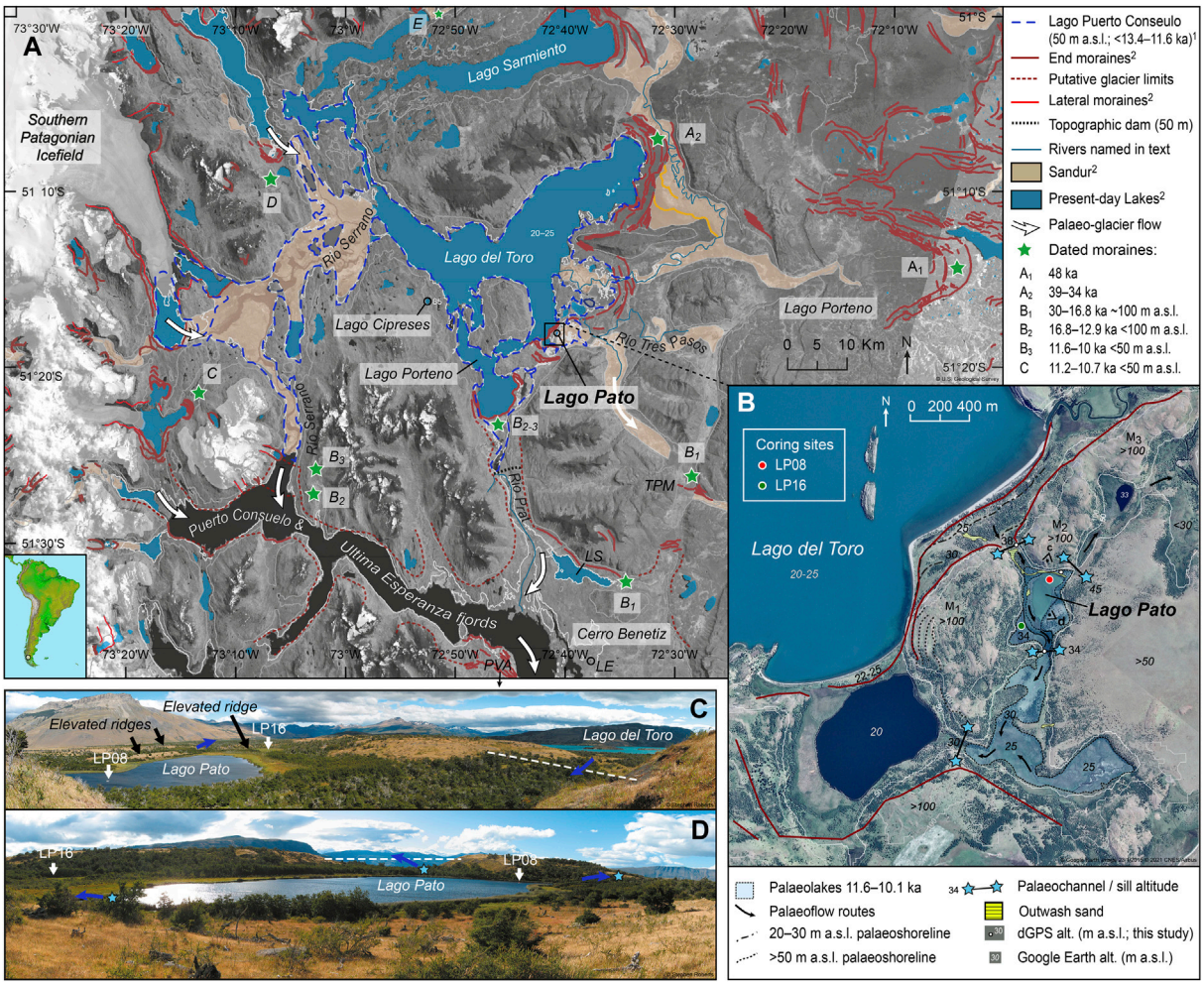

FIGURE 2 | (A) Location map highlighting key geomorphological features in the Torres Del Paine region [based on data in Glasser et al. (2008)]. The 50 m a.s.l. contour is shown as a dotted blue line. Green stars summarise the extent and age of former regional glaciations. 1, Garcia et al. (2014); 2, Glasser et al. (2008). Attribution: LANDSAT-8 satellite image was superimposed on the GEOTOP30 DEM in ARC-Map (www.esri.com), courtesy of the U.S. Geological Survey (https://www.usgs.gov/centers/eros). **(B)** Summary geomorphological sketch showing the ~40 m a.s.l. palaeoshoreline of Lago Pato and flow pathways and retaining ridges that would isolate Lago Pato from Lago del Toro (blue stars) as follows: 1) in the wetland to the south, separated by a sill elevation of 33.4 ± 0.1 m a.s.l.; 2) at 38.0 ± 0.1 m a.s.l., through a gap filled with outwash sand deposits between the prominent moraine complex that runs parallel with the southern shore of Lago del Toro to the northwest; 3) outflow breaching the northeastern sill at ~40–45 m a.s.l., requiring more substantial lake level rise of >10 m. Once the lake level in Lago del Toro dropped below ~40–38 m a.s.l., the only drainage route from Lago Pato was to the south, over the southern sill at ~32 m a.s.l. into the adjacent lake and Lago del Toro (~20–25 m a.s.l.). Areas to the south and southeast of Lago Pato, mapped as sandurs by Glasser et al. (2008), were visited during coring and interpreted as temporary wetlands that dry up during summer. LS is Lago Sofia, LE is Lago Eberhard, TPM is Tres Pasos Moraine, and PVA is Pantano Antonio Varas. Attribution: Google Earth, © Google.com, image 23/1/2015 © 2021 CNES/Airbus. **(C)** View from the northern side of Lago Pato showing the coring sites LP08 and LP16 and meltwater channels cut through the elevated moraine ridges on the NW and SE shores. **(D)** View looking towards the NE ridge and meltwater channel from the southern side of Lago Pato.

35,000 m^2 (~250 m × 130 m). It is located just outside the Parque Nacional Torres del Paine and on the eastern slopes of the Andes, on the southern shore of Lago del Toro (**Figure 2**). Both lakes are located to the east of the southern margin of the Southern Patagonian Ice Field and have been overridden and influenced by past glacial advances from the Cordillera Paine massif (**Figure 2A**).

Several outlet glaciers feed rivers that flow into Lago del Toro. However, Lago Pato, at ~33 m a.s.l., is currently an isolated and closed basin system with no direct glacial meltwater input. It is separated from the glaciolacustrine-influenced Lago del Toro, at 25 m a.s.l., by low-lying ridges at ~25–34 m a.s.l. to the south and east and elevated moraines, at ~ 38 m a.s.l., immediately to the north, northeast, and northwest (**Figures 2B–D**; **Table 1**). Former shorelines are clearly visible on the adjacent moraines and in the surrounding area on satellite imagery and are marked in the field by notable changes in catchment vegetation cover from grassland to dwarf shrubs (**Figures 2B–D**). Presently, the lake level in Lago del Toro is between 10 and 15 m below Lago Pato, depending on seasonal meltwater inputs into Lago del Toro (**Figure 2B**).

Lago Pato is located ~4–5° south of the region offshore in the Pacific Ocean where the present-day Antarctic Circumpolar

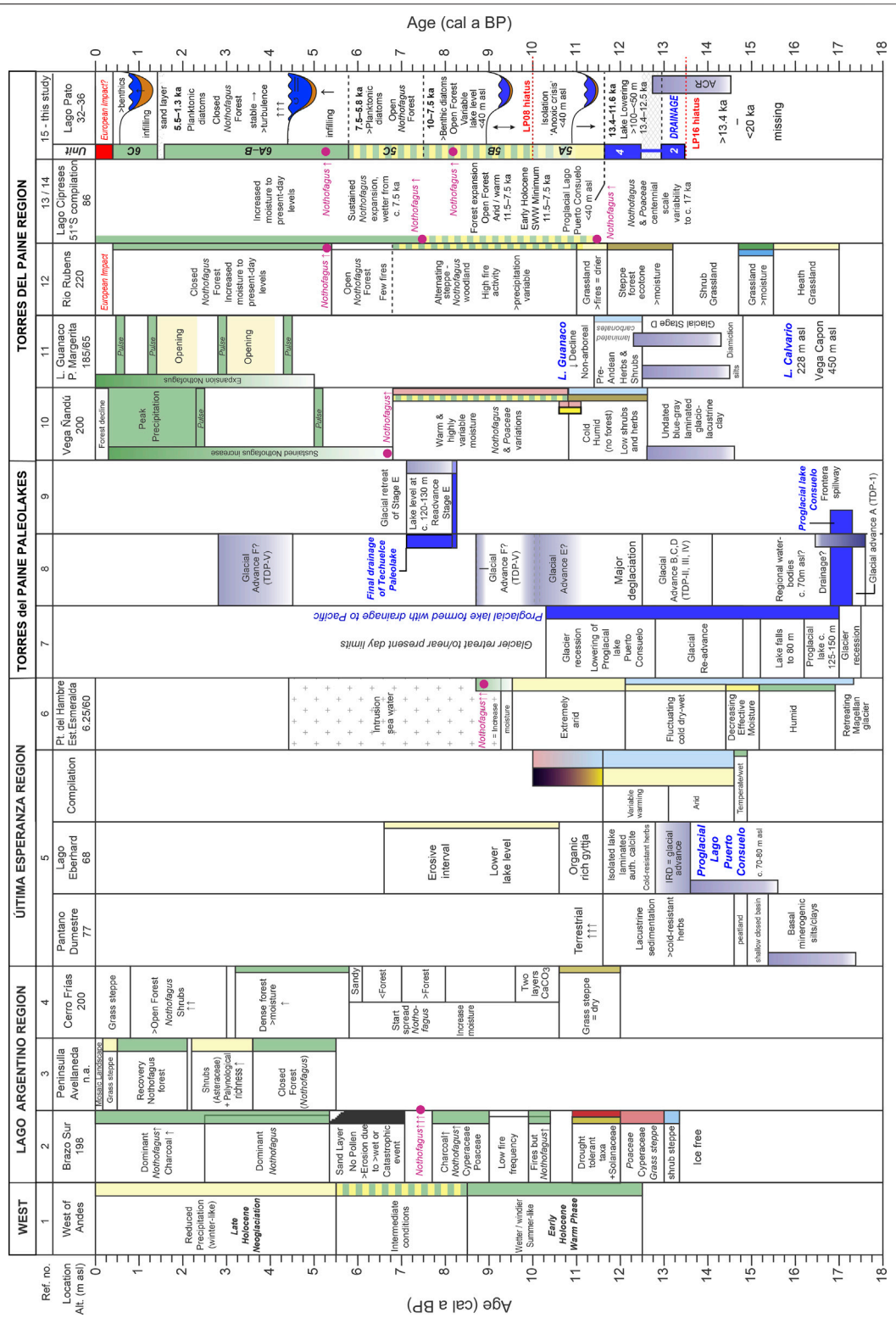

FIGURE 3 | Summary palaeoenvironmental interpretations for key studies from in Chilean Patagonia mentioned in the text (1–14). Summary findings from Lago Pato from this study are included in 15 for comparison. References: 1, Lamy et al. (2010); 2, Wille and Schäbitz (2008); 3, Echeverria et al. (2014); 4, Mancini (2009); 5, Moreno et al. (2012); 6, McCulloch and Davies (2001); 7, Sagredo et al. (2011); 8, García et al. (2014); 9, Solari et al. (2012); 10, Villa-Martínez and Moreno (2017); 11, Moreno et al. (2009a) and Moreno et al. (2009b); 12, Markgraf and Huber (2010); 13/14, Moreno et al. (2018) and Moreno et al. (2021); 15, this study.

TABLE 1 | Geomorphological data collected from Lago Pato. Data marked with an asterisk were calculated by subtracting the mean Google Earth offset (6.70 ± 5.95 m) from GPS measured data. Field measurements were undertaken using a Trimble 5700 GPS in December 2015, with a tripod height correction of 0.523 m using WGS84 as the reference ellipsoid, corrected using the EGM96 geoid model. Calculated elevations are shown to three decimal places, but the actual precision is, at best, one decimal place.

ID	Location description	Latitude (°S)	±2σ (m)	Longitude (°W)	±2σ (m)	WGS84 ellipsoidal height (m)	±2σ (m)	Geoid height (m)	Uncorrected elevation (m a.s.l.)	Corrected elevation (m a.s.l.)	Google Earth alt. (m a.s.l.)	Google Earth offset (m)
LP1	NW Sill to Lago del Toro 1	51°17′ 53.4218″	0.215	72°40′ 55.1173″	0.288	51.397	0.398	13.02	38.377	37.854	41	3.15
LP2	NW sill to Lago del Toro 2	51°17′ 53.4196″	0.044	72°40′ 55.1224″	0.097	51.508	0.145	13.02	38.488	37.965	41	3.04
LP3	LP16 coring site	51°18′ 11.3293″	0.059	72°40′ 53.6633″	0.107	46.682	0.112	13.01	33.672	33.149	40	6.85
LP4	S sill towards wetland	51°18′ 16.7246″	0.067	72°40′ 45.9815″	0.113	46.914	0.126	13.00	33.914	33.391	40	6.61
LP5	NE edge of Lago Pato	51°17′ 59.4762″	0.044	72°40′ 39.4845″	0.136	49.497	0.210	13.01	36.487	32.686	43	10.31
LP6	LP08 coring site	51°18′ 01.2000″	-	72°40′ 42.9600″	—	—	—	—	—	32.297*	39	—

Current (ACC) splits into equator- and pole-ward flows (Lamy et al., 2010; Caniupán et al., 2017), making it particularly sensitive to regional and spatial variations in the SWW-driven precipitation-evaporation balance over the Andes (**Figure 4**). Following post-glacial isolation, Lago Pato would have been a small, responsive lake located at the boundary with the eastern forest-steppe ecotone and in a transitional climatic zone between "wet" western and 'dry' eastern Patagonia. Our working hypothesis was that even relatively small changes in wind-driven precipitation in the past led to significant changes in lake level, lake ecology, and catchment vegetation cover.

2.1 Climate

Climate data from the Administración PN Torres del Paine Meteorological Station ~25 km from Lago Pato is characterised by a mean annual air temperature of 7.3°C (1964–2011 CE, 3 years after the LP08 core was taken), with minimum and maximum monthly averages of 3.6°C (in 1976 CE) and 9.1°C (in 1983 CE), mean annual precipitation of 817 mm a^{-1}, and mean annual wind speed (at ground level) of 24 km h^{-1}, predominantly from the W and NW (data from http://www.meteochile.gob.cl). In comparison, the mean annual precipitation along the west coast of Chilean Patagonia and western Andes is up to 7,000 mm a^{-1} but declines to 400 mm a^{-1} on the eastern steppe (Schneider et al., 2013). Temperature and precipitation anomaly profiles for TdP between 1979 and 2021 CE (compared to the 30-year mean between 1980 and 2010 CE) are shown in **Figure 4A**.

The Andean Cordillera creates an orographic barrier to the SWW (currently focussed at ~50–52°S) and a complex spatial (latitudinal) and temporal relationship between wind strength and precipitation (**Figures 1C**,D, **4B–I**). Analysis of weather station data has shown annual precipitation immediately east of the Andes, around Lago del Toro and Lago Pato, to have been neutral to slightly positively correlated to zonal wind flow over the high Andes (U on P at 850 mbar) over the last ~40 years (Garreaud et al., 2013; Schneider et al., 2013; Moreno et al., 2018). Studies combining weather station data and mesoscale modelling of the eastern Andean slopes have shown a more consistently positive correlation (Moreno et al., 2014; Moreno et al., 2018). Seasonally, there is only marginally more precipitation in the Última Esperanza region compared to winter (June–July–August, JJA) (**Figures 4B,D**), but the core SWW are stronger and more poleward shifted (south of 50–52°S) over Southern Patagonia during the Austral summer (December–January–February, DJF; **Figures 4C,E**). Consequently, zonal winds over the Andes have had a consistently neutral to negative correlation with precipitation at Lago Pato between 1979 and 2017 CE during the Austral summer. This relationship has become more negative over the last decade (2007–2017 CE; **Figures 4F,G**). In contrast, during winter, zonal winds over the Andes and precipitation over Lago Pato have been positively correlated over the last decade (**Figure 4H**), leading to a net neutral to negative annual correlation between precipitation and wind velocity (**Figure 4I**). At Lago Potrok Aike, ~175 km ESE of Lago Pato at 51°S, where the orographic effect of the Andes is reduced, easterly frontal system incursions are more prevalent, and winter precipitation can also increase when the SWW become weaker and/or when its core belt widens latitudinally (Garreaud et al., 2009; Fletcher and Moreno, 2012; Zolitschka et al., 2013).

Regionally, longer-term climate changes are controlled by the interplay between the changing strength and influence of interannual–millennial-scale climate drivers, such as the El Niño Southern Oscillation (ENSO) and the Southern Annular Mode (SAM), defined as the atmospheric pressure difference between the mid and high latitudes in the Southern Hemisphere (Garreaud et al., 2013). Decadal-scale variability in precipitation and temperature is evident in the TdP reanalysis data (**Figure 4A**). Positive phases of the SAM reflect warmer and drier conditions and higher pressure in the

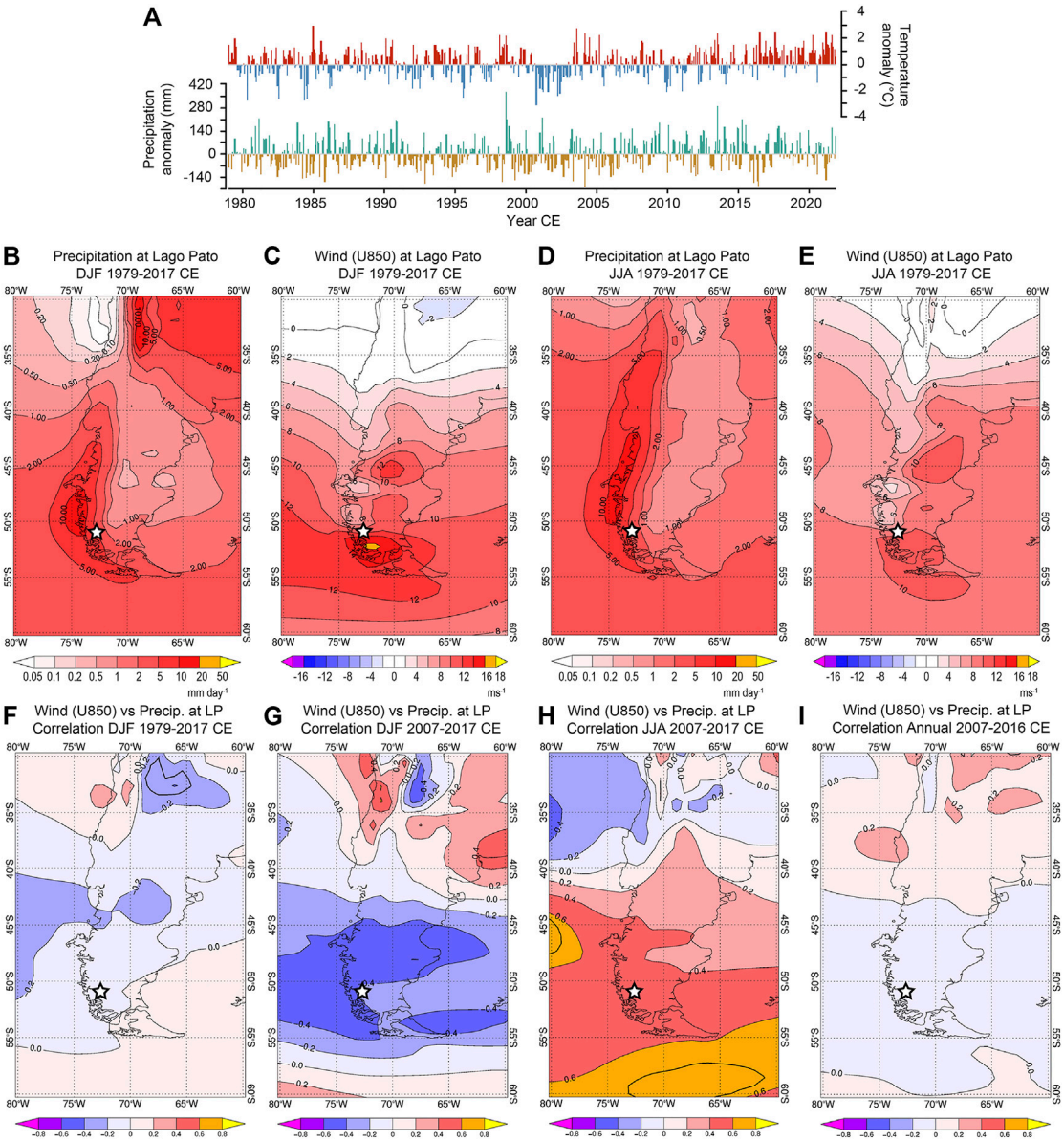

FIGURE 4 | (A) Temperature and precipitation anomaly data from Parque Nacional Torres del Paine meteorological station between 1979 and 2021. Data generated from and copyright of https://www.meteoblue.com, used here with permission. **(B–E)** ERA-INTERIM reanalysis (Dee et al., 2011) for mean Austral summer (December–January–February; DJF) and winter (June–July–August; JJA) mean surface precipitation (mm per day; 1/12/1979–1/3/2017) and zonal wind speed (U on P at 850-hPa over the Andes in ms^{-1}; 1/12/1979–1/3/2016) over southern South America (30–60°S) between 1979 and 2017 CE. The white star is the location of Lago Pato. **(F)** ERA-INTERIM reanalysis data showing neutral to marginally negative correlation coefficients between mean zonal wind velocity over southern South America and mean surface precipitation at Lago Pato for the austral summer (DJF) from 1/12 to 1/3 between 1979 and 2017 CE compared to **(G)** increasingly negative time mean correlation coefficients over Lago Pato for the austral summer (DJF) from 1/12 to 1/3 between 2007 and 2017 CE and **(H)** positive time mean correlation coefficients at Lago Pato for the austral winter (JJA) from 1/6 to 1/9 between 2007 and 2017 CE. **(I)** Time mean correlation coefficient map of annual mean wind velocity over southern South America (30–60°S) and annual mean precipitation at Lago Pato (white circle) between 1/12/1979 and 1/12/2016 CE. ERA-INTERIM data and maps were generated using a BAS internal portal to the Dee et al. (2011) dataset with the final layout made in Adobe Illustrator.

mid-latitudes (e.g., Patagonia) with lower pressures and stronger and more poleward shifted SWW (Marshall, 2003; 2007). In essence, the situation is analogous to the seasonal Westerlies (summer/winter) cycle in that the SWW are more intense and focused during positive (warmer) phases of the SAM (the current situation) and weaker, latitudinally broader, and less focussed during negative (colder) phases of the SAM (Perren et al., 2020).

Warming in recent decades has led to an increasingly positive Southern Annular Mode and a greater influence of the El Nino

Southern Oscillation (Marshall, 2003; Abram et al., 2014), with reduced precipitation and weaker Southern Westerlies in the high-to-mid-latitudes of southern South America (Garreaud et al., 2009). Similar processes are thought to occur over decadal–centennial and longer timescales, with an equatorward core SWW belt maintaining high lake levels in northern and eastern Patagonia between c. 51 ka and 9 ka (Zolitschka et al., 2013; Van Daele et al., 2016; Henríquez et al., 2021). Millennial-scale periodicities recorded in various proxy records are thought to be driven by changes in insolation and solar activity [e.g., the ~2.4–2.5 kyr Hallstatt cycle (Viaggi, 2021)], the planetary radiative imbalance (i.e., the amount of insolation absorbed versus the energy radiated back into space at the top of the atmosphere), internal ice sheet dynamics, and CO_2 outgassing, driven largely by changes in the SWW (Emile-Geay et al., 2007; Steinhilber et al., 2009; Baggenstos et al., 2019; Dickens et al., 2019; Henríquez et al., 2021; Shin et al., 2021; Evans et al., 2022).

2.2 Vegetation and Geology

Vegetation patterns in Southern Patagonia closely follow the sharp west-to-east precipitation gradient across the Andes, superimposed on latitudinal variations (Tuhkanen, 1992). As moisture-laden air masses cross the Andes, the hyper-humid region in the west transitions into a more arid steppe in the east. The western side of the Andes is dominated by Magellanic moorland communities and evergreen *Nothofagus* forests (southern beech), while the eastern slopes and those close to the Patagonian Ice Field are characterised by winter deciduous *Nothofagus* forests. The wider Provincia de Última Esperanza is a diverse eco-climatic region from hyper-humid in the west and arid in the east. Southern beech forests in western regions, with annual precipitation between ~450 and 1,000 mm a^{-1}, gradually merge into a transition zone of dry scrub and fescue grassland in regions with precipitation regimes below ~450 mm a^{-1} and finally become Patagonian steppe in drier eastern areas (Tuhkanen, 1992). Lago Pato is located just outside the Parque Nacional Torres del Paine, in the Comuna de Torres del Paine. As part of the Región de Magallanes, it is in an ecological transition zone between the *Nothofagus* dominated and steppe biomes, although the natural vegetation has been altered by agricultural and land management activity in and around Parque Nacional Torres del Paine and Lago Pato. The local geology is dominated by shales, intercalated by marls, sandstones, and conglomerates (Altenberger et al., 2003). The glaciated landscape of the Southern Patagonian Ice Sheet dominates the southern Andes and the Cordillera Paine massif to the west and northwest of Lago Pato.

3 METHODS

3.1 Geomorphology and Limnology

We measured the geoid-corrected elevation above sea level (m a.s.l.) of former lake shorelines and retaining moraine ridges around Lago Pato using a Trimble differential GPS (dGPS) accurate to down to 0.1 m with values quoted as ±two-sigma errors (**Table 1**). Other elevations were determined from "Google Earth" and are on average 6.7 ± 5.9 m (two-sigma) higher than the geoid-corrected dGPS field measurements; hence, we assigned ±10 m errors. Standard limnological properties (pH, conductivity, temperature, and dissolved oxygen) were measured in and around Lago Pato and other Southern Patagonian lakes with a YSI600 Sonde. Light penetration was measured with a Secchi disc and water samples for diatom and chemical analysis were taken at 1 m intervals in the water column.

3.2 Sedimentology, Geochemistry, and Chronology

Using a combination of a UWITEC-gravity corer, a Livingston piston corer, and a Russian corer, two sediment records were extracted from the deepest point (~3.5 m of water depth) in the lake—the 600 cm long LP08 record (S51° 18′01.2″, W72° 40′43.0″, 32 m a.s.l.)—and from a littoral wetland area—the 295 cm long LP16 record (S51°18′11.3″, W72° 40′53.7″, 33–34 m a.s.l.) (**Figure 2A**; **Table 1**). A surface gravity core from the LP08 site was sliced at 0.5 cm (0–20 cm) and 1 cm (20–41 cm) intervals in the field. Livingston piston cores (LP08) and Russian cores (LP16) were retained intact.

Intact cores were split in the laboratory and analysed for physical properties with a Geotek® multi-sensor core logger (MSCL) (Gunn and Best, 1998) to obtain gamma-ray wet density (ɣ-density or GRD), resistivity, and magnetic susceptibility (MSκ; SIx10^{-5}) data (Bartington Instruments; LP08: MS2C loop sensor, 2 mm intervals, 10 s; LP16: MS2E point sensor, 0.5 mm intervals; 10 s) and density-corrected MSχ (κ/ρ; kg m^{-3}). Digital X-radiographs were obtained from split cores using a rotating anode mobile digital Celtic SMR CR computerised X radiography unit at Cambridge University Vet School (48 kV; 4 mAs; no grid) and as ITRAX™ digital X-radiographs (45 kV, 50 mA.ms, 200 ms, 60 μm interval) at Aberystwyth University. Contiguous downcore wet-sediment Energy Dispersive Spectrometry (EDS) X-ray fluorescence core scanning (XRF-CS) geochemistry data were obtained using the ITRAX™ XRF core scanner fitted with a Molybdenum (Mo) anode X-ray tube (settings: 30 kV, 50 mA, count time 10 s). Machine and sample calibration was undertaken using a synthetic glass standard and XRF fused glass discs from the Ardley Lake and Yanou Lake sediment cores (Roberts et al., 2017) with similar compositional variability at the start and end of each core-site run. Measurements were made at 2 mm contiguous intervals for LP08 (equivalent to mean ± two-sigma: 4.5 ± 7 years), with duplicate scans undertaken at 200 μm intervals for LP08 Unit 1 (1.3 ± 4.2 years) and at 100 μm for the basal LP08 Unit 1 core section. LP16 Units 3–6 were scanned at 500 μm (9.6 ± 17.4 years) and LP16 Units 1-2 at 200 μm (1.1 ± 1.6 years). Data from finely laminated glaciolacustrine sediments in Units 1-2 were measured at, or smoothed to, 200 μm (from 100 μm interval data).

Raw count per second (cps) XRF-CS data were analysed using the Q-spec software v8.6.0 (Cox Analytical), with MSE values minimised to optimise the fit of the "as-measured" spectra to

TABLE 2 | Summary descriptions and interpretations of the lithofacies units in the Lago Pato LP08 and LP16 records.

Record	Unit subunit	Depth (cm)	Modelled age range (cal a BP ± 95% CI)	Summary lithological description	Summary interpretation	Lake history and palaeoclimate SWW position and movement
LP08	1	600–470	29,800 ± 1,020 to 21,230 ± 520	Light grey, finely laminated glaciolacustrine silty clay with pale greyish-orange layers enriched in Ti and Ca. The lowermost laminated sub-unit (1A) grades into a paler green-grey massive sub-unit (1B). In LP08, a sharp erosional upper boundary separates Unit 1 and Unit 5B at 470 cm. Units 2–5A are missing from LP08. In LP16, step changes to lower MS values separate sub-units 1A and 1B at 187 cm (25.5 cal ka BP) and Units 1 and 2 at ~110 cm (20.4 cal ka BP)	Unit 1 represents the 'background' glaciogenic detrital composition, with well-developed fine scale internal structure, most notably within Unit 1A, and dominated by glaciogenic physical weathering products associated with allochthonous catchment erosion. Fine grey (glaciogenic) laminations are enriched in Fe and Mn, reflecting reduced conditions and/or the decomposition of organic matter at the sediment-water interface	Lago del Toro and Lago Pato were part of a larger proglacial Palaeo-Lago Tehuelche after the l-LGM and before the g-LGM Lago Pato was overridden at the g-LGM SWW: N of 51°S, limited latitudinal movement in run-up to g-LGM
LP16		295–112 (112–110 hiatus)	27,530 ± 270 to 20,490 ± 350			
LP16	2	110–83	13,390 ± 640 to 13,060 ± 390	Unit 2 has similar sedimentological characteristics to the upper parts of Unit 1 but is distinguished by the lack of well-defined orange-brown banding and the presence of embedded fine subaquatic *Myriophyllum* sp. fragments	Glaciogenic physical weathering products associated with allochthonous catchment erosion. Embedded sub-aquatic macrofossils imply a shallower environment than Unit 1	First substantial lake level reduction at c. 13.4 ka: shallow, >productive lake (lake level: >100 m asl → <50 m asl) SWW: At 51°S, moving S from ACR SWW peak north of 51°S at c. 13.5 ka
LP16	3	83–74	13,070 ± 390 to 12,500 ± 220	Unit 3 is composed entirely of subaquatic *Myriophyllum* sp.	Shallower and more productive glaciogenic environment	A further reduction in lake level between c. 13.0 and 12.5 cal ka BP following glacier retreat after the ACR. SWW: S of 51°S, moving S
LP16	4	74–67	12,500 ± 220 to 11,720 ± 280	Unit 4 has a similar composition to Unit 2 but has increasingly elevated Ca and Sr and a reduced density of subaquatic *Myriophyllum* sp.	Shallower and more productive glaciogenic environment with authigenic precipitation (or redeposition) of Ca-, Sr-rich deposits. Still connected to Lago del Toro	Gradual refilling of Lago Pato while still connected to Lago del Toro SWW: S 51°S, moving N
LP16	5A	67–47	11,720 ± 280 to 10,120 ± 190	Unit 5 is structureless organic lake mud characterised by fluctuating Fe/Mn and Mn/Ti, with Ca and S peaks. Subunits 5A–C in LP16 characterised by exceptionally elevated (>+2-sigma) Fe/Mn and Mn/Ti between c. 11.7–10 cal ka BP (Unit 5A) and c. 8.4–7 cal ka BP. Subunits 5B and C are characterised by lower but still elevated Fe/Mn and Mn/Ti ratios and higher C/N values than Unit 1. Elevated Fe/Mn ratios reflecting minerogenic input are correlated with Mn/Ti ratios	Shallow-littoral environment isolated from glaciogenic inputs from Lago del Toro at 11.7 ka. Unit 5A represents an 'Anoxic Crisis' with the eventual loss of benthic diatoms within the lake. Units 5B and C represent a more restricted shallow and productive basin, with increased input of terrestrial vegetation ad periodic oxic phases consisting of Mn-oxides and co-precipitated hydroxides	Second major lake level reduction at c. 11.7 cal ka BP, continuing until complete isolation from Lago del Toro at c. 11.3 cal ka BP (lake level: <50 m asl → <40 m asl). Erosional and overspill/flushing events (or, less likely, palaeolake reformation and emptying) at c. 10 ka and c. 8.9–8.6 ka? SWW: S 51°S, moving N back over 51°S by 8 ka
	5B/C	47–35	10,120 ± 190 to 5,720 ± 130			
LP08	5B	470–378	10,160 ± 480 to 7,370 ± 290			
	5C	378–324	7,370 ± 290 to 5,600 ± 250			
LP08	6A	324–175	5,600 ± 250 to 3,310 ± 330	Highly organic, structureless, and increasingly fibrous macrophytic lake mud with low Mn/Ti ratios divided into subunits at 175 cm by a reduction in Mn (6B) and at 45 cm by a ~15 cm thick Sr-rich inwash sand layer (6c)	Significant Mn enrichment, with sporadic Mn and Ca peaks implying that Lago Pato was occasionally shallow and highly anoxic well into the mid Holocene. Increasing Fe/Mn ratios reflect a general increase in anoxia linked to greater stability and lake infilling	Shift to more persistently wet conditions with increased turbulence in the last 2 ka. LP16 became a subaerial environment in the last 200 years. SWW: marginally north of 51°S and generally stable; increased ENSO influence
	6B	175–45	3,310 ± 330 to 1,380 ± 130			
LP16	6A–C	45–0	1,380 ± 130 to −60 ± 3			
	6A–C	35–0	5,720 ± 130 to −10 ± 1			

modelled spectra. Element and scatter cps were normalised by total scatter cps (incoherent (Compton) scatter + coherent (Rayleigh) scatter; inc.+coh.) as element/inc.+coh. (Kylander et al., 2011). Data are presented as percentages of the total scatter normalised ratio sum [%∑TSN or, more simply, %TSN (Roberts et al., 2017)], equivalent to percentages of the cps sum (or %cps), to account for downcore variations in count rate, density, water, and organic content and to investigate covariance, closed-sum effects between elements and scatter parameters, and the non-stationarity and equifinality of geochemical responses through time (Tjallingii et al., 2007). Data less than mean minus two-sigma kcps (mainly due to gaps in the core) and greater than MSE plus two-sigma (representing a poor fit between measured to modelled spectra) were filtered before analysis. 'Noisy' and poorly measured elements were eliminated by comparing cps and using %TSN thresholds of >0.1% mean and >0.5% maximum and examining autocorrelation profiles for each element (Bishop, 2021). This left 12 'well-measured' elements for the LP08 record (Si, S, K, Ca, Ti, Mn, Fe, Zn, Br, Rb, Sr, Zr, and inc., coh. scatter) and 17 'well-measured' elements for the LP16 record (Si, S, K, Ca, Ti, V, Cr, Mn, Fe, Ni, Zn, As, Br, Rb, Sr, Zr, Ba, and inc., coh. scatter) (see the Supplementary Material for details).

Centred element log ratios (clr) and log element ratios of XRF-CS can produce similar downcore profiles to quantitative (Wavelength Dispersive Spectroscopy, WDS-XRF) analysis of dry and organic free samples (Weltje and Tjallingii, 2008; Davies et al., 2015; Roberts et al., 2017; Dunlea et al., 2020). Therefore, the key elements used in interpretations (S, Ca, Ti, Mn, Fe, Br, and Sr) are presented as natural log (i.e., log-n or Ln) ratios of cps data or their Z-scores (i.e., centred around the mean and standardised by subtracting the mean from observed values and dividing by the 1σ). As Al is not well-measured using an ITRAX^{TM} XRF core scanner with a Mo-tube (Löwemark et al., 2011), Ti-normalised log-n ratios were used to estimate elemental variations relative to the background bedrock input (Weltje and Tjallingii, 2008; Kylander et al., 2011; Davies et al., 2015; Roberts et al., 2017; Saunders et al., 2018).

Core sections were aligned into composite records from field depth measurements from visual stratigraphy, bulk density, MS, XRF-CS data, and, for LP08, subsample data (loss-on-ignition (LOI), and total organic carbon (TOC)), and using AnalySeries (Paillard et al., 1996).

A chronology for each record was established using Accelerator Mass Spectrometry (AMS) radiocarbon dating of 21 samples from the LP08 record and 15 samples from the LP16 record. Identifiable macrofossils were dated preferentially, but where bulk samples were the only option, we avoided intervals likely to contain significant authigenic carbonate, characterised by exceptionally elevated Ca, Sr, and/or Mn in XRF-CS profiles. Calibration of radiocarbon ages was undertaken in OXCAL v.4.4 (Bronk Ramsey, 2016) using the SHCal20.14C Southern Hemisphere atmosphere calibration dataset (Hogg et al., 2016; Hogg et al., 2020). Radiocarbon ages are reported as conventional radiocarbon years BP (^{14}C years BP) ±1σ and calibrated ages as 2σ (95.4%) ranges, median and mean calendar years BP (cal a BP and cal ka BP, relative to 1950 CE), rounded to the nearest 10 years. Age-depth models for both records were developed using Bayesian age-depth modelling software (BACON v.2.5) (Blaauw and Christen, 2011), incorporating a hiatus of 10,000 years at 470 cm in LP08 and 7,000 years at 110 cm in LP16 between Unit 1 and its overlying deposits (**Supplementary Figure S1**). Ages are rounded to the nearest 10 calendar years (cal a BP) in **Section 4** and to the nearest 100 years (0.1 cal ka BP) in the **Section 5** to reflect dating and age-depth modelling uncertainties.

Units with common characteristics were identified using constrained CONISS cluster analysis with broken stick on square root transformed 2 mm and 1 cm interval smoothed % TSN XRF-CS geochemical data and as-measured 1 cm interval diatom and pollen datasets. To establish provenance relationships, the Pearson product-moment correlation coefficient (PPMCC), multivariate principal components analysis (PCA), which reduces correlations between elements to the smallest set of linear combinations possible plotted on dimensionless axes, and discriminant hierarchical (k-means) cluster analysis, which uses a measure of statistical distance (dissimilarity) between multiple elements to generate groups, were applied to 12 'measurable' elements common to LP08 and LP16 (Si, S, K, Ca, Ti, Mn, Fe, Zn, Br, Rb, Sr, and Zr) and incoherent, coherent scatter parameters. Measured %TSN data were log-transformed, centred, and standardised as Z-scores prior to PCA.

Log-n element/Ti ratio XRF-CS Z-scores were used for time series analysis (Fast Fourier Transform, FFT, periodograms, Lomb–Scargle Power Spectrum, wavelet power spectrum, peak identification in MATLAB; **Figure 6**; **Supplementary Figure S6**) (Grinsted et al., 2004; Trauth, 2015). Equally spaced (10-year and 100-year) time intervals were generated for time series analysis using Piecewise Cubic Hermite Interpolated Polynomial (PCHIP) datasets, which avoids spline artefacts and preserves the shape of the original XRF-CS data series. Time series data were detrended (polynomial linear best fit) to remove the long-term linear trend. Second-order polynomial Locally Weighted Scatterplot Smoothing (LOESS) 100-year smoothing (0.1 sampling interval with outliers removed) was also used to compare datasets to published data.

3.3 Carbon, Diatom, and Pollen Analysis

Geochemical and sedimentological interpretations of the lake-level change in Lago Pato were inferred from multi-proxy analysis of the <10 cal ka BP organic deposits of Unit 6 in the LP08 record. This part of the LP08 was more highly resolved than the LP16 Holocene record and contained sufficient diatoms and pollen for quantitative analysis. Loss-on-ignition (LOI) (12 h drying at 110°C, 4 h at 550°C (LOI_{550}), and 2 h at 950°C for carbonate-proxy ($LOI_{950} \times 1.36$) (Heiri et al., 2001)), total organic carbon (TOC, $\%C_{org}$) and total nitrogen (%N) were determined at 1 and 4 cm intervals in the LP08 core. Bulk organic carbon isotopic ratios ($\delta^{13}C_{org}$), determined by combustion on a Costech EA interfaced with the VG Triple Trap and Optima IRMS at NIGL (NERC Isotope Geosciences Laboratory), were calculated to the V_{PDB} scale using a within-run laboratory standard calibrated against NBS-19 and NBS-22. Replicate analyses of sample material gave a precision of ±0.1 (per mil) for $\delta^{13}C_{org}$ and

10% for C/N. Flux data (g cm^{-2} a^{-1}) were calculated from the product of dry mass accumulation rates (g cm^{-2} a^{-1}) (as dry bulk density (g cm^{-3}) x sedimentation rate (cm a^{-1})) and proxy concentration measurements (Street-Perrott et al., 2007).

Subsamples for diatom and stomatocyst analysis were taken at 4 and 8 cm intervals from the LP08 core following standard preparation techniques (Renberg, 1990; Sterken et al., 2012). At least 400 valves were counted per slide, and species were identified to at least genus level using taxonomic studies from the region (Rumrich et al., 2000; Guerrero and Echenique, 2002). Where feasible, distinctions were made between different morphotypes of the small benthic fragilariod species (e.g., *Staurosirella* aff. *pinnata*; *Staurosira* aff. *venter*) because this can reflect different environmental conditions (Stevenson et al., 2008). No distinction was made between stomatocyst morphotypes.

Microscopic pollen, charcoal, and cryptotephra shards were counted at 8 cm intervals in the LP08 core (Moore et al., 1991) with *Lycopodium* spores of known concentration added for quantification (Stockmarr, 1971). The total pollen sum from each subsample is at least 300 land pollen grains (total land pollen, TLP) above 470 cm in the LP08 record (i.e., above the hiatus between Unit 1 and 5B). Local site indicators (e.g., obligate aquatic plants, moss spores, and algae) were calculated as TLP + taxon. Charcoal was classified into five different size classes, <25, 25–50, 50–75, 75–100, and >100 μm, to distinguish between proximal and distal fires, assuming hydrodynamic fractionation at the regional scale. Diatom and pollen data were obtained from the more highly resolved Holocene-age Unit 5 and 6 sediments of the LP08 record. Both proxies were largely absent from the basal glaciolacustrine deposits in Unit 1 of both records.

Data were analysed and figures constructed in R v. 4.1.0/ Rstudio v. 1.4.1717, using the R packages Vegan, Rioja, Tidyverse (ggplot2), Ggally v. 2.1.2 (Juggins, 2012; Oksanen, 2014; Barret, 2021; Galili, 2021) (and other packages listed in the figure captions and Supplementary Material); SigmaPlot v. 14.0, C2 v.1.7.7 (Juggins, 2007); MATLAB v. R2021a; and ESRI ArcGIS v. 10.4. The final layout of all figures was achieved in Adobe Illustrator CC v. 2021.

4 RESULTS

4.1 Geomorphology and Limnology

The NE shoreline of Lago Pato has a differential GPS (dGPS) ellipsoid corrected elevation of 32.7 ± 1 m a.s.l. (**Table 1**). Former lake shorelines immediately surrounding the lake are visible on satellite images between ~35 and 40 m a.s.l., and there are two further prominent shorelines at ~40–45 m a.s.l. and ~45–50 m a.s.l. that delineate the visible break from grassy wetlands to more densely vegetated bushland around the lake and the transition to more barren grassland cover on the surrounding moraine complexes. The LP08 site is the deepest point of the current lake, with a water level at ~32 m a.s.l. (**Table 1**), while the LP16 core site is located on a slightly elevated (~33–34 m a.s.l.) infilled littoral area of the basin, which is currently a seasonal (ephemeral) wetland, approximately 200 m SW of the LP08 core site (**Figure 2B**). Lago del Toro, immediately north, has a seasonally dependent water level of ~24 ± 5 m a.s.l.

Retaining shoreline ridges separating Lago Pato from Lago del Toro are ~4–10 m above the present water level in Lago Pato, suggesting that moderately higher lake levels in Lago del Toro could plausibly overspill into Lago Pato (**Figure 2B**). Our geomorphological data show that Lago Pato would have become an isolated and closed basin once the water level in Lago del Toro was <32–37 m a.s.l. Water column chemistry measured at the Lago Pato depocentre (LP08 coring site) in February 2007 had a pH of 8.87 ± 0.01 (n = 3; mean ± 1σ), a specific conductance of 331 ± 2 μS cm^{-1}, and a temperature of 11.81 ± 0.04°C and dissolved O_2 of 11.92 ± 0.05 mg L^{-1} (equivalent to 372.5 ± 1.7 μM). Visibility was limited to less than 1 m water depth due to relatively high phytoplankton primary production.

4.2 Sedimentology, Geochemistry, and Chronology

The LP08 and LP16 records were divided into six lithofacies units shown in **Figure 5**. These are summarised and interpreted in **Table 2**, the Supplementary Material, and **Section 5.1**. In summary, the littoral record (LP16) contains all six units, but glaciolacustrine Units 2–4 and the more organic subunit 5A were missing from the depocentre (LP08) record (**Figure 5**; **Supplementary Figure S1**). Units 5B–C and 6 (c. 10–5.8 cal ka BP) were preserved at a much higher resolution in the LP08 record, 0–470 cm (**Figure 5A**) compared to 0–50 cm in LP16 (**Figure 5B**). **Figure 6A** shows the transition from glaciolacustrine to full organic sedimentation at the start of the Holocene between Units 2–4 and 6 in LP16 when Lago Pato was isolated from Lago del Toro and a short-lived return to glaciolacustrine sedimentation between c. 8.9 and 8.6 ka in Units 5B and 6 in LP08 (**Figure 6A**). **Figures 6B–F–F** and **Supplementary Figures S3D, S6** show the decadal-to-centennial-scale variability of erosional inputs into the deep glaciolacustrine basin of Unit 1 in the LP08 and LP16 records between c. 20 and 30 cal ka BP. In LP08, elevated C/N ratios in Units 5 and 6 reflect increased terrestrial organic matter input, with a notable increase in all productivity proxies from c. 5.6 cal ka BP onwards (**Figure 5A**). Principal components analysis (PCA) summarised in **Figure 7** shows that the variance in both LP08 and LP16 XRF-CS datasets is driven by erosional inputs (characterised most strongly by Ti, Rb, and K along the first PC axis in a positive direction) versus negative PC axis 1 values (inc. and coh. scatter, Br, which reflect organic productivity but not Zr as a matrix effect) (**Supplementary Figures S2, S3, S5**).

A complex relationship between Ca, S, Mn, Sr, and, to some degree, Fe exists, driven by a mixture of detrital and/or authigenic processes, but mainly redox changes, represented by the second PC axis. This relationship varies between the two records and between units within each record. For example, in the LP08 record, an inverse correlation between K, Fe, Rb, Zn, and, to some

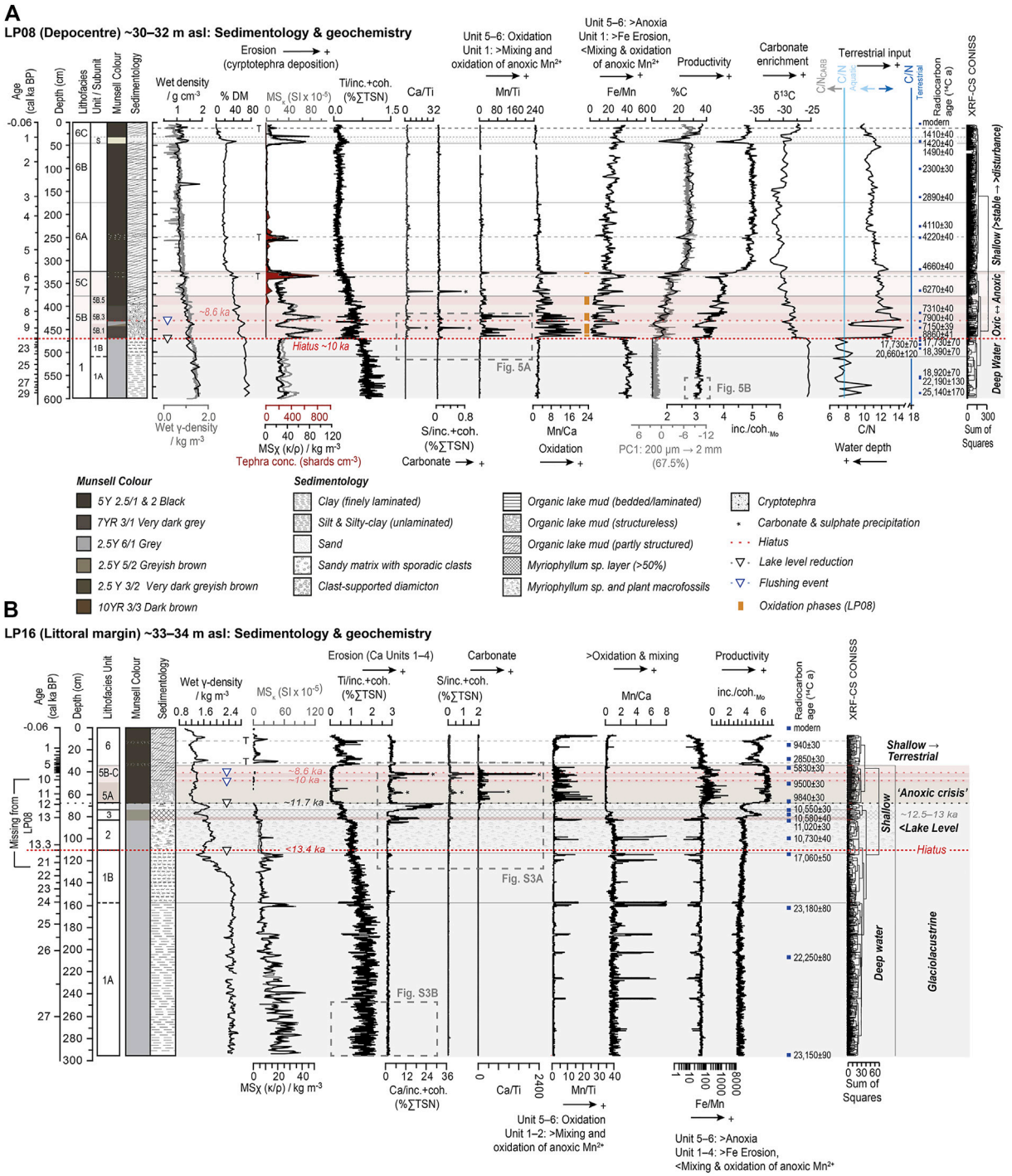

FIGURE 5 | Summary sedimentology and geochemistry data for Lago Pato sediment records. **(A)** LP08 (depocentre site). **(B)** LP16 (littoral-catchment site). This figure integrates sedimentological observations, key core scanning parameters, ratios, and subsample data and shows the main changes in key elements (Ti, Mn, Ca, Fe) and their ratios in both records. Data points between 68 and 62 cm in the LP08 record were not plotted or included in the analysis due to low counts from an extrusion-related surface gap. Data were plotted in C2 (Juggins, 2007) and R, with the final layout achieved in Adobe Illustrator.

degree, Mn versus incoherent and coherent scatter and Br broadly aligns with PC1, while S is strongly correlated with Ca, Mn, and Sr, to a lesser degree, between PC1 and PC2 (**Figures 7A**; **Supplementary Figure S2A**). The PC3 axis reflects an inverse correlation between Mn and Ca, S (**Figure 7B**, **Supplementary Figures S2E–H**). In contrast, the LP16 record has increased variance along the PC2 axis, with Sr and Ca positively correlated with each other yet negatively correlated with all

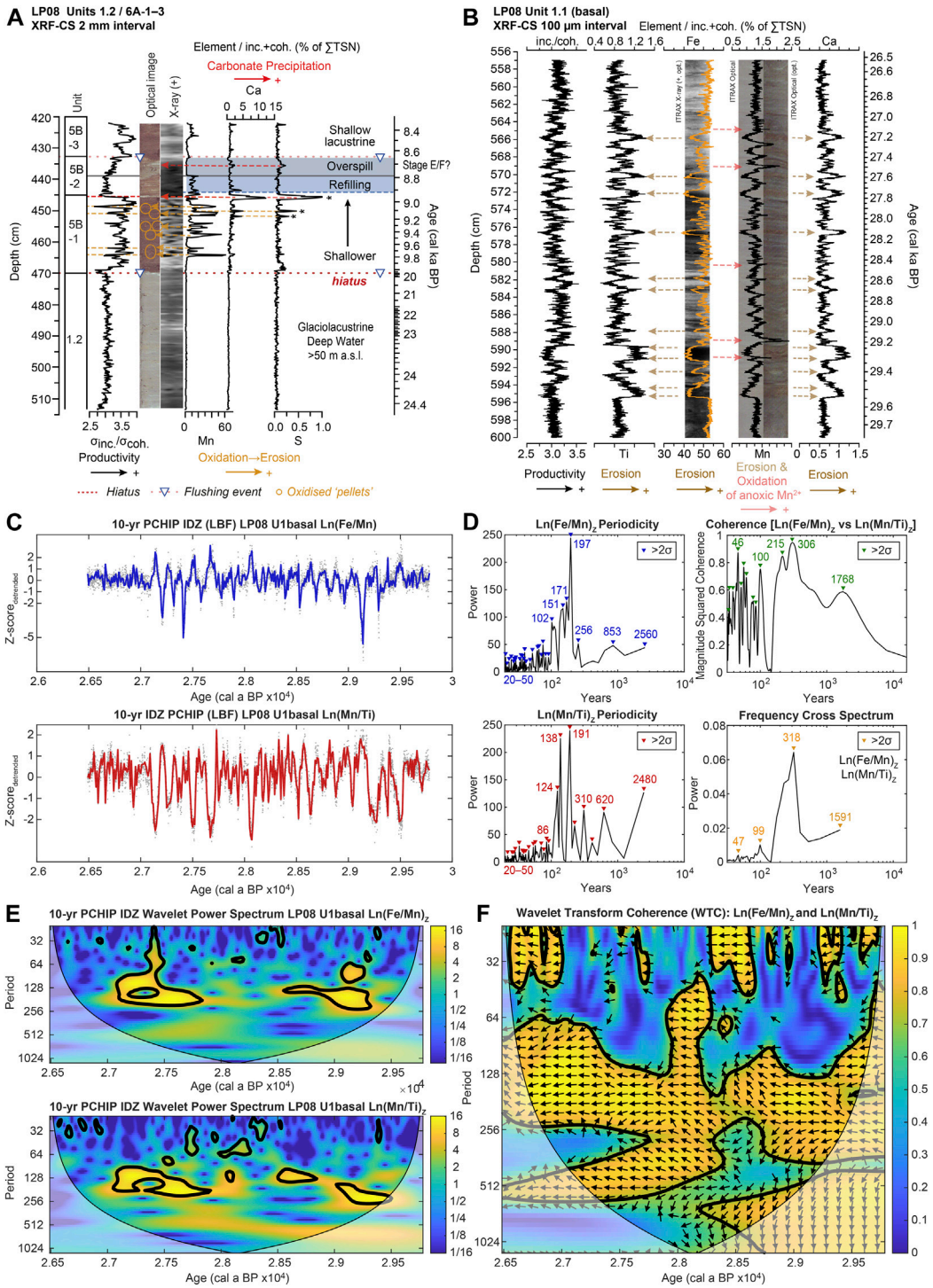

FIGURE 6 | Key geochemical features of the LP08 XRF-CS record. **(A)** Close-up of the Unit 1/Unit 6 boundary showing the sharp boundary (hiatus) at ~470 cm depth (c. 10 cal ka BP) and Mn-rich nodules, and Ca- and S-rich layers associated with carbonate precipitation in a shallow water (arid) sedimentary environment. A short-lived phase of glacier readvance and reformation of palaeo Lago Tehuelche–Puerto Consuelo to >40–<50 m a.s.l. might have occurred between 8.9 and 8.6 ka (Units 5B-2). **(B)** Ultra-high-resolution (100 µm; 44 cm core length) XRF-CS data from the LP08 basal core section plotted against depth and weighted mean modelled age (SH20-M1H model). Variations in organic (inc./coh.), erosional (Ti/inc.+coh. and Ca/inc.+coh. as %TSN), and redox (Mn/inc.+coh. as %TSN) geochemical ratios are shown. **(C)** Time series analysis of the 10-year PCHIP (Piecewise Cubic Hermite Interpolating Polynomial) interpolated $Ln(Fe/Mn)_{Z\text{-scores}}$ (blue line) and $Ln(Mn/Ti)_{Z\text{-scores}}$ (red line) and from the LP08 basal core section (B). The mean sample interval for the dataset (grey dots) is 0.75 ± 0.31 years. **(D)** Power spectrum periodicity, cross-coherence, and cross-spectrum bi-plots for $Ln(Fe/Mn)_{Z\text{-scores}}$ and $Ln(Mn/Ti)_{Z\text{-scores}}$ data from **(C)** with prominent (i.e., >2-sigma) decadal-to-millennial-scale

(*Continued*)

FIGURE 6 | periodicities highlighted. MSC is Magnitude Squared Coherence. **(E)** Wavelet power spectrum and **(F)** wavelet transform coherence (WTC) plots (Grinsted et al., 2004) for $Ln(Fe/Mn)_{Z\text{-scores}}$ $Ln(Mn/Ti)_{Z\text{-scores}}$ from **(C)** showing decadal-to-centennial-scale periodicity [period, in years in **(E,F)**] and time-dependent changes in correlation [0–1 in **(F)**]. WTC uses Monte Carlo methods to assess the statistical significance of cross-coherence against red noise in both time series. Significant (>95% confidence) decadal-to-centennial-scale periodicities and correlations are outlined in black, with a strong and significant correlation for $Ln(Fe/Mn)_{Z\text{-scores}}$ $Ln(Mn/Ti)_{Z\text{-scores}}$. Periodicities of 128–512 years between 30 and 26 ka. Directional arrows in **(F)** show that Ln(Fe/Mn) and Ln(Mn/Ti) are always anti-correlated. Data were plotted and analysed in C2 (Juggins, 2007) and MATLAB, with the final layout achieved in Adobe Illustrator.

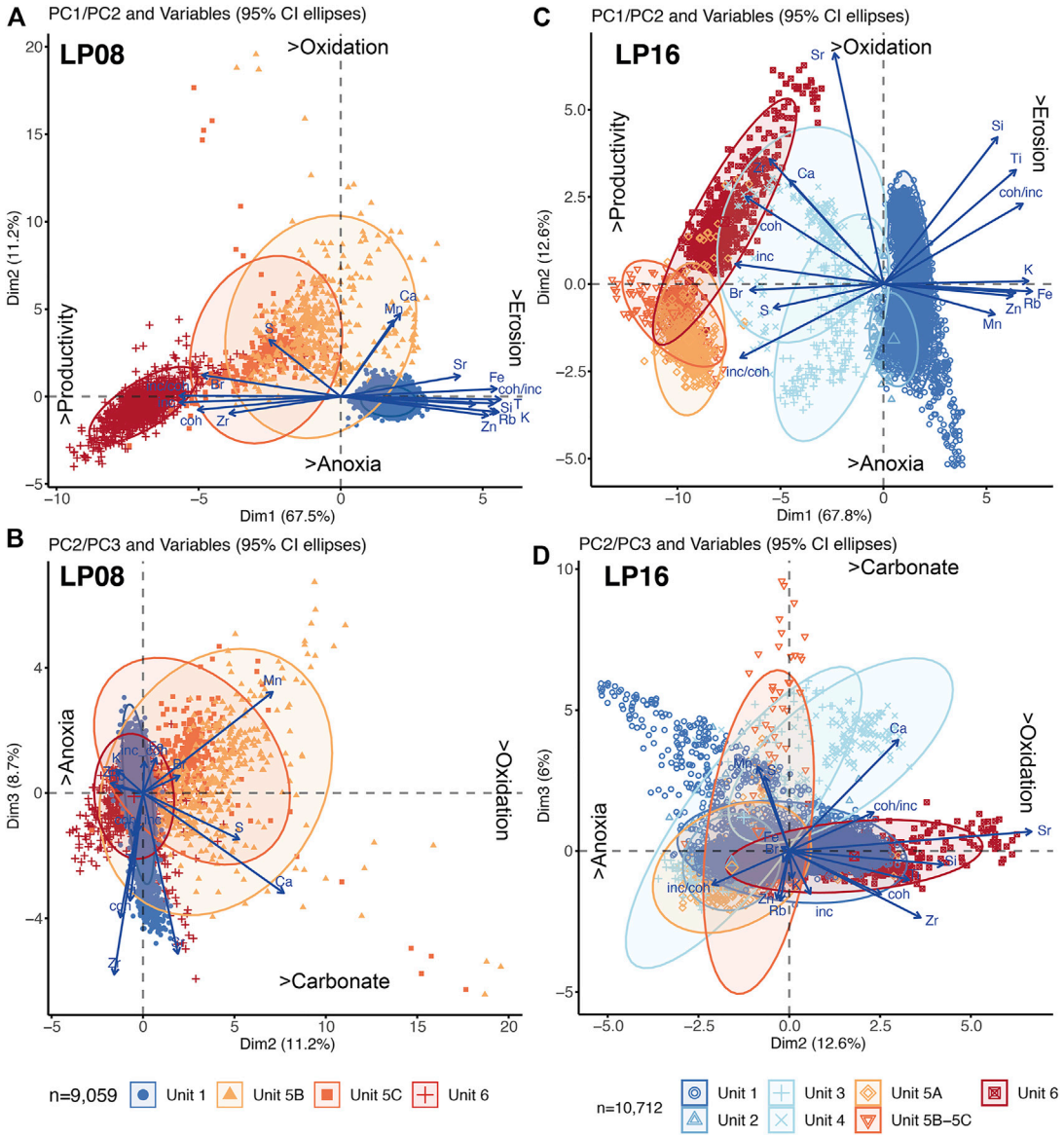

FIGURE 7 | Principal component analysis (PCA) biplots and summary interpretation for **(A)** LP08: PC1/PC2, **(B)** LP08: PC1/PC3, **(C)** LP16: PC1/PC2, and **(D)** LP16: PC1/PC3. Further analysis and PCA biplots are shown in **Supplementary Figures S2, S3**). 'As-measured' 200 μm→2 mm element/total scatter XRF-CS datasets (expressed as a percentage of total scatter normalised sum) were used. Data were $\log_n$ transformed, centred, standardised, and then grouped by lithofacies units as defined by CONISS cluster analysis shown in **Figure 5**. Data were plotted and analysed in R, with the final layout achieved in Adobe Illustrator.

other elements (**Supplementary Figure S3D**). In LP16, S is strongly aligned along PC1, reflecting increased productivity and anoxia within Unit 5A (rather than carbonate), while the PC3 axis describes a positive correlation between Mn and S within Unit 1 (**Supplementary Figure S3**) and is most likely related to deep water anoxia and the Mn and S peaks present in **Figure 5B**.

TABLE 3 | Radiocarbon dating data for the LP08 and LP16 records. Aw, acid wash; a/a/a, acid-alkali-acid pre-treatment; M, macrofossil age; P, paired bulk-macrofossil ages; R, age reversal and length of reversal in years in brackets. Reasons for rejection: X-a, organic sediments emplaced on extraction; X-b, drag down of younger roots during coring.

No.	Lab ID	Core ID and section depth (cm)	Strat. depth (cm)	Carbon source: pre-treatment	$\delta^{13}C_{IRMS}$ (‰)	^{14}C (ab. pMC) (% mod.±1σ)	C-14 age (^{14}C a±1σ)	SH20 calibrated ages (cal a BP) (2σ, 95.4% probability) max.–min.	Mean ± 1σ	Median	Notes
1	SUERC-20903	LP08-SC 1.5–2.0	1.5–2	Macrophytic lake mud: aw	−27.8	104.09 ± 0.45	—	−6 to −70	−15 ± 19	−7	—
2	BETA-281397	LP08-1A: 26.5–27	39.5–40	Macrophytic lake mud: aw	−26.9	83.9 ± 0.42	1,410 ± 40	1,360–1,170	1,270 ± 50	1,280	—
3	BETA-283772	LP08-SC:40 M	40–41	Plant material: a/a/a	−28.5	83.8 ± 0.42	1,420 ± 40	1,360–1,170	1,280 ± 50	1,290	P
4	BETA-281396	LP08-SC:40 B	40–41	Macrophytic lake mud: aw	−29.2	83.07 ± 0.41	1,490 ± 40	1,410–1,280	1,340 ± 30	1,340	P
5	BETA-476098	LP08-1A: 81–82	100.2–101.3	Macrophytic lake mud: aw	−30.0	75.1 ± 0.28	2,300 ± 30	2,350–2,140	2,240 ± 60	2,220	—
6	BETA-281398	LP08-1B: 48–48.5	162–162.5	Macrophytic lake mud: aw	−31.1	69.78 ± 0.35	2,890 ± 40	3,150–2,850	2,980 ± 70	2,970	—
7	BETA-476104	LP08-1C: 53–54	225.2–226.2	Macrophytic lake mud: aw	−31.5	59.95 ± 0.22	4,110 ± 30	4,810–4,420	4,590 ± 100	4,570	—
8	BETA-281399	LP08-1C: 78–78.5	250–250.5	Plant material: a/a/a	−29.5	59.14 ± 0.29	4,220 ± 40	4,850–4,570	4,710 ± 80	4,720	M
9	BETA-281400	LP08-1D: 69–69.5	319.6–320.1	Macrophytic lake mud: aw	−29.2	55.98 ± 0.28	4,660 ± 40	5,480–5,060	5,370 ± 90	5,390	—
10	BETA-281402	LP08-1E: 30–31	365.4–366.4	Plant material: a/a/a	−30.8	45.82 ± 0.23	6,270 ± 40	7,260–6,990	7,130 ± 80	7,120	M
11	BETA-288873	LP08-1E 79–80	414.4–415.4	Organic-rich sediment: aw	−27.8	40.25 ± 0.20	7,310 ± 40	8,180–7,980	8,090 ± 50	8,100	—
12	SUERC-20906	LP08-1F: 10–11	432–433	Organic-rich sediment: aw	−28.3	37.38 ± 0.19	7,900 ± 40	8,980–8,540	8,690 ± 100	8,670	R (-720)
13	SUERC-20907	LP08-1F: 25–26	447–448	Organic-rich sediment: aw	−27.7	41.05 ± 0.20	7,150 ± 39	8,020–7,840	7,930 ± 50	7,940	—
14	SUERC-20909	LP08-1F: 46–47	468–469	Organic-rich sediment: aw	−28.7	33.20 ± 0.17	8,860 ± 41	10,160–9,680	9,900 ± 130	9,880	—
15	BETA-281403	LP08-1F: 52.5–53	474.5–475.5	Glaciogenic clay-rich sediment: aw	−25.2	11.00 ± 0.10	17,730 ± 70	21,790–21,090	21,450 ± 180	21,430	—
16	BETA-281405	LP08-1G: 17.5–18	483.5–484	Glaciogenic clay-rich sediment: aw	−25.2	11.03 ± 0.10	17,710 ± 70	21,760–21,050	21,400 ± 180	21,390	—
17	BETA-281404	LP08-1F: 61.5–62	483.5–484.5	Glaciogenic clay-rich sediment: aw	−24.9	10.13 ± 0.09	18,390 ± 70	22,440–22,130	22,290 ± 70	22,300	—
18	BETA-271299	LP08-1G 26–27	492–493	Glaciogenic clay-rich sediment: aw	−25.6	7.64 ± 0.11	20,660 ± 120	25,200–24,370	24,830 ± 190	24,850	—
19	BETA-281406	LP08-1H: 46–46.5	554.2–554.7	Glaciogenic clay-rich sediment: aw	−24.8	9.49 ± 0.08	18,920 ± 70	22,990–22,550	22,790 ± 120	22,800	R (-3,600)
20	BETA-271298	LP08-1H 48–49	556.2–557.2	Glaciogenic clay-rich sediment: aw	−25.5	6.31 ± 0.10	22,190 ± 130	26,910–25,990	26,420 ± 250	26,380	—
21	BETA-271297	LP08-1I 33–34	589.4–590.4	Glaciogenic clay-rich sediment: aw	−25.3	4.37 ± 0.09	25,140 ± 170	29,910–29,050	29,440 ± 230	29,420	—
22	BETA-480157	LP16-1C(SUR)_0–2	0–2	Plant material: a/a/a	−27.8	103.2 ± 0.40	—	−6 to −7	−6 ± 1	−6	M
23	BETA-480156	LP16-1C(SUR)_15–16	15–16	Organic-rich sediment: aw	−27.8	88.96 ± 0.33	940 ± 30	910–730	820 ± 50	800	—
24	BETA-476093	LP16-1A: 0–1	28–29	Organic-rich sediment: aw	−28.2	70.13 ± 0.26	2,850 ± 30	3,060–2,780	2,920 ± 60	2,920	—
25	BETA-476099	LP16-1A: 8–9	36–37	Organic-rich sediment: aw	−29.7	48.4 ± 0.18	5,830 ± 30	6,730–6,480	6,590 ± 50	6,590	—
26	BETA-476094	LP16-1A: 22–23	50–51	Organic-rich sediment: aw	−28.7	30.65 ± 0.11	9,500 ± 30	11,070–10,570	10,720 ± 110	10,700	—
27	BETA-476095	LP16-1A: 38–39	66–67	Glaciogenic clay-rich sediment: aw	−31.4	29.38 ± 0.11	9,840 ± 30	11,260–11,170	11,220 ± 20	11,220	—
28	BETA-476100	LP16-2A: 20–21 M	74–74.5	*Myriophyllum* sp. aq. moss; a/a/a	−33.0	26.89 ± 0.10	10,550 ± 30	12,620–12,470	12,550 ± 60	12,550	P

(Continued on following page)

TABLE 3 | (*Continued*) Radiocarbon dating data for the LP08 and LP16 records. Aw, acid wash; a/a/a, acid-alkali-acid pre-treatment; M, macrofossil age; P, paired bulk-macrofossil ages; R, age reversal and length of reversal in years in brackets. Reasons for rejection: X-a, organic sediments emplaced on extraction; X-b, drag down of younger roots during coring.

No.	Lab ID	Core ID and section depth (cm)	Strat. depth (cm)	Carbon source: pre-treatment	$\delta^{13}C_{IRMS}$ (‰)	^{14}C (ab. pMC) (% mod.±1σ)	C-14 age (^{14}C a±1σ)	SH20 calibrated ages (cal a BP) (2σ, 95.4% probability) max.–min.	Mean ± 1σ	Median	Notes
29	BETA-476101	LP16-2A: 20–21 B	74–74.5	Glaciogenic grey clay-rich sediment: aw	–27.1	26.79 ± 0.13	10,580 ± 40	12,690–12,470	12,560 ± 70	12,550	P
30	BETA-476096	LP16-2A: 24–24.5_M	78–78.5	*Myriophyllum* sp. aq. moss layer; a/a/a	–36.3	25.36 ± 0.09	11,020 ± 30	13,070–12,780	12,900 ± 60	12,900	M
32	BETA-480158	LP16-2A_46-M	100–100.5	*Myriophyllum* sp. aq. moss; a/a/a	–30.5	26.3 ± 0.13	10,730 ± 40	12,750–12,620	12,700 ± 30	12,710	M
33	BETA-476102	LP16-2B: 22–23	114–115	Glaciogenic clay-rich sediment: aw	–25.0	11.96 ± 0.07	17,060 ± 50	20,780–20,430	20,580 ± 90	20,560	—
34	BETA-480160	LP16-3A_33	162–163	Glaciogenic clay-rich sediment: aw	–25.2	5.58 ± 0.06	23,180 ± 80	27,650–27,250	27,420 ± 110	27,400	—
35	BETA-476103	LP16-3B: 38–39	206.8–207.8	Glaciogenic clay-rich sediment: aw	–25.1	6.27 ± 0.06	22,250 ± 80	26,920–26,120	26,540 ± 200	26,480	—
36	BETA-476097	LP16-4B: 47–48	294.52–295.5	Glaciogenic clay-rich sediment: aw	–25.5	5.6 ± 0.06	23,150 ± 90	27,640–27,230	27,400 ± 110	27,370	—
-	SUERC-20910	LP08-LP08-1I: 51–52	607.4–608.4	Organic sediment: acid washes	–29.3	39.52 ± 0.20	7,460 ± 40	8,370–8,050	8,250 ± 60	8,260	X-a
-	SUERC-20911	LP08-1I: 55–56	611.4–612.4	Organic sediment: acid washes	–29.1	40.34 ± 0.18	7,290 ± 40	8,180–7,970	8,080 ± 60	8,080	X-a
31	BETA-480159	LP16-2A: 30–30.5_M	84–84.5	Plant root material (terrestrial); a/a/a	–27.5	37.68 ± 0.14	7,840 ± 30	8,690–8,450	8,570 ± 50	8,570	X-b

In both records, all calibrated Unit 1 ages from glaciolacustrine sediments were older than 20 cal ka BP, with basal ages of ~30–27 cal ka BP (**Table 3**). In LP08, a significant age gap exists between radiocarbon ages from the top of Unit 1 (471 cm: 21,230 ± 510 cal a BP modelled age ± mean 95% confidence interval) and the base of Unit 6 (470 cm: 10,160 ± 2,120 cal a BP), where a sharp (erosional) boundary exists. Units 2–5 appear to be missing and are present in LP16 only. Units 1 and 2 in the LP16 record are separated by a large age gap, defined by a large downshift in MS values at 110 cm and embedded *Myriophyllum* sp. macrofossils into Unit 2, but without a visually obvious sedimentary discontinuity between 115 and 111 cm (20,660 ± 250–20,440 ± 410 cal a BP) and ~110 cm (13,390 ± 440 cal a BP) (**Table 3**; **Supplementary Figure S1**).

Late Glacial transition ages in LP16 and Holocene ages from both cores (i.e., Units 2–6) were in broadly stratigraphic order, except for a minor age-reversal at 433 cm in LP08 (**Table 2**), where sediment reworking within the shallow basin is evident (**Figures 5A**; **Supplementary Figure S3**; **Table 3**). Ages from Units 2–6 had lower mean ± 2σ 95% confidence ranges (LP08: 300 ± 500 cal years; LP16: 320 ± 280 cal years) than the glaciolacustrine Unit 1 ages (LP08: 890 ± 560 cal years; LP16: 720 ± 440 cal years). Post-bomb calibration ages from an unconsolidated, macrophytic lake mud sample at 1.5–2 cm in the LP08 record, core-top terrestrial vegetation at 0–0.5 cm in the LP16 record, and overlapping ages from paired lake-mud and plant macrofossil remaining at ~40 cm depth imply that exchange between atmospheric and lacustrine carbon reservoirs have been in equilibrium during the late Holocene.

4.3 Diatom and Pollen Analysis

Diatom and pollen were largely absent from Unit 1 of the LP08 record, meaning only samples from 470 cm (10,160 ± 2,120 cal a BP) upwards (Unit 5B) in the LP08 record had sufficient valves and concentrations of palynomorphs for reliable counting statistics. Although single valves of *Staurosirella* aff. *pinnata* (532.7 cm), *Achnanthes* spp. (530.3 cm), and *Fragilaria capucina* s.l., (486.3 cm) diatoms were found, the minerogenic sediments of Unit 1 and Unit 5 sediments up to 454 cm (>9,280 ± 680 cal a BP) were characterised by a near absence of diatoms. Based on cluster analysis, the LP08 core was subdivided into six diatom zones (DZ1–6) between 454 and 0 cm depth (**Figure 8**; **Supplementary Figure S7**). Diatom concentrations remained low (<50 × 10^6 valves g^{-1} dry mass) in DZ1 (454–339 cm; 9,280 ± 680–6,180 ± 560 cal a BP). A diverse benthic diatom community, dominated by *Pseudostaurosira* spp., *Staurosira* aff. *venter*, *Staurosirella* aff. *lapponica*, *Staurosirella* aff. *pinnata*, and *Mastogloia* spp., was already established, supporting geochemical evidence that the first phase of isolation from Lago del Toro (Unit 5A) is missing from the LP08 record. At 416 cm (8,150 ± 160 cal a BP), the initially turbulent, shallow-brackish, and nutrient-enriched lacustrine regime of DZ1a was replaced briefly by more stable and possibly deeper water, indicated by the dominance (~80%) of planktonic species, *Discostella stelligera* species l

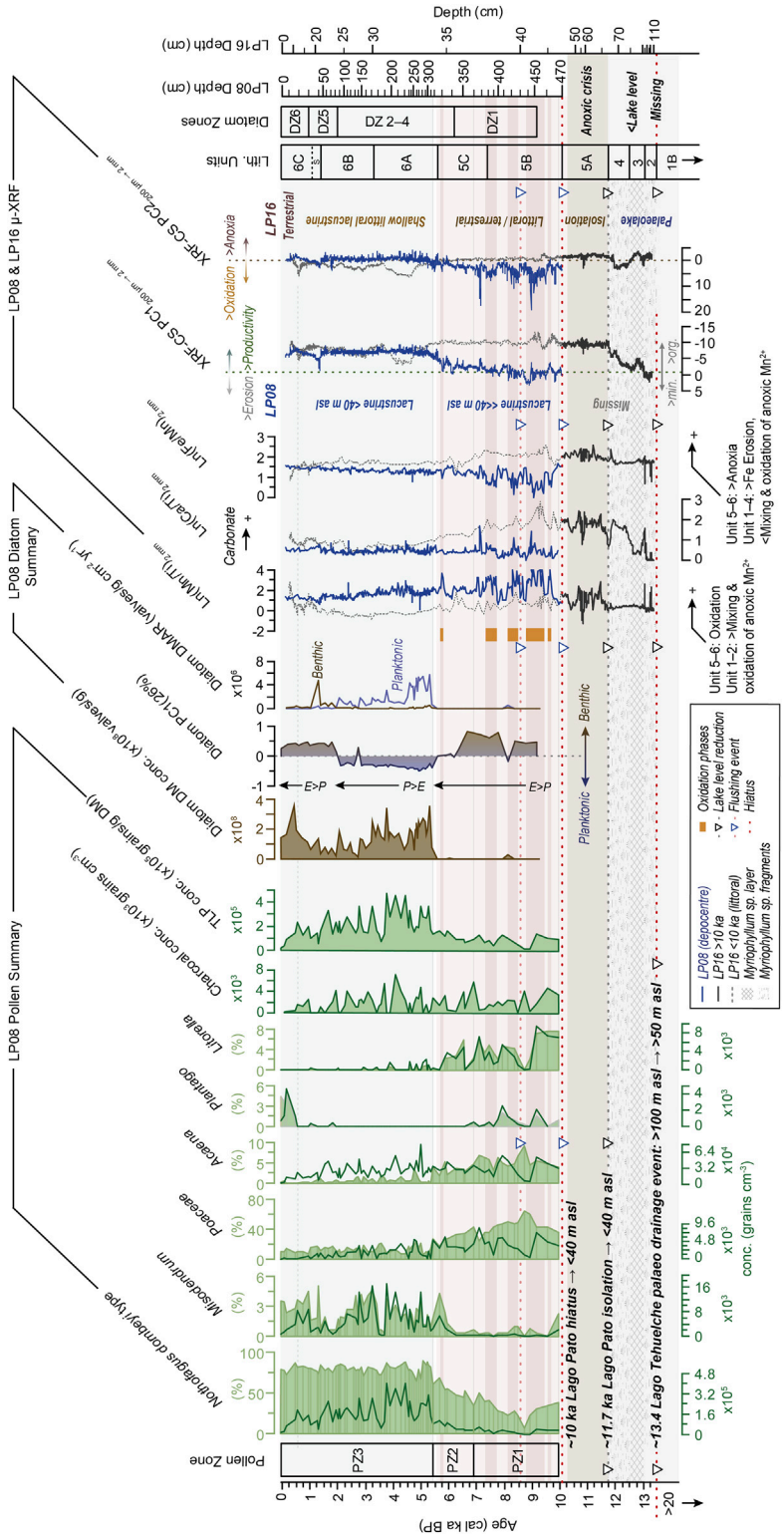

FIGURE 8 | Summary key pollen and diatom compositional diagram for Holocene-age sediments in the LP08 record compared to key geochemical $\log_n$ ratios and principal component (PC1) profiles from the LP08 and LP16 records shown in **Figures 5**–**7**. DM, dry mass concentration, DMAR, dry mass accumulation rate. Data were plotted and analysed in C2 (Juggins, 2007), with the final layout achieved in Adobe Illustrator.

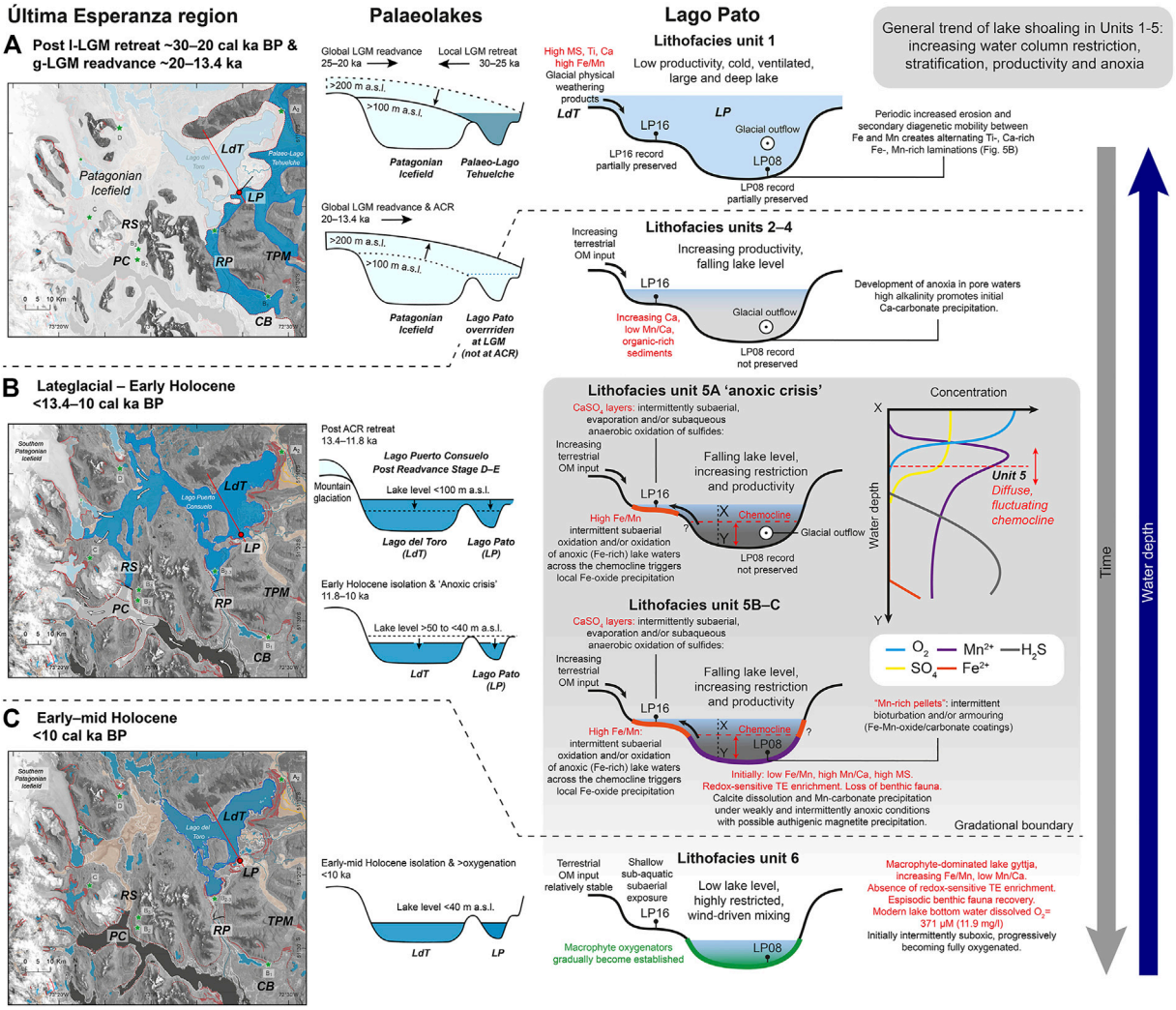

FIGURE 9 | Schematic cartoon and lake ontogeny model illustrating changes in glacial activity and its impact on the Lago del Toro lake level and development of Lago Pato and in the last ~30 ka. **(A)** Cross section across Lago del Toro (LdT) and Lago Pato (LP) during the retreat from local-LGM (l-LGM) glacial limits and during readvance to global-LGM (g-LGM) limit. The outline of Palaeo-Lago Tehuelche (blue) formed after the l-LGM and the extent of the Southern Patagonia Icefield are adapted from Garcia et al. (2014). PC is Puerto Consuelo, TPM is Tres Paso Moraine, CB is Cerro Benetiz, and RS is Rio Serrano. **(B)** Palaeo-Lago Puerto Consuelo at c. 13.4–11.7 ka after the first major lake lowering event and during the early Holocene isolation of Lago del Toro and Lago Pato, between c. 11.7 and 10 ka. Isolation occurred when the palaeolake level fell below ~40 m a.s.l. after glaciers retreated from the Puerto Consuelo area, removing the ice-dam at ~50 m a.s.l. that retained the enlarged palaeolake over Lago del Toro and Lago Pato. Glacier limits shown in **(B)** are minima at c. 11.3 ka following the retreat from advanced ACR positions along the Río Serrano (RS) and from the Cerro Benetiz (CB) area (adapted from García et al. (2014) and the references therein). **(C)** Development of Lago Pato as an isolated basin <10 ka. Chemocline changes in the lithofacies model are based on the Brownie Lake profiles (Wittkop et al., 2020), with observations in black text and interpretations in red text. This figure was made in ARC-GIS and Adobe Illustrator.

(sp.1). More turbulent and shallow-brackish conditions, with benthic *Pseudostaurosira* spp., *Staurosira* aff. *venter*, and *Mastogloia* spp. dominating, returned in DZ1b (**Supplementary Figure S7**).

DZ2 and DZ3 (339–228 cm; 6,180 ± 380–4,520 ± 170 cal a BP) are characterised by the increasing dominance of large and heavily silicified (tycho-) planktonic *Aulacoseira* species and smaller planktonic *Discostella stelligera* s.l., both indicating an increasingly stable, stratified lake with a shallow epilimnion. There is a dramatic increase in diatom concentration at c. 307 cm (*c.* 5,320 ± 210 cal a BP) to >300 × 10^6 valves g^{-1}, followed shortly after by a significant increase in chrysophyte cyst concentration to >250 cysts g^{-1} (**Supplementary Figure S7**). *Aulacoseira ambigua* became increasingly abundant (>~50–60%) at this time, implying that a less well-stratified water column existed.

While *Aulacoseira ambigua* is absent further up-core, the dominance of planktonic species such as *Discostella stelligera* s.l. and *Aulacoseira granulata* s.l. implies more stable conditions (perhaps deeper water) persisted in DZ4 and DZ3 (229–83 cm; 4,530 ± 180–1960 ± 260 cal a BP). Benthic species such as *Staurosirella* aff. *pinnata* briefly became dominant at ~140 cm

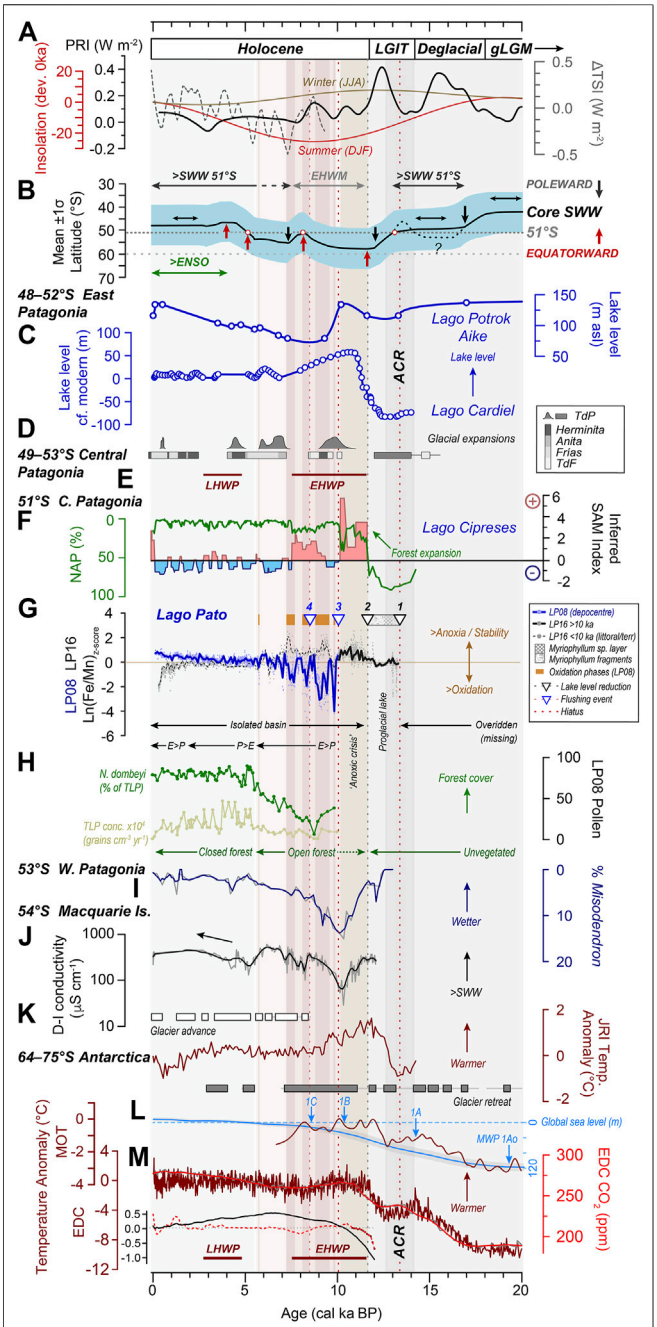

FIGURE 10 | Regional-global driving mechanisms of glacier dynamics and palaeoclimatic change compared with lake-level change in Patagonia and the Fe/Mn (redox) record from Lago Pato over the last 20 cal ka BP. **(A)** Total Solar Irradiance deviation (ΔTSI, dashed grey line) from present-day value (a solar forcing parameter based on variations in ^{10}Be isotope data from ice cores) (Steinhilber et al., 2009), austral winter insolation (June–July–August, JJA; brown line), and summer insolation (December–January–February, DJF; red line) at 51°S (Laskar et al., 2004); the planetary radiative imbalance at the top of the atmosphere (PRI, solid black line). This is the principal driver of global climate change, defined as the difference between the total insolation absorbed at the top of the atmosphere and the amount of energy radiated back into space (Baggenstos et al., 2019). **(B)** Hypothetical representation of the mean annual latitudinal position of the

(*Continued*)

FIGURE 10 | core SWW intensity belt and an approximate 1σ latitudinal range of enhanced precipitation associated with it (Ariztegui et al., 2010; Quade and Kaplan, 2017). Figure adapted from Quade and Kaplan (2017) to include a northward shift in the SWW, driving glacier readvance in the TdP region and between 50 and 55°S during the ACR. The grey dotted line is 51°S; dark grey horizontal arrows represent phases of increased SWW; light grey horizontal arrows represent the Early Holocene Westerlies Minimum (EHWM) ~11.5–7.5 ka (Moreno et al., 2021), which drove the reduction in atmospheric CO_2 between 10 and 8 ka shown in (M). Black arrows represent poleward (or less diffuse) or stable SWW, dark red arrows represent equatorward (or more diffuse) SWW. Selected regional records between ~49 and 53°S that follow are shown in order from east to west across Patagonia and from north to south. **(C)** Lake-level changes at Potrok Aike, a closed basin ~150 km southeast of Lago Pato (Zolitschka et al., 2013), and Lago Cardiel, ~280 km north of Lago Pato in central (Argentinean) Patagonia. Increased lake levels at the latter during the Late Glacial have been linked to stronger SWW and increased precipitation between 48 and 52°S. For Potrok Aike, increased precipitation and higher lake levels during the EHWM were associated with the incursion of the Easterlies (Ariztegui et al., 2010; Zolitschka et al., 2013). **(D)** Compilation of cosmogenic surface exposure dating constraints on glacier expansion for Southern Patagonia and Tierra del Fuego (adapted from Darvill et al. (2015), Kaplan et al. (2020). **(E)** Summary timing of the Early Holocene Warm Period (EHWP) and the Late Holocene Warm Period (LHWP) (Marcott et al., 2013; Kaufman et al., 2020). **(F)** Inferred Holocene SAM-index from positive (red) to negative (blue) SAM-like states overlain by the Northern Arboreal Pollen (NAP) percentage plot from Lago Cipreses, ~11 km WNW of Lago Pato (Moreno et al., 2018; Kaplan et al., 2020). **(G)** LP08 and LP16 Ln(Fe/Mn) ratios as Z-scores representing anoxia/stability ↔ oxidation/instability in Lago Pato. The solid blue (LP08) and solid/dashed black (LP16) lines are a 100-year interval Piecewise Cubic Hermite Interpolating Polynomial (PCHIP) smoothing of measured interval data (light blue, LP08, and grey, LP16, circles). Downward black triangles denote lake level reductions at 1) c. 13.4, 2) 11.7 ka in LP16. Downward blue triangles represent flushing events at c. 10 ka (3, erosional hiatus) and c. 8.6 ka (4, refilling/emptying event) in the LP08 depocentre record. **(H)** Percentage count data for *Nothofagus dombeyi type* and total land pollen (TLP) concentrations as proxies for changes in vegetational cover in the Lago Pato catchment over the last c. 10 cal ka BP and a summary of the inferred precipitation: evaporation (P:E) balance, based on the LP08 PC1 axis diatom data (**Figure 8**). **(I)** Relative percentage changes in *Misodendrum* (mistletoes commonly found on deciduous *Nothofagus* species) in sediment records from the western Andes (Lamy et al., 2010; Fletcher and Moreno (2012) interpretation). **(J)** Changes in diatom-inferred **(D–I)** conductivity from Macquarie Island (Saunders et al., 2018) as an indicator of increasing SWW at ~54°S. The black line is a 100-year LOESS smoothing of as-measured D-I data (grey line). **(K)** A compilation of the timing of glacier advance and retreat on the northern Antarctic Peninsula (Kaplan et al., 2020) and temperature anomaly data from the James Ross Island ice core record (Mulvaney et al., 2012). **(L)** Global Mean Ocean Temperature (MOT) 20–6.5 cal ka BP (Bereiter et al., 2018) and a stacked global mean sea level curve 20–0 ka (Spratt and Lisiecki, 2016). **(M)** Atmospheric CO_2 concentrations (100-year LOESS smoothing (red line) of raw data (grey line) and temperature anomaly data from the EPICA Dome C ice core record in Antarctica (dark red line) (Monnin et al., 2001; Jouzel et al., 2007), Holocene palaeotemperature compilation of median temperature anomalies (relative to 1800–1900 CE) for 60–90°S (dashed red line), and globally (black line) (Kaufman et al., 2020) and a summary of the main Holocene warm periods at 30–90°S (Marcott et al., 2013) (dark red bars). The grey dotted line is the median 12 kyr temperature value for 60–90°S (0.02); fifth (–2.21) and 95th (1.51) error percentiles are out of the plotting range. The background shading in this figure summarises the timing of the key features in the Lago Pato record as follows: green shading represents a late Holocene phase of enhanced ENSO (El Niño Southern Oscillation); light red shading represents more arid conditions; dark red shading with orange bars represents enhanced oxidation phases; light brown shading represents the "Anoxic Crisis"; light grey shading represents glaciogenic deposits; dark grey shading indicating the time period covered by the Antarctic Cold Reversal (ACR: 14.6–12.8 ka). Data in this figure were analysed and plotted in SigmaPlot and R, with the final layout achieved in Adobe Illustrator.

(2,740 ± 260 cal a BP) within DZ4 when a dramatic reduction in the planktonic *Discostella stelligera* species to <20% abundance occurred. This brief excursion to more unstable conditions coincided with a shift to lower S/Ti ratios, indicative of slightly shallower, less anoxic conditions, a shift to less depleted $\delta^{13}C$ values (~ −30%), and a short-lived erosional phase in the LP16 record at c. 2,700 cal a BP. The return of *Discostella stelligera* s.l. to 60%–80% abundance suggests that a more stable deeper lake persisted until c. 2000 cal a BP when an abrupt increase in benthic species (e.g., *Staurosirella* aff. *pinnata*) reoccurred. Low chrysophyte cyst concentrations between 78 and 30 cm within DZ5 (DZ5: 83–30 cm; 1,960 ± 260–1,020 ± 310 cal a BP) also indicate more turbulent conditions. These conditions persisted during the last c. 1,000 cal a BP (DZ6: 0–30 cm; 1,020 ± 310 to −60 ± 10), but with *Staurosira* aff. *venter* (>75%) dominating. In contrast, the most recent surface sample (0.25 cm) is dominated by planktonic *Cyclotella meneghiniana* (75%) species.

Above 470 cm (10,160 ± 2,120 cal a BP), we identified 13 pollen taxa with a relative abundance of more than 2% and three significant local pollen assemblage zones (PZ 1–3 in **Figure 8**, **Supplementary Figure S8**). Pollen zones 1 and 2 (470–359 and 359–315 cm; 10,160 ± 2,120–6,890 ± 300 and 6,890 ± 300–5,400 ± 180 cal a BP), which map broadly onto Units 5B and 5C, are characterised by low total pollen (and diatom) concentrations and relatively high values of Poaceae that reach a maximum (>60%) at 436 cm depth (8,730 ± 270 cal a BP) and decline towards the top of the zone. Poaceae are commonly used as an aridity indicator species in Patagonia (Moreno et al., 2018; Moreno et al., 2021) and are more elevated in Unit 5B of LP08 where Fe/Mn and Mn/Ti are more variable, and elevated Ca/Ti and Sr/Ti (carbonate) ratios and S peaks exist. Together, these proxies indicate that a very restricted lake system existed in the early Holocene between c. 10,000 and 7,500 cal a BP (**Figures 5A**, **8**). Most notably, *Nothofagus dombeyi* type pollen starts to increase from ~420 cm (c. 8,270 ± 240 cal a BP) onwards, and there are low percentages of dwarf shrubs and herbs such as *Empetrum rubrum*, Asteraceae, *Acaena,* and *Litorella* (**Figure 8**, **Supplementary Figure S8**). *Nothofagus dombeyi* type, inversely related to Poaceae, increases towards the top of this zone, while the abundance of Cyperaceae (as well as Polypodiaceae and *Pediastrum*, not shown in the summary of **Figure 8**, **Supplementary Figure S8**) remains high throughout.

In local pollen assemblage zone 3 (PZ 3 in **Figure 8**, **Supplementary Figure S8**; 315–0 cm; 5,400 ± 180 to −60 ± 10 cal a BP), *Nothofagus dombeyi* type continues to dominate (60%–80%), with the total pollen concentration higher than in PZ 1 and 2, indicating a generally more productive (wetter) environment. The hemiparasite *Misodendrum* requires *Nothofagus* as a host for germination and establishment; hence, *Misodendrum* and *Nothofagus dombeyi* are well-correlated (**Figure 8**). Poaceae abundances were lower (<30%) and oscillated at (sub)millennial timescales, while other dwarf shrubs and herbs almost disappeared from the record until the last 500 years. The decline in Cyperaceae at the start of pollen zone 1 continued until the present. The relative abundance of *Pediastrum* is lower than PZ 1 but oscillates, reaching peak values between ~200 and 100 cm (3,920–2,220 cal a BP). Small amounts of introduced European taxa (e.g., *Plantago* and *Rumex acetosella*, not shown in **Figure 8**) were present near the top of the core.

5 DISCUSSION

5.1 Lake Geochemistry and Ontogeny

In the following section, we interpret the main geochemical changes in the LP08 and LP16 records (**Table 2** for a summary).

Unit 1 (30–20 ka): the elevated sediment density, magnetic susceptibility, and minerogenic input (e.g., K, Ti, Fe, Rb, and Sr) and the near-complete absence of pollen in Unit 1 are consistent with a high input of fine glacial clay eroded from an enlarged, glaciated, and sparsely vegetated catchment (**Figure 9**). Fine glacial sediment in suspension would have created 'turbid' conditions even within a relatively deep lake, preventing the establishment of photoautotrophic diatom communities (Karst-Riddoch et al., 2009). Prolonged phases of perennial lake-ice cover and increased turbidity are consistent with the low primary production and production proxy values (e.g., $\%C_{org}$, C/N, inc./coh.), the absence of diatoms (Hodgson et al., 2009), and stratification within perennially ice-covered and deep glaciolacustrine lakes (Wennrich et al., 2014).

Fine grey glaciolacustrine sediments are enriched in Fe and Mn but have broadly stable Fe/Mn ratios throughout Unit 1, suggesting an erosional source of glaciogenic sediment into Lago del Toro that did not change substantially until the start of the Holocene. As Fe^{2+} is less stable in anoxic lake sediments and precipitates before Mn^{2+}, elevated Fe/Mn ratios have been used as a proxy for increased stability (and anoxia) in deep, well-ventilated lakes (Kylander et al., 2011). Decadal-scale elevation of Mn and Fe coincides with phases of reduced erosional input (shown by <Ti in **Figure 6B**) and is associated with manganese carbonate formation, rhodochrosite ($MnCO_3$), commonly found in areas of shale bedrock and anoxic conditions (Melles et al., 2012), but has also been used as an indicator of increased oxidation where wind-driven mixing of the water column exists in deep lakes (Moreno et al., 2007; Kylander et al., 2011). In shallow(er) lakes, >Mn can reflect complete overturning (as well as oxygenation) of stratification, reducing Mn solubility and causing manganese oxides and hydroxides to co-precipitate with iron oxy-hydroxides (Wennrich et al., 2014; Davies et al., 2015).

Comparatively minor increases in Fe/Mn and decreased Mn/Ti in Unit 1 (relative to Unit 5) most likely reflect short-lived bottom water anoxia interspersed with oxidation events linked to minor increases in Mn^{2+} precipitation and/or secondary mobility between Fe and Mn phases within laminations (**Figures 5**, **6**, **8A**). High MS and exceptionally elevated Mn/Ti peaks in LP16 Unit 1 (as well as 2) reflect increased mixing and oxidation of anoxic Mn^{2+} during lake overturning (**Figures 6B–D–D**, **8**). A minor component of biogenic magnetite formed under anoxic conditions (Kirschvink and Chang, 1984) could exist, but this is more likely in Unit 5, where strong anti-correlation between

these ratios also exists during an early to mid Holocene arid phase c. 11.8–7.5 ka, extending until c. 5.6 ka (**Figures 6A**, **8B**).

Periodic orangey-brown Ti- and Ca-rich bands within Unit 1 imply decadal-centennial-scale phases of increased erosion or erosion from a different local source, perhaps with a degree of secondary diagenetic mobility between Fe and Mn, between 29.8 and 20.5 ka (i.e., the period covered by Unit 1 in Lago Pato) (**Figures 6B–F–F**, **9A**, **Supplementary Figures S3B, S6**). Fe/Mn and Mn/Ti profiles within the basal deposits of Unit 1 and across the whole of Unit in LP08 have several significant (>two-sigma) periodicities (**Figure 6D**, **Supplementary Figures S6E,F**). Decadal-scale variability is apparent within Unit 1 of both records, notwithstanding its average age model 95% CI of >700 years. The mean prominent peak-peak interval for Ln(Fe/Mn) and Ln(Mn/Ti) in LP08 Unit 1 is 35 ± 19 and 37 ± 22 years (**Supplementary Figures S6C,D**) and 34 ± 16 and 37 ± 16 years for LP16 Unit 1 (**Supplementary Figures S6N,O**). Decadal-scale variations are also apparent in the wavelet analysis shown in **Figures 6D–F**. Because the data shown have been interpolated to evenly spaced 10-year intervals, a combination of multiple 8–16-year SAM cycles (Yuan and Yonekura, 2011) could plausibly be responsible for the low frequency 20–40-year periodicities observed in Unit 1 (**Figures 6D–F**, **Supplementary Figures S6E–K**). At the centennial scale, the 197-year periodicity in Fe/Mn and the 191-year periodicity in Mn/Ti for the LP08 Unit 1 basal deposits (**Figure 6D**) and the 197/233-year periodicity in Fe/Mn and the 248-year periodicity in Mn/Ti for the whole of LP08 Unit 1 (**Supplementary Figure S6E,F**) are broadly similar to the ~200–250-year solar cycle that is thought to modulate SWW airflow detected in high-resolution pollen records from Patagonia and the Falkland Islands (Turney et al., 2016; Moreno et al., 2018). Longer (centennial–millennial) periodicities in Unit 1 deposits of both LP08 and LP16 might reflect 'grand solar cycles' driven by changes in the Sun's magnetic field (Ineson et al., 2015). Although we failed to find convincing evidence for the ~2.4–2.5 kyr Hallstatt solar activity cycle (Viaggi, 2021), it seems likely that millennial-to-centennial-scale variations in solar activity (shown in **Figure 10A**), SWW, and SAM (**Figures 10B,F**), coupled with changes in internal glacier dynamics, drove fluctuations in glacier accumulation, meltwater input, and seasonal lake-ice cover between the l-LGM and g-LGM, which account for variations in deep water (in)stability, redox conditions, and lake stratification processes between 29.8 and 20.5 ka.

Several lines of evidence support Units 2–5A being missing from the LP08 record: 1) the lack of pollen from a cold-steppe scrubland environment and the existence of an already established open landscape with a *Nothofagus* forest (comprising ~30% of TLP) around Lago Pato; 2) the existence of a benthic diatom community in organic sediments of Unit 5B that were deposited unconformably on top of Unit 1 glacial sediments; 3) the presence of shallow-water sub-aquatic angiosperm *Myriophyllum* sp., an early coloniser in organic deposits <10 ka (Unit 5 in LP08); and 4) the absence of two substantial Volcan Reclus tephras dated to 9,320 ± 15 ^{14}C yr BP (10,570–10,300 cal a BP) in the basal glaciolacustrine unit in a record from nearby Lago Eberhard (Moreno et al., 2012) and other lake records in the Última Esperanza region (Sagredo et al., 2011) and the R1 tephra dated to 12,627 ± 48 ^{14}C a BP (15,190–14,610 cal a BP) (Sagredo et al., 2011). The latter is >20 cm thick in the Cerro Benitez area ~31 km S of Lago Pato (McCulloch et al., 2021), and the presence in lacustrine deposits indicates that ice had thinned to at least ~215 m a.s.l. by 17.5 ka (Sagredo et al., 2011).

Units 2–4 (13.4–11.8 ka): the presence of *Myriophyllum* sp. fragments embedded in the glaciogenic deposits of Unit 2, and a ~10 cm thick *Myriophyllum* sp. layer is evidence of a substantial increase in lake productivity following a dramatic drop in lake level c. 13.4–13.0 ka. Increasing Ca and Sr (but not S) towards the top of Unit 3 and into Unit 4 relates to precipitation of authigenic calcite, likely triggered by increased alkalinity linked to anaerobic degradation of organic matter (Torres et al., 2020) (**Supplementary Figure S3A**). The lack of Mn enrichment in Units 3 and 4 (characterised by low Mn/Ca, **Figure 5B**, **Supplementary Figure S3**) suggests Mn was not available for fixation during authigenic (early diagenetic) carbonate precipitation (**Figure 9B**).

Unit 5 (11.6–5.6 ka): exceptionally elevated and concomitant Ca/Ti and S/Ti and low Mn/Ca in Unit 5 represent localised authigenic carbonate and/or sulphate precipitation, possibly gypsum ($CaSO_4{\cdot}2H_2O$; asterisks in **Figure 5**) or anhydrite. The presence of large S peaks indicates relatively S-rich lake bottom waters (SO_4 or H_2S, depending on local redox conditions) despite freshwater conditions. Gypsum precipitation implies subaerial exposure (drying) or potentially subaqueous anaerobic oxidation of solid sulphides by Fe^{3+} or Mn^{4+} (Aller and Rude, 1988; Pirlet et al., 2010). This seems plausible because Unit 5 exhibits phases of authigenic enrichment in Mn (exceptionally high Mn/Ti; **Figures 5**, **8**).

Unit 5 of LP16 has two phases of exceptionally elevated Fe/Mn ratios: an initial 'Anoxic Crisis' following isolation from Lago del Toro at the start of the Holocene and a secondary phase between c. 9 and 7.5 ka. High Fe/Mn and high Fe/Ti in Unit 5 (**Figures 5**, **8**, **Supplementary Figure S6**), above the 'background' glaciogenic detrital signal, implies a preference for authigenic enrichment of Fe compared to Mn. Assuming redox conditions analogous to Brownie Lake (Wittkop et al., 2020), fixation of Fe^{2+} was most likely triggered by oxidation of anoxic (Fe-rich) lake waters across the chemocline (**Figure 9C**). Alternatively, the very high Fe content of Unit 5A might be attributed to a very shallow, possibly even terrestrial, environment at the littoral LP16 site as peat can become highly enriched in Fe^{3+} during more oxic (drier) conditions (Schittek et al., 2015). Fe enrichment also occurs in anaerobic (very shallow) organic lake and peat deposits when organic material breaks down under stable conditions (Damman, 1978). Mn is then reduced from tetravalent MnO_2 to its divalent Mn^{2+} state and removed from organic matter, elevating Mn values and ratios. The near absence of Mn and low Mn/Ti when Fe/Mn is elevated in Units 5B/C implies that the LP08 depocentre remained submerged throughout the Holocene.

More stable conditions associated with reduced SWW between c. 11.6 and 5.5 ka were interrupted by short-lived

phases of instability, most notably at c. 10.5–10.0 ka in LP16, which coincides with the timing of the erosional hiatus in the LP08 record at c. 10.1–10.0 ka. The concomitant reversal in the Fe/Mn profiles of LP08 and LP16 following the 'Early Holocene Anoxic Crisis' (c. 11.7–10.1 ka) in Unit 5A of LP16 (**Figures 7**, **10G**) suggests local redox processes and water depth, rather than regional (climatic) processes, were the main control on the distribution of these metals during the Holocene.

A simple 'oxide model' attributing Mn enrichment to the onset of more oxygenated bottom water conditions (Force and Cannon, 1988; Calvert and Pedersen, 1996) is not considered plausible because bottom waters were least ventilated at LP08, the lake depocentre, compared to LP16. A more credible explanation invokes Mn-carbonate (most likely rhodochrosite, $MnCO_3$) precipitation immediately beneath the chemocline at LP08, with trapping of Fe-oxides above the chemocline at LP16 (**Figure 9B**), consistent with redox systematics in analogous lakes (e.g., Brownie Lake; Wittkop et al., 2020). Fixation of Mn in carbonate is supported by increased Mn/Ca in Units 5B-C at LP08. A fluctuating and complex redox relationship between Fe and Mn in LP08 is evident in orange 'pelletised' deposits with exceptionally elevated MS, Mn, and Mn/Ti ratios in Unit 5B (**Figure 6A**). These are most likely due to co-precipitation of Mn under anoxic conditions (or possibly the formation of rhodochrosite or kutnahorite minerals, particularly where Fe enrichment occurs). The presence of benthic diatoms in Unit 5B implies bottom water conditions at LP08 during the early to mid Holocene were only intermittently (rather than persistently) anoxic (**Figures 7**–**9**), while the disappearance of benthic diatoms at the base of Unit 5C and through most of Unit 6, until c. 1.5 ka, suggests the development of more permanent anoxia in a deeper and more stable lake between c. 7.3 and 5.6 ka onwards.

Unit 6 (5.6 to–0.06 ka): increasing Ti content and Mn/Ca implies Unit 6 at LP16 was deposited under progressively shallow water (above the chemocline), culminating in a sharp decline in the Fe/Mn profile at LP16 profile c. 500–200 years ago, which mirrors the increasingly anoxic >Fe/Mn trend in the submerged LP08 site (**Figure 10G**) and implies a shift to terrestrial subaerial conditions at the littoral margins of Lago Pato. At LP08, the continued accumulation of macrophytic organic matter suggests lacustrine conditions were more favourable for colonisation. Progressively increasing Fe/Mn, a sharp decrease in Mn/Ca and Mn/Ti (**Figures 5A**, **8**), a lack of authigenic enrichment in redox-sensitive metals (e.g., V), and a return of benthic diatoms (**Figure 8**, **Supplementary Figure S7**) all suggest bottom waters became progressively more ventilated at the depocentre in the late Holocene, consistent with the well-oxygenated modern lake conditions (371 μM O_2 (11.9 mg/L)).

To summarise, we have identified five key phases in the history of Lago Pato. In the following sections, we relate these five phases to glacier retreat and readvance and lake-level change in the Torres del Paine and Última Esperanza region since ~39 ka and, more widely, to hemispheric-global driving mechanisms of paleoclimatic change, in particular, the changing strength and position of the SWW relative to 51°S.

5.2 Local to Regional Implications

5.2.1 Local-LGM—Global-LGM and Deglaciation (<39–>14 ka)

The LP08 and LP16 records provide evidence of glaciolacustrine deposition into Lago Pato until c. 11.7 ka (**Figure 10G**; **Table 2** for a summary). High volumes of minerogenic erosional inputs and low productivity fluxes throughout lithofacies Unit 1 and in Units 2–4 reflect the proximity of an ice tongue from an expanded Southern Patagonian Ice Field following the retreat from the l-LGM (c. 37–30 ka) and after the g-LGM (c. 26–19 ka) (Hughes and Gibbard, 2015). The large ice-dammed proglacial lake, palaeo-Lago Tehuelche, covered Lago del Toro and Lago Sarmiento <c. 38 ka and >c. 17.6–16.8 ka, between local- and global-LGM advances (c. 32–27 ka) and as glaciers withdrew after the g-LGM (García et al., 2012; García et al., 2014; Davies et al., 2020) (locations B_1, B_2 in **Figures 2A**, **9**). Unit 1 in LP08 and LP16 is a preserved fragment of this former palaeolake sedimentary record, with a 'floating chronology' reflecting deposition in a deep palaeo-proglacial lake that existed at Lago Pato between 30 and 20 ka, prior to g-LGM, and ACR readvances over Lago del Toro and Lago Pato between 14.6 and 12.9 ka. (**Figures 8**–**10**).

A glaciolacustrine environment existed at Lago Pato between c. 28 and 20 ka after glaciers had receded from their most advanced (MIS 3) positions along the Río Tres Pasos valley to the south-east, where a terminal moraine has been dated to c. 39–37 ka (location A_2 in **Figure 2A**). From c. 30 ka onwards, as the Antarctic Ice Sheet and sea-ice grew during the g-LGM, the core belt of SWW became weaker at 51°S as it shifted equatorward to ~40–45°S, north of Lago Pato and its current alignment with the Antarctic Circumpolar Current off the coast of Chile at ~50–52°S (Toggweiler and Russell, 2008; Van Daele et al., 2016; Quade and Kaplan, 2017) (**Figure 10B**). Reduced precipitation supply in the Última Esperanza region led to glacier retreat and large palaeolakes formed as the main SPI outlet glacier covering Lago del Toro thinned and withdrew eastwards and from its maximum extent along the Río Prat and Río Tres Paso valleys to the south and south-east (**Figure 9A**) (Sagredo et al., 2011; Solari et al., 2012; García et al., 2014). Palaeolakes in the Puerto Consuelo and Última Esperanza fjords merged, forming a much larger palaeo-Lago Tehuelche–Puerto Consuelo up to 280 m a.s.l. deep along the Río Prat valley (García et al., 2014; Davies et al., 2020) (location B_1, **Figures 2A**, **9A**). Ice-dammed deposits and terraces in the Río Prat, Río Tres Paso, and Puerto Consuelo valleys between 125 and 155 m a.s.l. have been dated to c. 18–17 ka (García et al., 2014), suggesting that an ice dam up to 150–200 m a.s.l. existed along the Puerto Consuelo-Última Esperanza fjord at the gLGM.

The absence of deglacial age sediments <20 ka, at both coring sites in Lago Pato, implies that it was overridden by readvancing LGM and ACR glaciers or sediments were removed when palaeo-Lago Tehuelche emptied across the Lago Pato spillway sometime between c. 20 and 13.4 ka, in line with García et al. (2014) (**Figures 2B**, **9B**,C). The latter interpretation is more probable as geomorphological evidence and glacial debris associated with

glacier advances over Lago Pato are absent. After glaciers had retreated in the early Holocene, the removal of Units 2–4 from LP08 and the exceptionally sharp erosional boundary between the glaciogenic sediments of Unit 1 and organic deposits of Unit 6 were created by meltwater emptying across the Lago Pato depocentre at c. 10 ka (**Figures 8**, **9**).

Successive palaeolake lowering after the g-LGM occurred sometime before c. 17 ka during Stage I of the Cordillera Paine glaciation scheme (García et al., 2014; García et al., 2018) and after glacial advance stages C and D in the Strait of Magellan that ended between c. 21.7–20.4 ka and c. 17 ka (McCulloch et al., 2005). The oldest minimum radiocarbon ages for ice retreat and the formation of ice-dammed lake deposits in the Lago Sofia-Puerto Consuelo valley area are c. 18–17 cal ka BP (Sagredo et al., 2011; McCulloch et al., 2021) (**Figure 2**).

Garcia et al. (2014) associated a small moraine-arc to a former ice-lobe that extended east and southwards into the Río Prat Valley (B_1 in **Figure 2A**) and the now-abandoned outwash sandur plains formed along to the south and east of Lago del Toro with ice-dammed palaeo-Lago Tehuelche. This finally emptied, sometime after c. 16.8 ka but before the start of the ACR at c. 14.6 ka when a northward latitudinal shift in the SWW drove glacier readvance across this part of Patagonia (**Figure 2A**) (Pesce and Moreno, 2014; Moreno et al., 2018; Moreno, 2020; Fletcher et al., 2021). The absence of sediments dated between c. 20 and 13.5 ka from both Lago Pato records is consistent with basal ages of c. 14.6 ka from the Lago Cipreses record (~11 km west WNW of Lago Pato at 51°17′16.43″S, 72°50′12.18″W; **Figure 10F**) that constrain the initiation of local ice-free and the end ice-marginal glaciolacustrine conditions at ~110 m a.s.l. along the southern shore of Lago del Toro (i.e., ~85 m above Lago del Toro at 25 m a.s.l.) (Moreno et al., 2018).

Organic sedimentation in the higher altitude closed basin Lago Cipreses record at 110 m a.s.l. suggests that ice covering Lago del Toro had receded by, more than 12 km, from the end of the lake (and, inward by more than 50%), by 14.6 ka (Moreno et al., 2018). A similar transition is recorded in lake records from the Puerto Consuelo area at ~15.4 ka (80 m a.s.l.) (Pantano Dumestre), implying that a stepwise regression of Lago Puerto Consuelo began before the start of the ACR at c. 14.6 ka (Moreno et al., 2012).

5.2.2 Late Glacial–Holocene (13.4–11.7 ka)

The lower-altitude Lago Pato records provide evidence of two further stepwise lowering events during the Late Glacial: 1) at c. 13.4–13.0 ka, towards the end of the ACR, when lake levels dropped from >100 m a.s.l. to between 40 and 50 m a.s.l. (**Figures 5B**, **8**, **9B**), which is consistent with the c. 12.8 ka cessation of glaciolacustrine deposition at Lago Eberhard ~70 m a.sl. (cf. Moreno et al., 2012); 2) at c. 11.7 ka, when water levels dropped below 40 m a.s.l., Lago Pato became isolated from Lago del Toro (**Figure 9C**).

The most dramatic reduction in lake level at c. 13.4–13.0 ka is represented in LP16 by the presence of the shallow-water *Myriophyllum* sp. layer Unit 3 within glaciogenic sediments and exceptionally elevated Ca (as well as S and Sr) due to increased deposition of shallow-water carbonates (Units 3 and 4) (**Figure 8**). This post ACR drainage event occurred after Meltwater Pulse 1A at c.14 ka during a phase of rapidly rising global sea level and oceanic warming (**Figure 10L**) and before unprecedented 700-year warming of the Southern Ocean at c. 12 ka (Bereiter et al., 2018). During the Late Glacial, an enlarged proglacial lake encompassed Lago Pato, Lago del Toro, Lago Porteño, and all the smaller basins and sandur along the Río Serrano (Garcia et al., 2014). This palaeolake was topographically dammed at ~50 m a.sl. in the Río Prat valley and at a similar elevation by the glacier that still occupied the Puerto Consuelo fjord (**Figure 9B**). A lower-altitude ice tongue in Río Serrano Valley (B_3 in **Figures 2A**, **9A**), at least 25 m a.s.l. along the western outflow of Lago del Toro, would have also been necessary to create an ice-dammed palaeolake in contact with the SPI (Marden and Clapperton, 1995; Garcia et al., 2014).

Lago Pato is bounded topographically at ~40–50 m a.s.l. to the south and east and by a broad, undated (probably ACR) moraine complex that runs parallel with the present-day southern shoreline of the Bahía del Bote section of Lago del Toro to the northeast and west (**Figure 2A**). As Lago Pato was topographically constrained to the north and east (>~45 m a.s.l.) and the wetlands and the retaining sill to the south are at a much lower elevation (32–33 m a.s.l.; **Table 1**), the c. 13.4–13.0 ka lake drainage event, near the end of the ACR, would have passed through the Lago Porteño-Río Prat valley, rather than directly over Lago Pato (**Figure 9B**). A lower altitude palaeolake implied by the presence of shallow subaquatic macrofossils in the Lago Pato LP16 record is supported by a lack of glaciolacustrine deposits above 100 m a.s.l. younger than 16.8 cal ka BP in the Última Esperanza–Puerto Consuelo fjords.

As the core SWW belt migrated equatorward past 51°S during the ACR, outlet glaciers were maintained in relatively advanced positions in TdP (Bertrand et al., 2017; Quade and Kaplan, 2017; Fletcher et al., 2021) (**Figures 10B,D**). The southward movement of the SWW back past 51°S after the ACR continued poleward until c. 12 ka (Quade and Kaplan, 2017; McCulloch et al., 2020) and likely drove down precipitation levels, leading to the removal of high-altitude ice dams that had maintained palaeolake Tehuelche-Puerto Consuelo >100 m a.s.l. (**Figures 10B,D**)

The second reduction in lake level to between ~30 and 40 m a.s.l. at c. 11.7 cal ka BP isolated Lago Pato from Lago del Toro, cutting off the glaciolacustrine sediment supply from erosion of the TdP massif. An enlarged Lago del Toro had remained topographically dammed up to ~50 m a.s.l. along the Río Prat valley until low-level ice dams <~40–50 m a.s.l. in the Puerto-Consuelo fjord area most likely failed. This phase of lake regression is consistent with the minimum age for organic sedimentation of 10.3 ka from the Pantano Antonio Varas lake record at ~25 m a.s.l. and a ~30 m terrace constraining ice-dammed lake regression on the southern peninsula of Puerto Consuelo Fjord (Sagredo et al., 2011) (**Figure 2A**).

5.2.3 Early-Mid Holocene (11.7–5.6 ka)

The isolation of Lago Pato from Lago del Toro at the start of Unit 5A, c. 11.7 cal ka BP, is marked by a shift to a shallower lake system dominated by organic-rich lake muds and littoral vegetation. The time period covered by the zonally coherent

Early Holocene Westerlies Minimum (EHWM: 11.5–7.5 ka; Moreno et al., 2021) is initially characterised by greater stability in the littoral environment of Lago Pato between c. 11.7 and 10.1 ka, with exceptionally elevated Fe/Mn during the 'Anoxic Crisis' phase (**Figure 10G**) and possible peat formation over the LP16 site. Two early Holocene erosional contacts, between Units 1 and 6 at c. 10 ka and at the boundary between Units 5B-2 and 5B-3 at c. 8.9–8.6 ka in LP08 (**Figures 5A**, **6A**), coincide with increased oxidation in LP16 sediments (downward arrows 3 and 4 in **Figure 10F**), suggesting a highly variable lake level, fluctuating at or near the height of the retaining sill during the early Holocene, with occasional flushing through the depocentre (**Figures 5**, **6**, **8**, **9B**, **10F**).

At the start of the Holocene, glaciers along the SPI retreated rapidly to close to their present-day, land-locked, limits, as evidenced by moraines preserved in Río Serrano area ~30 km west of Lago Pato with cosmogenic surface exposure isotope ages of 11.3–10.7 cal ka BP (location C in **Figure 2B**) (Marden and Clapperton, 1995; Solari et al., 2012; Aniya, 2013). Similar to nearby lake studies (e.g., Lago Cipreses; **Figure 10F**) (Moreno et al., 2018), we found no evidence of further glacier readvances over Lago Pato during the Holocene.

New data from Lago Pato are consistent with the timing of 1) forest expansion in and around Última Esperanza from c. 11.9 cal ka BP onwards (Moreno et al., 2012; Moreno and Videla, 2016; Moreno et al., 2018; McCulloch et al., 2021; Moreno et al., 2021); 2) regional fjord deglaciation (Bertrand et al., 2017); and 3) regional pollen and lacustrine records from 52 to 55°S (Zolitschka et al., 2018; McCulloch et al., 2020; Moreno et al., 2021). Increasingly arid conditions (linked to falling lake levels) have been found in several early Holocene terrestrial records from Southern Patagonia (Moreno et al., 2012; Zolitschka et al., 2013; Moreno et al., 2018; Zolitschka et al., 2018; Reynhout et al., 2019; McCulloch et al., 2020; Moreno et al., 2021) and in the wider sub-Antarctic region, for example, Macquarie Island at 54°S in the Southern Ocean (Saunders et al., 2018) (**Figures 10C,F,G,I,J**).

During the transition into the Holocene, the core SWW belt remained strong and possibly more poleward-shifted but weaker at its northern margins (Toggweiler et al., 2006; Toggweiler and Russell, 2008; Quade and Kaplan, 2017; Moreno et al., 2021). This drove down moisture leading to deglaciation in Patagonia (Quade and Kaplan, 2017; Moreno et al., 2018; Kaplan et al., 2020). A phase of exceptionally positive planetary radiative imbalance following the ACR between c. 12 and 9 ka (Baggenstos et al., 2019) (**Figure 10A**) and the shift to an increasing trend in summer insolation at 51°S from c. 10 ka (**Figure 10A**) likely resulted in the contraction of the polar vortex, leading to a poleward shift in the SWW and the prolonged period of positive SAM-like conditions between c. 11.5 and 10 ka (**Figure 10F**).

Continued lake regression at this time reflects the poleward limit of the SWW (~55°S) and/or a zonally coherent EHWM (11.5–7.5 ka) between 50 and 54°S (Saunders et al., 2018; Moreno et al., 2021) and is coupled with a prolonged phase of increasingly positive SAM-like conditions (**Figures 10B–G**) (Quade and Kaplan, 2017). Elevated conductivity in a lake record from Macquarie Island at the start of the Holocene, followed by a reduction in conductivity to a minimum between c. 11 and 10 ka, implies that a hemispheric poleward shift of the core SWW to the south of ~54°S could have occurred during the EHWM (Saunders et al., 2018). The removal of sediments at c. 10 ka from the Lago Pato depocentre (LP08) occurred as the SWW were starting to move equatorward once more from their most poleward position of the early Holocene (**Figure 10B**).

A return to glaciolacustrine sedimentation in Lago Pato at c. 8.9 ka implies an isolation breach, most likely due to a precipitation-driven refilling/flushing event during a regionally wetter phase (**Figure 6A**) (Moreno et al., 2018; Zolitschka et al., 2018), or a short-lived enlargement of Lago del Toro between c. 8.9 and 8.6 ka, possibly linked to glacier readvance, re-damming, and subsequent dam failure at the Río Serrano/Puerto Consuelo Fjord outlet (**Figure 2**, location B3). Both scenarios are consistent with the core SWW returning northward from ~55 to 60°S to ~51°S between c. 10 and 8 ka, bringing increased precipitation (**Figure 10B**) (Quade and Kaplan, 2017; Moreno et al., 2021). The increasing conductivity trend between c. 10 and 6 cal ka BP in a lake record from Macquarie Island (Saunders et al., 2018) suggests a potential hemispheric equatorward shift in the SWW back over ~54°S at this time.

All proxy evidence from Lago Pato points to more arid conditions with decadal-to-centennial-scale fluctuations in water column stability (redox) until c. 7.5 ka (**Figures 8**, **10G**). Lower lake levels in Lago Pato (below the overspill ridge limit of ~30–35 m a.s.l. into Lago del Toro) between 9.7 and 7 cal ka BP are broadly consistent with: 1) an extended period of 'extreme dryness' in the Laguna Potrok Aike, a closed basin ~175 km southeast of Lago Pato, which is not influenced by SPI glacial activity in an area where the local correlation between the present-day annual wind speed and precipitation is negative (Zolitschka et al., 2013) (**Figure 10C**); 2) pollen records from Isla Navarino, further south (54–55°S) (McCulloch et al., 2020); and 3) an the early Holocene dry period in Laguna Azul, south-eastern Patagonia (52°S), between c. 10.1 and 8.3 cal ka BP (Zolitschka et al., 2018). While higher lake levels at Potrok Aike during the EHWM time period have been associated with phases of an incursion of precipitation bearing Easterlies (Ariztegui et al., 2010), consistently drier conditions across all these records likely reflect the increasing trend in summer insolation over 50°S–55°S, the poleward migration of the core SWW belt south of 52°S, and/or phases of reduced Easterlies incursion into eastern Patagonia (Fletcher and Moreno, 2012; Saunders et al., 2018; Moreno et al., 2021) (**Figures 10A,B**). These interpretations have not yet been reconciled with generally wetter and windier conditions inferred from some records from the west coast of Patagonia (Lamy et al., 2010) and further north in Chile (Van Daele et al., 2016) during the early Holocene.

The Lago Pato pollen record is overwhelmingly dominated by forest taxa (mainly *Nothofagus* pollen) (**Figures 8**, **10G**, **Supplementary Figure S8**). Unlike nearby Lago Cipreses (Moreno et al., 2018) and similarly high-resolution pollen records further east (Mayr et al., 2007) and south (McCulloch et al., 2020), we found limited evidence of high frequency or rapid (climate-driven) variability in our pollen data during the

Holocene. The more highly resolved lacustrine redox proxies (e.g., Fe/Mn (anoxia) and Mn/Ti (oxidation)) display sub-millennial/centennial-scale variability. This is less well-defined than the centennial–millennial-scale periodicities in the Fe/Mn in the pre-Holocene LP08 record, but broadly similar to the variability found in pollen data produced by Moreno et al. (2018) from Lago Cipreses (~11 km WNW of Lago Pato), and some other SE Patagonian lakes (Zolitschka et al., 2018).

Several palaeorecords suggest that a highly variable precipitation regime existed in Patagonia well into the mid-Holocene (Mayr et al., 2007; Lamy et al., 2010; Moreno et al., 2018; Zolitschka et al., 2018). These include, for example, the occurrence of a grass steppe biome in a pollen record from Cerro Frías (Mancini, 2002; Mancini, 2009) and increased fire activity in the Río Rubens region (Huber et al., 2004). These two records were later re-evaluated, with periods of relatively high but extremely variable precipitation with extended periods of summer drought between c. 11 and 5.5 ka (Markgraf and Huber, 2010). Variable redox conditions in Lago Pato during the early–mid Holocene reflect changes in lake stability and are consistent with the variable precipitation and SAM regimes identified between c. 10.8 and 6.8 ka in the nearby Vega Ñandú (Villa-Martínez and Moreno, 2017) and Lago Cipreses lake records (Moreno et al., 2018) (**Figures 10C,F,G**). A period of increased early–mid Holocene variability is also consistent with an "erosive" interval found between c. 10.6 and 6.6 ka in the Lago Eberhard sediment core (Moreno et al., 2012), attributed to a lake low-stand, warmer/drier conditions, and a reduction in SWW influence over the TdP region and Patagonia more generally, between c. 10.4 and 7.5 ka either as the SWW migrated poleward again (after 8 ka) or when SWW zonal intensity declined (**Figure 10B**) (Quade and Kaplan, 2017; Moreno et al., 2021).

From c. 7.4 ka onwards, Lago Pato maintained an organic-rich depositional environment. Even in wetter periods, the maximum water level remained below the retaining sill at ~33 m a.s.l., forming an enlarged and more stable (increasingly more anoxic) palaeo-Lago Pato that most likely encompassed both the LP08 and LP16 core sites. This is evident in **Figure 8** and **Figure 10G** from increasing similarity between the PC1 and Fe/Mn profiles for both records from c. 7.4 ka onwards and supported by the greater prevalence of pollen and diatom species associated with wetter conditions and forest density from c. 7.7 ka (**Figures 8**, **9**, **10G**,H).

Wetter conditions after c. 7.4 ka are consistent with the expansion of humid-temperate closed forests dominated by mainly *Nothofagus* from c. 7.5 ka in lake records in the Última Esperanza Province and further south after c. 7 ka (McCulloch et al., 2020; Moreno et al., 2021). Progression to wetter and more stable conditions during the mid to late Holocene is also mirrored at localities of similar distances from the eastern flank of the Andes and in palaeo records across a W-E transect at ~51°S (**Figures 3**, **10**). A co-eval readvance of the Cordillera Darwin Ice Field occurred between c. 7.3 and 5.7 ka (Bertrand et al., 2017), with refilling of Laguna Potrok Aike accelerating after c. 7 ka (Zolitschka et al., 2013) (**Figure 10C**). The shift to a more closed forest, indicative of generally wetter conditions, also began at c. 7.7 ka in records from the eastern shore of Brazo Sur (Wille and Schäbitz, 2008; Markgraf and Huber, 2010), but it was delayed until c. 5.1 ka in the Vega Ñandú area (Villa-Martínez and Moreno, 2017). The establishment of a dense *Nothofagus* forest in the Vega Ñandú area also coincided with an abrupt decrease in fire frequency and a shift from minerotrophic to ombrotrophic bog taxa at Río Rubens after c. 5.5 ka (Huber et al., 2004). Increasingly wetter conditions in these records reflects generally wetter conditions in southern Patagonia and the more stable and equatorward expansion of the core SWW belt and more negative SAM-like conditions after c. 5.7 ka (**Figures 10B,F**) (Markgraf and Huber, 2010; Moreno et al., 2021). The transition from open to closed forests at Lago Pato coincided with rising temperatures between 60 and 90°S from 7.5 ka (Marcott et al., 2013) and the global 'Holocene thermal maximum' centred on 6.5–6.0 ka cal BP, which was 0.7°C warmer than the pre-industrial 19th Century (Kaufman et al., 2020) (**Figures 10H,M**).

5.2.4 Mid–Late Holocene (5.7–1.9 ka)

Greater hydrological stability with a more stable lake water column and increasing stratification in Lago Pato between c. 5.6 and 1.9 ka is shown by consistent C/N ratio values (**Figure 5A**), the increasing dominance of planktonic diatoms, which reflect progressively deeper water levels and a reduced littoral zone, and an increasingly anoxic trend (**Figures 5A**, **8**, **10G**, **Supplementary Figure S7**). For example, between c. 6.5 and 3.0 ka, heavily silicified planktonic diatom species (e.g., *Aulacoseira ambigua*, *Aulacoseira granulata* s.l., and *Cyclostephanos* cf. *patagonicus*) were relatively abundant, indicating more stable water levels (**Supplementary Figure S7**), yet turbulent mixing likely prevented these relatively heavy taxa from sinking out of the photic zone (Kilham and Kilham, 1975; Rioual et al., 2007). A concomitant gradual increase in *Discostella stelligera* s.l., a smaller euplanktonic diatom with an efficient nutrient uptake strategy, implies periodic stratification of the water column (**Supplementary Figure S7A**) (Rühland et al., 2003; Tolotti et al., 2007; Rühland et al., 2008; Winder et al., 2009). In TdP, Patagonian steppe pollen (mainly Poaceae), indicating drier conditions, was replaced by increasingly dominant *Nothofagus* pollen suggesting a more closed and dense forest.

The mid–late Holocene stabilisation of Lago Pato is consistent with cooler and wetter conditions at ~51°S that have been attributed to a relatively minor reduction and/or continued equatorward shift in the SWW north of ~51°S into the lower latitudes (**Figure 10B**) (Lamy et al., 2010; McCulloch et al., 2020; Moreno et al., 2021). The intensification of the SWW over southern Patagonia at this time is thought to have been modulated by an increasing trend in summer insolation and initiated at c. 7.5 ka (**Figure 10A**) by steepening the pole-to-equator temperature gradient (Lamy et al., 2010). This led to a cooling trend in the South Pacific Ocean (Lamy et al., 2010; Whitlock et al., 2017; Moreno et al., 2018), as well as increased sea-ice and reduced ocean productivity around Antarctica (Mayr et al., 2007; Peck et al., 2015).

Decadal (ENSO-like) to millennial–centennial-scale (SAM-like) variability in the SWW during the mid–late Holocene has been detected in several small and sensitive lake systems in Patagonia (Moreno et al., 2018; Reynhout et al., 2019). West of the Andes, wetter conditions are also thought to reflect the increased regional-seasonal variability in SWW intensity (Moreno et al., 2009a; Kilian and Lamy, 2012; Villa-Martínez and Moreno, 2017). Meanwhile, in the east, the equatorward shift in the SWW from c. 5.5 ka led to increasing lake levels as precipitation-laden frontal systems from the Atlantic became more dominant (Lamy et al., 2010; Zolitschka et al., 2013). The increased influence of the ENSO in the last four thousand years is thought to have contributed to minor readvances of glaciers across Southern Patagonia (Moreno et al., 2010; Fletcher and Moreno, 2012; Villa-Martínez and Moreno, 2017; Kaplan et al., 2020; McCulloch et al., 2020).

Between c. 5.6 and 1.9 ka, the proxy data from Lago Pato indicate that net annual precipitation-evaporation was broadly balanced (**Figure 8**, **Supplementary Figure S7**). Since 2010 CE, the wind strength in Patagonia has increased during summer, when the core SWW are more focussed and poleward shifted. As austral summer winds have strengthened over the last decade, the correlation between wind strength and precipitation over Lago Pato during the austral summer has become increasingly negative (r = 0, 1979–2010 CE; r = −0.2 to −0.4, 2007–2017 CE) (**Figures 4F,G**). In the austral winter, the SWW are more diffuse, with the core SWW belt driven slightly northwards as the jet stream moves into subtropical latitudes of about 30°S. This equatorward shift broadens and weakens, the core wind belt, particularly north of ~50°S (Garreaud et al., 2013; Bertrand et al., 2014; Fiers et al., 2019). As a result, winter precipitation is more intense further north of ~35°S (**Figure 4D**). At Lago Pato, the SWW have become marginally weaker and the correlation between wind and rainfall in the winter consistently positive (r = +0.4–0.6 in 2017) (**Figure 4H**). A similar scenario in autumn or winter during the mid–late Holocene would have resulted in higher amounts of precipitation and a well-mixed water column in Lago Pato. Less intense SWW and reduced precipitation during the austral summer would have led to smaller phytoplankton taxa blooms as more stable but nutrient-depleted conditions. For small lake systems such as Lago Pato in transitional locations between the Andes and eastern Patagonia, even a comparatively small net reduction in SWW and/or warmer temperatures in summer would result in a relatively more stable water column. Additionally, increased precipitation in winter (**Figure 4D**) would have maintained glaciers and a denser, more closed *Nothofagus* forest ecosystem. This kind of seasonal response has been inferred from pollen records elsewhere in Torres del Paine (Moreno et al., 2018) and from Isla Navarino at ~54–55°S (McCulloch et al., 2020).

5.2.5 Late Holocene–Recent (1.9–0 ka)

Shallower and more turbulent conditions in Lago Pato between c. 1.9 and 0.5 ka are marked by an increase in benthic diatoms in Diatom Zone 6, Mn/Ti ratios, indicating increased mixing and oxidation, and higher C/N values (**Figures 5A**, **8**, **Supplementary Figure S7**), reflecting a greater input of terrestrial material or a higher contribution of macrophytes to lake primary production (Duff and Smol, 1995). In sub-Arctic lakes, planktonic diatoms are rare or absent if the water level is less than 5 m deep (Karst-Riddoch et al., 2009). In Lago Pato, previously dominant planktonic taxa were replaced by c. 1.9 ka by assemblages composed of small chain-forming benthic/tychoplanktonic *Fragilariod* species. The latter are common during pioneering turbid and lower nutrient conditions (Bigler et al., 2003) and also occur in lakes with increased alkalinity (Wilson et al., 2012), longer winter lake ice-cover (Smol, 1983), and increased availability of aerophilic habitats (Van Dam et al., 1994).

While further studies are needed to understand the ecological preferences of *Fragilariod* species (Bennion et al., 2010), their abrupt development after c. 1.9 ka coincides with a decline in the total amount of stomatocysts mainly formed by euplanktonic chrysophytes (**Supplementary Figures S7A,B**). Increased wind-induced detachment from the littoral zone likely brought more benthic diatoms into suspension. Enlargement of the wetland area surrounding Lago Pato and its shallow benthic zone explains the continuous deposition of organic matter at the shallower/littoral LP16 core site throughout the Holocene. The presence of an extensive shallow wetland basin (LP16) with a deeper water zone (LP08) also explains the co-existence of planktonic and benthic diatom communities in the LP08 sediments. This culminated in the (re)deposition of a Sr-rich outwash sand layer (S) in LP08 at c. 1.4 ka and a dramatic increase in oxidation at the LP16 site in the last ~200 years, indicative of recent subaerial exposure of the littoral zone (**Figures 5A**, **8**, **10G**).

Declining biological productivity and total land pollen between c. 1.4 ka and the present day (**Figure 8**) were driven by predominantly negative SAM-like conditions at ~51°S between c. 2 and 0.5 ka in South America (**Figure 10F**) (Abram et al., 2014). The SAM was modulated by increasing SWW at ~51°S and an enhanced ENSO in this interval and, in particular, during the Medieval Climate Anomaly (MCA: c. 1–0.7 ka, 1,250–950 CE) (Mann et al., 2009; Abram et al., 2014). Changes linked to a warmer MCA in South America have been inferred from some (Moreno and Videla, 2016), but not all, records in the Última Esperanza region (Moreno et al., 2010; Villa-Martínez and Moreno, 2017; Moreno et al., 2018). The influence of the MCA is not well-represented in the Lago Pato data (**Figures 8**, **10G**).

In the last ~500 years, the *Nothofagus* forest cover remained relatively constant, while carbon and nitrogen content rose. The declining benthic diatom community suggests reduced levels of turbulence and catchment instability, consistent with 1) an equatorward shifted SWW during a 'post-MCA' phase of negative SAM-like conditions; 2) extreme cold 'events' in most Southern Hemisphere palaeorecords (Neukom et al., 2014); 3) minor glacier advances across the Patagonian Ice Field and the Northern Antarctic Peninsula (Reynhout et al., 2019; Kaplan et al., 2020; Simms et al., 2021); and 4) the Northern Hemisphere 'Little Ice Age' (0.55–0.25 ka, 1,400–1,700 CE) (Mann et al., 2009; Kaufman et al., 2020; Perren et al., 2020). European weed species,

such as *Plantago* and *Rumex acetosella*, became established in the Lago Pato catchment (**Figure 8**). These species are commonly found in other pollen records from Patagonia and relate to increased human activity, principally pastoral farming, which has converted much of the natural *Nothofagus* forest to a grass-steppe biome. Natural lake infilling processes combined with increased human activity in the TdP area could have led to increased macrophyte development and elevated lake sediment carbon and nitrogen levels observed in Lago Pato (>30% C and ~4% N, approximately double the mid-late Holocene mean N value). Recent increases in *Cyclotella meneghiniana* are also likely related to human-induced changes in the lake catchment (Van Dam et al., 1994), rather than (natural) lake ontogeny or warmer conditions.

6 CONCLUSION

We analysed two sediment core records from Lago Pato, a small lake basin located in a climatically transitional location east of the Andes and topographically separated from Lago del Toro in the Torres del Paine National Park, Southern Chile, to provide insights into changing glacier configurations, lake-level change, and climate-driven regional vegetation changes in the Última Esperanza region over the last ~30,000 years. Focussing on the last glacial-interglacial transition and Holocene parts of the well-preserved records, we undertook detailed geochemical, pollen, and diatom analysis to examine the relationship between changes in the lake level, water column stability, bottom water redox conditions, and precipitation-evaporation balance at the site.

We identified the following five evolutionary phases in the history of Lago Pato, which we link to deglaciation and palaeoenvironmental change in the Torres del Paine and Última Esperanza region and wider regional to global climate changes during the Late Glacial and Holocene:

1) <39 ka–13.4 ka: a deep proglacial lake encompassing Lago del Toro and Lago Pato, with evidence of decadal-centennial-scale redox variations, developed between the l-LGM ~38–30 cal ka BP and the g-LGM ~26–19 cal ka BP. This palaeolake was dammed by glacier ice >100 m thick along the Puerto Consuelo–Última Esperanza fjord to the south. Sediments dated between 20 and 13.4 ka were removed from the Lago Pato littoral record following a large lake drainage event near the end of the ACR.
2) <13.4–11.7 ka: lake levels over Lago Pato were lowered from >~100 m a.s.l. to ~40–50 m by two drainage events. The enlarged palaeolake became shallower as regional glaciers retreated and low altitude ice-dams in the Última-Esperanza fjord failed at c. 13.4 ka and c. 11.7 cal ka BP as the SWW shifted poleward south of 51°S after the ACR. Lago Pato was isolated from Lago del Toro at 11.7 ka by the second lake lowering event.
3) 11.7–5.6 ka: a stable, anoxic early Holocene shallow-littoral–terrestrial environment was replaced by an increasingly productive shallow-littoral and periodically oxidising lacustrine environment with a variable lake level. The presence of open *Nothofagus* forests and benthic diatom assemblages are consistent with regional aridity associated with more positive SAM-like conditions and poleward SWW south of ~51°S. Two refilling and flushing (erosional) events create a hiatus at c. 10 ka and a brief return to glaciolacustrine sedimentation at c. 8.6–8.4 ka in the LP08 depocentre record due to the enlargement of Lago del Toro as the SWW moved equatorward towards ~51°S between c. 10 and 8 ka. Lago Pato returned to an isolated and productive regime between 8.4 and 5.6 ka as the SWW shifted poleward, south of ~51°S again.
4) 5.6–1.9 ka: increasing stability and anoxia between c. 4.5 and 4 cal ka BP in Lago Pato is associated with an equatorward shift in the SWW back past ~51°S as negative SAM-like conditions prevailed during the mid–late Holocene.
5) 1.9–0 ka: a shallower subaqueous lacustrine phase in the depocentre with increased turbulence reflecting generally increased SWW in the second half of the late Holocene. In the last 500 years, reduced levels of turbulence and catchment instability reflect reduced or equatorward shifted SWW during the 'Little Ice Age' advance in TdP. Vegetational changes in recent centuries and decades most likely relate to increased pastoral farming and human activity in the Torres del Paine area.

DATA AVAILABILITY STATEMENT

The original contributions presented in the study are included in the article/**Supplementary Material**, further inquiries can be directed to the corresponding author. Data has been deposited in the NERC EDS UK Polar Data Centre (PDC) as follows: Bathymetric and lake chemistry data: https://doi.org/10.5285/D55D7619-3E07-41B0-929E-C9DA0A4B61AF; LP08 lake sediment record data: https://doi.org/10.5285/C75EA98B-080E-455E-A54F-A9E8CF07AA73; LP16 lake sediment record data: https://doi.org/10.5285/F85EE4EB-8918-4AA4-8E51-6C46F4C812CB; Time series data: https://doi.org/10.5285/6BD95602-F2E3-4968-8622-C4AEB71C214C. Code and data can be found at: https://github.com/stever60/Lago_Pato.

AUTHOR CONTRIBUTIONS

SR, RM, JE, SD, WN, and EV conceived the research questions, obtained funding, wrote the manuscript, constructed figures and tables, undertook XRF-CS, pollen, diatom analysis, analysed the data, and wrote code. MS and EvdeV identified diatoms and collected diatom samples. SR, MS, KH, JV, CD, EV, DH, and WV undertook fieldwork. SD, JE, and AW undertook laboratory and data analysis and helped construct figures. All authors edited and commented on the final manuscript.

FUNDING

This project was funded by the Natural Environment Research Council (NERC) through the British Antarctic Survey (BAS) and

an UGent BOF bilateral collaboration project. RMcC was supported by Programa Regional R17A10002 and R20F0002 (PATSER) ANID.

ACKNOWLEDGMENTS

We gratefully acknowledge the University of Magallanes (UMAG) and the University of Santiago (Carolina Diaz) for assistance with fieldwork; the NERC/SUERC AMS Radiocarbon Facility for providing initial range-finder radiocarbon dates; the NERC Isotope Geosciences Laboratory (NIGL, now National Environmental Isotope Facility, NEIF, at the British Geological Survey) and Melanie Lang for stable carbon isotope analysis; Aberystwyth University (David Kelly), Durham University (Neil Tunstall and Christopher Longley), and Edinburgh University (Chris Hayward) for the use of their core scanning and microprobe facilities and technical support. We also thank John Turner and Tony Phillips for assistance with ERA-INTERIM analysis; Chris Darvill, Neil Glasser, Mike Kaplan, and Patricio Moreno for access to their published datasets; and Mike Kaplan for permission to use and adapt the SAM-index diagram used in **Figure 10F**. We are grateful to the two reviewers for their constructive and insightful comments, which helped improve the manuscript.

SUPPLEMENTARY MATERIAL

The Supplementary Material for this article can be found online at: https://www.frontiersin.org/articles/10.3389/feart.2022.813396/full#supplementary-material

REFERENCES

Abram, N. J., Mulvaney, R., Vimeux, F., Phipps, S. J., Turner, J., and England, M. H. (2014). Evolution of the Southern Annular Mode during the Past Millennium. *Nat. Clim Change* 4, 564–569. doi:10.1038/nclimate2235

Aller, R. C., and Rude, P. D. (1988). Complete Oxidation of Solid Phase Sulfides by Manganese and Bacteria in Anoxic marine Sediments. *Geochimica et Cosmochimica Acta* 52, 751–765. doi:10.1016/0016-7037(88)90335-3

Altenberger, U., Oberhansli, R., Putlitz, B., and Wemmer, K. (2003). Tectonic controls and Cenozoic magmatism at the Torres del Paine, southern Andes (Chile, 51 degrees 10'S). *Revista Geologica De Chile* 30, 65–81. doi:10.4067/s0716-02082003000100005

Aniya, M. (2013). Holocene Glaciations of Hielo Patag¡oacute;nico (Patagonia Icefield), South America: A Brief Review. *Geochem. J.* 47, 97–105. doi:10.2343/geochemj.1.0171

Ariztegui, D., Gilli, A., Anselmetti, F. S., Goñi, R. A., Belardi, J. B., and Espinosa, S. (2010). Lake-level Changes in central Patagonia (Argentina): Crossing Environmental Thresholds for Lateglacial and Holocene Human Occupation. *J. Quat. Sci.* 25, 1092–1099. doi:10.1002/jqs.1352

Baggenstos, D., Häberli, M., Schmitt, J., Shackleton, S. A., Birner, B., Severinghaus, J. P., et al. (2019). Earth's Radiative Imbalance from the Last Glacial Maximum to the Present. *Proc. Natl. Acad. Sci. USA* 116, 14881–14886. doi:10.1073/pnas.1905447116

Barret, S. (2021). *Ggobi/Ggally*. v2.1.2. doi:10.5281/zenodo.5009047

Bennion, H., Sayer, C. D., and Tibby, J. (2010). "Diatoms as Indicators of Environmental Change in Shallow Lakes," in *The Diatoms: Applications for the Environmental and Earth Sciences*. Editors J. P. Smol and E. F. Stoermer. 2nd ed (Cambridge University Press), 152–173.

Bereiter, B., Shackleton, S., Baggenstos, D., Kawamura, K., and Severinghaus, J. (2018). Mean Global Ocean Temperatures during the Last Glacial Transition. *Nature* 553, 39–44. doi:10.1038/nature25152

Bertrand, S., Hughen, K., Sepúlveda, J., and Pantoja, S. (2014). Late Holocene Covariability of the Southern Westerlies and Sea Surface Temperature in Northern Chilean Patagonia. *Quat. Sci. Rev.* 105, 195–208. doi:10.1016/j.quascirev.2014.09.021

Bertrand, S., Lange, C. B., Pantoja, S., Hughen, K., Van Tornhout, E., and Wellner, J. S. (2017). Postglacial Fluctuations of Cordillera Darwin Glaciers (Southernmost Patagonia) Reconstructed from Almirantazgo Fjord Sediments. *Quat. Sci. Rev.* 177, 265–275. doi:10.1016/j.quascirev.2017.10.029

Bigler, C., Grahn, E., Larocque, I., Jeziorski, A., and Hall, R. (2003). Holocene Environmental Change at Lake Njulla (999 M Asl), Northern Sweden: a Comparison with Four Small Nearby Lakes along an Altitudinal Gradient. *J. Paleolimnology* 29, 13–29. doi:10.1023/a:1022850925937

Bishop, T. (2021). *itraxR: Itrax Data Analysis Tools*. Available at: https://CRAN.R-project.org/package=itraxR.

Blaauw, M., and Christen, J. A. (2011). Flexible Paleoclimate Age-Depth Models Using an Autoregressive Gamma Process. *Bayesian Anal.* 6, 457–474. doi:10.1214/ba/1339616472

Blunier, T., Schwander, J., Stauffer, B., Stocker, T., Dällenbach, A., Indermühle, A., et al. (1997). Timing of the Antarctic Cold Reversal and the Atmospheric CO2increase with Respect to the Younger Dryas Event. *Geophys. Res. Lett.* 24, 2683–2686. doi:10.1029/97gl02658

Bronk Ramsey, C. (2016). Development of the Radiocarbon Calibration Program. *Radiocarbon* 43, 355–363. doi:10.1017/s0033822200038212

Calvert, S. E., and Pedersen, T. F. (1996). Sedimentary Geochemistry of Manganese; Implications for the Environment of Formation of Manganiferous Black Shales. *Econ. Geology.* 91, 36–47. doi:10.2113/gsecongeo.91.1.36

Caniupán, M., Lamy, F., Lange, C. B., Kaiser, J., Kilian, R., Arz, H. W., et al. (2017). Holocene Sea-Surface Temperature Variability in the Chilean Fjord Region. *Quat. Res.* 82, 342–353.

Dam, H., Mertens, A., and Sinkeldam, J. (1994). A Coded Checklist and Ecological Indicator Values of Freshwater Diatoms from The Netherlands. *Neth. J. Aquat. Ecol.* 28, 117–133. doi:10.1007/bf02334251

Damman, A. W. H. (1978). Distribution and Movement of Elements in Ombrotrophic Peat Bogs. *Oikos* 30, 480–495. doi:10.2307/3543344

Darvill, C. M., Bentley, M. J., Stokes, C. R., Hein, A. S., and Rodés, Á. (2015). Extensive MIS 3 Glaciation in Southernmost Patagonia Revealed by Cosmogenic Nuclide Dating of Outwash Sediments. *Earth Planet. Sci. Lett.* 429, 157–169. doi:10.1016/j.epsl.2015.07.030

Davies, B. J., Darvill, C. M., Lovell, H., Bendle, J. M., Dowdeswell, J. A., Fabel, D., et al. (2020). The Evolution of the Patagonian Ice Sheet from 35 Ka to the Present Day (PATICE). *Earth-Science Rev.* 204, 103152. doi:10.1016/j.earscirev.2020.103152

Davies, S. J., Lamb, H. F., and Roberts, S. J. (2015). "Micro-XRF Core Scanning in Palaeolimnology: Recent Developments," in *Micro-XRF Studies of Sediment Cores*. Editors I. W. Croudace and R. G. Rothwell (Dordrecht: Springer Netherlands), 189–226. doi:10.1007/978-94-017-9849-5_7

Dee, D. P., Uppala, S. M., Simmons, A. J., Berrisford, P., Poli, P., Kobayashi, S., et al. (2011). The ERA-Interim Reanalysis: Configuration and Performance of the Data Assimilation System. *Q.J.R. Meteorol. Soc.* 137, 553–597. doi:10.1002/qj.828

Dickens, W. A., Kuhn, G., Leng, M. J., Graham, A. G. C., Dowdeswell, J. A., Meredith, M. P., et al. (2019). Enhanced Glacial Discharge from the Eastern Antarctic Peninsula since the 1700s Associated with a Positive Southern Annular Mode. *Sci. Rep.* 9, 14606. doi:10.1038/s41598-019-50897-4

Duff, K. E., and Smol, J. P. (1995). The Relationship of Chrysophycean Stomatocysts to Environmental Variables in Freshwater Lakes in British Columbia. *Can. J. Bot.* 73, 1097–1111. doi:10.1139/b95-119

Dunlea, A. G., Murray, R. W., Tada, R., Alvarez-Zarikian, C. A., Anderson, C. H., Gilli, A., et al. (2020). Intercomparison of XRF Core Scanning Results from Seven Labs and Approaches to Practical Calibration. *Geochem. Geophys. Geosystems* 21, e2020GC009248. doi:10.1029/2020gc009248

Echeverria, M. E., Sottile, G. D., Mancini, M. V., and Fontana, S. L. (2014). Nothofagus forest Dynamics and Palaeoenvironmental Variations during the Mid and Late Holocene, in Southwest Patagonia. *The Holocene* 24, 957–969. doi:10.1177/0959683614534742

Emile-Geay, J., Cane, M., Seager, R., Kaplan, A., and Almasi, P. (2007). El Niño as a Mediator of the Solar Influence on Climate. *Paleoceanography* 22, PA3210. doi:10.1029/2006pa001304

Evans, G., Augustinus, P., Gadd, P., Zawadzki, A., Ditchfield, A., and Hopkins, J. (2022). Millennial-scale Periodicities Associated with Changes in Wind Ansd Precipitation over the Last Glacial Cycle (Ca. 117 ± 8.5 Ka BP) Recorded in Sediments from Lake Kai Iwi, Northland, New Zealand. *Glob. Planet. Change* 208, 103688. doi:10.1016/j.gloplacha.2021.103688

Fiers, G., Bertrand, S., Van Daele, M., Granon, E., Reid, B., Vandoorne, W., et al. (2019). Hydroclimate Variability of Northern Chilean Patagonia during the Last 20 Kyr Inferred from the Bulk Organic Geochemistry of Lago Castor Sediments (45°S). *Quat. Sci. Rev.* 204, 105–118. doi:10.1016/j.quascirev.2018.11.015

Fletcher, M.-S., and Moreno, P. I. (2012). Have the Southern Westerlies Changed in a Zonally Symmetric Manner over the Last 14,000 Years? A Hemisphere-wide Take on a Controversial Problem. *Quat. Int.* 253, 32–46. doi:10.1016/j.quaint.2011.04.042

Fletcher, M.-S., Pedro, J., Hall, T., Mariani, M., Alexander, J. A., Beck, K., et al. (2021). Northward Shift of the Southern Westerlies during the Antarctic Cold Reversal. *Quat. Sci. Rev.* 271, 107189. doi:10.1016/j.quascirev.2021.107189

Fogwill, C. J., and Kubik, P. W. (2016). A glacial stage spanning the antarctic cold reversal in torres del paine (51°s), chile, based on preliminary cosmogenic exposure ages. *Geografiska Annaler: Ser. A, Phys. Geogr.* 87, 403–408. doi:10.1111/j.0435-3676.2005.00266.x

Force, E. R., and Cannon, W. F. (1988). Depositional Model for Shallow-marine Manganese Deposits Around Black Shale Basins. *Econ. Geology.* 83, 93–117. doi:10.2113/gsecongeo.83.1.93

Galili, T. (2021). *Dendextend: Extending 'dendrogram' Functionality in R*. Available at: https://cran.r-project.org/package=dendextend.

García, J.-L., Hall, B. L., Kaplan, M. R., Vega, R. M., and Strelin, J. A. (2014). Glacial geomorphology of the Torres del Paine region (southern Patagonia): Implications for glaciation, deglaciation and paleolake history. *Geomorphology* 204, 599–616.

García, J.-L., Hein, A. S., Binnie, S. A., Gómez, G. A., González, M. A., and Dunai, T. J. (2018). The MIS 3 maximum of the Torres del Paine and Última Esperanza ice lobes in Patagonia and the pacing of southern mountain glaciation. *Quat. Sci. Rev.* 185, 9–26.

García, J. L., Kaplan, M. R., Hall, B. L., Schaefer, J. M., Vega, R. M., Schwartz, R., et al. (2012). Glacier Expansion in Southern Patagonia throughout the Antarctic Cold Reversal. *Geology* 40, 859–862.

Garreaud, R. D., Vuille, M., Compagnucci, R., and Marengo, J. (2009). Present-day South American Climate. *Palaeogeogr. Palaeoclimatol. Palaeoecol.* 281, 180–195. doi:10.1016/j.palaeo.2007.10.032

Garreaud, R., Lopez, P., Minvielle, M., and Rojas, M. (2013). Large-Scale Control on the Patagonian Climate. *J. Clim.* 26, 215–230. doi:10.1175/jcli-d-12-00001.1

Glasser, N. F., Jansson, K. N., Goodfellow, B. W., De Angelis, H., Rodnight, H., and Rood, D. H. (2017). Cosmogenic Nuclide Exposure Ages for Moraines in the Lago San Martin Valley, Argentina. *Quat. Res.* 75, 636–646. doi:10.1016/j.yqres.2010.11.005

Glasser, N. F., Jansson, K. N., Harrison, S., and Kleman, J. (2008). The Glacial Geomorphology and Pleistocene History of South America between 38°S and 56°S. *Quat. Sci. Rev.* 27, 365–390. doi:10.1016/j.quascirev.2007.11.011

Grinsted, A., Moore, J. C., and Jevrejeva, S. (2004). Application of the Cross Wavelet Transform and Wavelet Coherence to Geophysical Time Series. *Nonlin. Process. Geophys.* 11, 561–566. doi:10.5194/npg-11-561-2004

Guerrero, J. M., and Echenique, R. O. (2002). Cyclostephanos Patagonicussp. Nov., a New Freshwater Diatom from Western Patagonia (Argentina). *Diatom Res.* 17, 141–151. doi:10.1080/0269249x.2002.9705535

Gunn, D. E., and Best, A. I. (1998). A New Automated Nondestructive System for High Resolution Multi-Sensor Core Logging of Open Sediment Cores. *Geo-Marine Lett.* 18, 70–77. doi:10.1007/s003670050054

Heiri, O., Lotter, A. F., and Lemcke, G. (2001). Loss on Ignition as a Method for Estimating Organic and Carbonate Content in Sediments: Reproducibility and Comparability of Results. *J. Paleolimnology* 25, 101–110. doi:10.1023/a:1008119611481

Henríquez, C. A., Moreno, P. I., Dunbar, R. B., and Mucciarone, D. A. (2021). The Last Glacial Termination in Northwestern Patagonia Viewed from the Lago Fonk (~40°S) Record. *Quat. Sci. Rev.* 271, 107197.

Hodgson, D. A., Roberts, S. J., Bentley, M. J., Carmichael, E. L., Smith, J. A., Verleyen, E., et al. (2009). Exploring Former Subglacial Hodgson Lake, Antarctica. Paper II: Palaeolimnology. *Quat. Sci. Rev.* 28, 2310–2325. doi:10.1016/j.quascirev.2009.04.014

Hodgson, D. A., and Sime, L. C. (2010). Southern Westerlies and CO2. *Nat. Geosci* 3, 666–667. doi:10.1038/ngeo970

Hogg, A. G., Heaton, T. J., Hua, Q., Palmer, J. G., Turney, C. S., Southon, J., et al. (2020). SHCal20 Southern Hemisphere Calibration, 0-55,000 Years Cal BP. *Radiocarbon* 62, 759–778. doi:10.1017/rdc.2020.59

Hogg, A. G., Hua, Q., Blackwell, P. G., Niu, M., Buck, C. E., Guilderson, T. P., et al. (2016). SHCal13 Southern Hemisphere Calibration, 0-50,000 Years Cal BP. *Radiocarbon* 55, 1889–1903. doi:10.2458/azu_js_rc.55.16783

Huber, U. M., Markgraf, V., and Schäbitz, F. (2004). Geographical and Temporal Trends in Late Quaternary Fire Histories of Fuego-Patagonia, South America. *Quat. Sci. Rev.* 23, 1079–1097. doi:10.1016/j.quascirev.2003.11.002

Hughes, P. D., and Gibbard, P. L. (2015). A Stratigraphical Basis for the Last Glacial Maximum (LGM). *Quat. Int.* 383, 174–185. doi:10.1016/j.quaint.2014.06.006

Ineson, S., Maycock, A. C., Gray, L. J., Scaife, A. A., Dunstone, N. J., Harder, J. W., et al. (2015). Regional Climate Impacts of a Possible Future Grand Solar Minimum. *Nat. Commun.* 6, 7535. doi:10.1038/ncomms8535

Jouzel, J., Masson-Delmotte, V., Cattani, O., Dreyfus, G., Falourd, S., Hoffmann, G., et al. (2007). Orbital and Millennial Antarctic Climate Variability over the Past 800,000 Years. *Science* 317, 793–796. doi:10.1126/science.1141038

Juggins, S. (2007). *C2 Version 1.5 User Guide. Software for Ecological and Palaeoecological Data Analysis and Visualisation*. Newcastle: Newcastle University.

Juggins, S. (2012). *Rioja: Analysis of Quaternary Science Data, R Package Version*. 0.8-5.

Kaplan, M. R., Coronato, A., Hulton, N. R. J., Rabassa, J. O., Kubik, P. W., and Freeman, S. P. H. T. (2007). Cosmogenic Nuclide Measurements in Southernmost South America and Implications for Landscape Change. *Geomorphology* 87, 284–301. doi:10.1016/j.geomorph.2006.10.005

Kaplan, M. R., Fogwill, C. J., Sugden, D. E., Hulton, N. R. J., Kubik, P. W., and Freeman, S. P. H. T. (2008). Southern Patagonian Glacial Chronology for the Last Glacial Period and Implications for Southern Ocean Climate. *Quat. Sci. Rev.* 27, 284–294. doi:10.1016/j.quascirev.2007.09.013

Kaplan, M. R., Strelin, J. A., Schaefer, J. M., Peltier, C., Martini, M. A., Flores, E., et al. (2020). Holocene Glacier Behavior Around the Northern Antarctic Peninsula and Possible Causes. *Earth Planet. Sci. Lett.* 534, 116077. doi:10.1016/j.epsl.2020.116077

Karst-Riddoch, T. L., Malmquist, H. J., and Smol, J. P. (2009). Relationships between Freshwater Sedimentary Diatoms and Environmental Variables in Subarctic Icelandic Lakes. *fal* 175, 1–28. doi:10.1127/1863-9135/2009/0175-0001

Kaufman, D., Mckay, N., Routson, C., Erb, M., Davis, B., Heiri, O., et al. (2020). A Global Database of Holocene Paleotemperature Records. *Sci. Data* 7, 115. doi:10.1038/s41597-020-0445-3

Kilham, S. S., and Kilham, P. (1975). Melosira Granulata (Ehr.) RALFS: Morphology and Ecology of a Cosmopolitan Freshwater Diatom. *SIL Proc. 1922-2010* 19, 2716–2721. doi:10.1080/03680770.1974.11896368

Kilian, R., and Lamy, F. (2012). A Review of Glacial and Holocene Paleoclimate Records from Southernmost Patagonia (49-55°S). *Quat. Sci. Rev.* 53, 1–23. doi:10.1016/j.quascirev.2012.07.017

Kirschvink, J. L., and Chang, S.-B. R. (1984). Ultrafine-grained Magnetite in Deep-Sea Sediments: Possible Bacterial Magnetofossils. *Geol* 12, 559–562. doi:10.1130/0091-7613(1984)12<559:umidsp>2.0.co;2

Kylander, M. E., Ampel, L., Wohlfarth, B., and Veres, D. (2011). High-resolution X-ray Fluorescence Core Scanning Analysis of Les Echets (France) Sedimentary Sequence: New Insights from Chemical Proxies. *J. Quat. Sci.* 26, 109–117. doi:10.1002/jqs.1438

Lamy, F., Kilian, R., Arz, H. W., Francois, J.-P., Kaiser, J., Prange, M., et al. (2010). Holocene Changes in the Position and Intensity of the Southern westerly Wind belt. *Nat. Geosci* 3, 695–699. doi:10.1038/ngeo959

Landschützer, P., Gruber, N., and Bakker, D. C. E. (2016). Decadal Variations and Trends of the Global Ocean Carbon Sink. *Glob. Biogeochem. Cycles* 30, 1396–1417.

Laskar, J., Robutel, P., Joutel, F., Gastineau, M., Correia, A. C. M., and Levrard, B. (2004). A Long-Term Numerical Solution for the Insolation Quantities of the Earth. *A&A* 428, 261–285. doi:10.1051/0004-6361:20041335

Le Quéré, C., Rödenbeck, C., Buitenhuis, E. T., Conway, T. J., Langenfelds, R., Gomez, A., et al. (2007). Saturation of the Southern Ocean CO2 Sink Due to Recent Climate Change. *Science* 316, 1735–1738. doi:10.1126/science.1136188

Löwemark, L., Chen, H. F., Yang, T. N., Kylander, M., Yu, E. F., Hsu, Y. W., et al. (2011). Normalizing XRF-Scanner Data: A Cautionary Note on the Interpretation of High-Resolution Records from Organic-Rich Lakes. *J. Asian Earth Sci.* 40, 1250–1256.

Mancini, M. V. (2009). Holocene Vegetation and Climate Changes from a Peat Pollen Record of the forest - Steppe Ecotone, Southwest of Patagonia (Argentina). *Quat. Sci. Rev.* 28, 1490–1497. doi:10.1016/j.quascirev.2009.01.017

Mancini, M. V. (2002). Vegetation and Climate during the Holocene in Southwest Patagonia, Argentina. *Rev. Palaeobotany Palynology* 122, 101–115. doi:10.1016/s0034-6667(02)00105-7

Mann, M. E., Zhang, Z., Rutherford, S., Bradley, R. S., Hughes, M. K., Shindell, D., et al. (2009). Global Signatures and Dynamical Origins of the Little Ice Age and Medieval Climate Anomaly. *Science* 326, 1256–1260. doi:10.1126/science.1177303

Marcott, S. A., Shakun, J. D., Clark, P. U., and Mix, A. C. (2013). A Reconstruction of Regional and Global Temperature for the Past 11,300 Years. *Science* 339, 1198–1201. doi:10.1126/science.1228026

Marden, C. J., and Clapperton, C. M. (1995). Fluctuations of the South Patagonian Ice-Field during the Last Glaciation and the Holocene. *J. Quat. Sci.* 10, 197–209. doi:10.1002/jqs.3390100302

Markgraf, V., and Huber, U. M. (2010). Late and postglacial vegetation and fire history in Southern Patagonia and Tierra del Fuego. *Palaeogeogr. Palaeoclimatol. Palaeoecol.* 297, 351–366. doi:10.1016/j.palaeo.2010.08.013

Marshall, G. J. (2007). Half-century Seasonal Relationships between the Southern Annular Mode and Antarctic Temperatures. *Int. J. Climatol.* 27, 373–383. doi:10.1002/joc.1407

Marshall, G. J. (2003). Trends in the Southern Annular Mode from Observations and Reanalyses. *J. Clim.* 16, 4134–4143. doi:10.1175/1520-0442(2003)016<4134:titsam>2.0.co;2

Marshall, J., and Speer, K. (2012). Closure of the Meridional Overturning Circulation through Southern Ocean Upwelling. *Nat. Geosci* 5, 171–180. doi:10.1038/ngeo1391

Mayr, C., Lücke, A., Wagner, S., Wissel, H., Ohlendorf, C., Haberzettl, T., et al. (2013). Intensified Southern Hemisphere Westerlies Regulated Atmospheric CO2 during the Last Deglaciation. *Geology* 41, 831–834. doi:10.1130/g34335.1

Mayr, C., Wille, M., Haberzettl, T., Fey, M., Janssen, S., Lucke, A., et al. (2007). Holocene Variability of the Southern Hemisphere Westerlies in Argentinean Patagonia (52°S). *Quat. Sci. Rev.* 26, 579–584. doi:10.1016/j.quascirev.2006.11.013

Mcculloch, R. D., Bentley, M. J., Tipping, R. M., and Clapperton, C. M. (2005). Evidence for Late-Glacial Ice Dammed Lakes in the central Strait of Magellan and Bahía Inútil, Southernmost South america. *Geografiska Annaler: Ser. A, Phys. Geogr.* 87, 335–362. doi:10.1111/j.0435-3676.2005.00262.x

Mcculloch, R. D., Blaikie, J., Jacob, B., Mansilla, C. A., Morello, F., De Pol-Holz, R., et al. (2020). Late Glacial and Holocene Climate Variability, Southernmost Patagonia. *Quat. Sci. Rev.* 229, 106131. doi:10.1016/j.quascirev.2019.106131

Mcculloch, R. D., and Davies, S. J. (2001). Late-glacial and Holocene Palaeoenvironmental Change in the central Strait of Magellan, Southern Patagonia. *Palaeogeogr. Palaeoclimatol. Palaeoecol.* 173, 143–173. doi:10.1016/s0031-0182(01)00316-9

Mcculloch, R. D., Mansilla, C. A., Martin, F., Borrero, L., Staff, R. A., and Tisdall, E. W. (2021). The Nature and Timing of Landscape Change at Cerro Benítez, Última Esperanza, Southern Patagonia (52°S): New Insights into the History of Megafaunal Extinctions and Human Occupation. *Quat. Int.* 601, 116–129. doi:10.1016/j.quaint.2021.07.018

Melles, M., Brigham-Grette, J., Minyuk, P. S., Nowaczyk, N. R., Wennrich, V., Deconto, R. M., et al. (2012). 2.8 Million Years of Arctic Climate Change from Lake El'gygytgyn, NE Russia. *Science* 337, 315–320. doi:10.1126/science.1222135

Monnin, E., Indermühle, A., Dällenbach, A., Flückiger, J., Stauffer, B., Stocker, T. F., et al. (2001). Atmospheric CO 2 Concentrations over the Last Glacial Termination. *Science* 291, 112–114. doi:10.1126/science.291.5501.112

Moore, P. D., Webb, J. A., and Collinson, M. E. (1991). *Pollen Analysis*. Blackwell Scientific Publications.

Moreno, A., Giralt, S., Valero-Garcés, B., Sáez, A., Bao, R., Prego, R., et al. (2007). A 14kyr Record of the Tropical Andes: The Lago Chungará Sequence (18°S, Northern Chilean Altiplano). *Quat. Int.* 161, 4–21. doi:10.1016/j.quaint.2006.10.020

Moreno, P. I., Francois, J. P., Moy, C. M., and Villa-Martínez, R. (2010). Covariability of the Southern Westerlies and Atmospheric CO2 during the Holocene. *Geology* 38, 727–730. doi:10.1130/g30962.1

Moreno, P. I., François, J. P., Villa-Martínez, R. P., and Moy, C. M. (2009a). Millennial-scale Variability in Southern Hemisphere westerly Wind Activity over the Last 5000 Years in SW Patagonia. *Quat. Sci. Rev.* 28, 25–38. doi:10.1016/j.quascirev.2008.10.009

Moreno, P. I., Henríquez, W. I., Pesce, O. H., Henríquez, C. A., Fletcher, M. S., Garreaud, R. D., et al. (2021). An Early Holocene westerly Minimum in the Southern Mid-latitudes. *Quat. Sci. Rev.* 251, 106730. doi:10.1016/j.quascirev.2020.106730

Moreno, P. I., Kaplan, M. R., François, J. P., Villa-Martínez, R., Moy, C. M., Stern, C. R., et al. (2009b). Renewed Glacial Activity during the Antarctic Cold Reversal and Persistence of Cold Conditions until 11.5 Ka in Southwestern Patagonia. *Geology* 37, 375–378. doi:10.1130/g25399a.1

Moreno, P. I. (2020). Timing and Structure of Vegetation, Fire, and Climate Changes on the Pacific Slope of Northwestern Patagonia since the Last Glacial Termination. *Quat. Sci. Rev.* 238, 106328. doi:10.1016/j.quascirev.2020.106328

Moreno, P. I., and Videla, J. (2016). Centennial and Millennial-Scale Hydroclimate Changes in Northwestern Patagonia since 16,000 Yr BP. *Quat. Sci. Rev.* 149, 326–337. doi:10.1016/j.quascirev.2016.08.008

Moreno, P. I., Vilanova, I., Villa-Martínez, R., Dunbar, R. B., Mucciarone, D. A., Kaplan, M. R., et al. (2018). Onset and Evolution of Southern Annular Mode-like Changes at Centennial Timescale. *Sci. Rep.* 8, 3458. doi:10.1038/s41598-018-21836-6

Moreno, P. I., Vilanova, I., Villa-Martínez, R., Garreaud, R. D., Rojas, M., and De Pol-Holz, R. (2014). Southern Annular Mode-like Changes in Southwestern Patagonia at Centennial Timescales over the Last Three Millennia. *Nat. Commun.* 5, 4375. doi:10.1038/ncomms5375

Moreno, P. I., Villa-Martínez, R., Cárdenas, M. L., and Sagredo, E. A. (2012). Deglacial Changes of the Southern Margin of the Southern westerly Winds Revealed by Terrestrial Records from SW Patagonia (52°S). *Quat. Sci. Rev.* 41, 1–21. doi:10.1016/j.quascirev.2012.02.002

Mulvaney, R., Abram, N. J., Hindmarsh, R. C. A., Arrowsmith, C., Fleet, L., Triest, J., et al. (2012). Recent Antarctic Peninsula Warming Relative to Holocene Climate and Ice-Shelf History. *Nature* 489, 141–144. doi:10.1038/nature11391

Neukom, R., Gergis, J., Karoly, D. J., Wanner, H., Curran, M., Elbert, J., et al. (2014). Inter-hemispheric Temperature Variability over the Past Millennium. *Nat. Clim. Change* 4, 362–367. doi:10.1038/nclimate2174

Oksanen, J. (2014). *Vegan: Community Ecology Package*. R package version 2.3-0Available at: http://cran.r-project.org/web/packages/vegan/index.html.

Paillard, D., Labeyrie, L., and Yiou, P. (1996). Macintosh Program Performs Time-Series Analysis. *Eos Trans. AGU* 77, 379. doi:10.1029/96eo00259

Palacios, D., Stokes, C. R., Phillips, F. M., Clague, J. J., Alcalá-Reygosa, J., Andrés, N., et al. (2020). The Deglaciation of the Americas during the Last Glacial Termination. *Earth-Science Rev.* 203, 103113. doi:10.1016/j.earscirev.2020.103113

Peck, V. L., Allen, C. S., Kender, S., Mcclymont, E. L., and Hodgson, D. A. (2015). Oceanographic Variability on the West Antarctic Peninsula during the Holocene and the Influence of Upper Circumpolar Deep Water. *Quat. Sci. Rev.* 119, 54–65. doi:10.1016/j.quascirev.2015.04.002

Perren, B. B., Hodgson, D. A., Roberts, S. J., Sime, L., Van Nieuwenhuyze, W., Verleyen, E., et al. (2020). Southward Migration of the Southern Hemisphere westerly Winds Corresponds with Warming Climate over Centennial Timescales. *Commun. Earth Environ.* 1, 58. doi:10.1038/s43247-020-00059-6

Pesce, O. H., and Moreno, P. I. (2014). Vegetation, fire and climate change in central-east Isla Grande de Chiloé (43°S) since the Last Glacial Maximum, northwestern Patagonia. *Quat. Sci. Rev.* 90, 143–157. doi:10.1016/j.quascirev.2014.02.021

Pirlet, H., Wehrmann, L. M., Brunner, B., Frank, N., Dewanckele, J., Van Rooij, D., et al. (2010). Diagenetic Formation of gypsum and Dolomite in a Cold-Water Coral mound in the Porcupine Seabight, off Ireland. *Sedimentology* 57, 786–805. doi:10.1111/j.1365-3091.2009.01119.x

Quade, J., and Kaplan, M. R. (2017). Lake-level Stratigraphy and Geochronology Revisited at Lago (Lake) Cardiel, Argentina, and Changes in the Southern Hemispheric Westerlies over the Last 25 Ka. *Quat. Sci. Rev.* 177, 173–188. doi:10.1016/j.quascirev.2017.10.006

Renberg, I. (1990). A Procedure for Preparing Large Sets of Diatom Slide from Sediment Cores. *J. Paleolimnology* 4, 87–90. doi:10.1007/bf00208301

Reynhout, S. A., Sagredo, E. A., Kaplan, M. R., Aravena, J. C., Martini, M. A., Moreno, P. I., et al. (2019). Holocene Glacier Fluctuations in Patagonia Are Modulated by Summer Insolation Intensity and Paced by Southern Annular Mode-like Variability. *Quat. Sci. Rev.* 220, 178–187. doi:10.1016/j.quascirev.2019.05.029

Rioual, P., Andrieu-Ponel, V., De Beaulieu, J.-L., Reille, M., Svobodova, H., and Battarbee, R. W. (2007). Diatom Responses to Limnological and Climatic Changes at Ribains Maar (French Massif Central) during the Eemian and Early Würm. *Quat. Sci. Rev.* 26, 1557–1609. doi:10.1016/j.quascirev.2007.03.009

Roberts, S. J., Monien, P., Foster, L. C., Loftfield, J., Hocking, E. P., Schnetger, B., et al. (2017). Past Penguin colony Responses to Explosive Volcanism on the Antarctic Peninsula. *Nat. Commun.* 8, 14914. doi:10.1038/ncomms14914

Rühland, K. M., Smol, J. P., and Pienitz, R. (2003). Ecology and Spatial Distributions of Surface-Sediment Diatoms from 77 Lakes in the Subarctic Canadian Treeline Region. *Can. J. Bot.* 81, 57–73.

Rühland, K., Paterson, A. M., and Smol, J. P. (2008). Hemispheric-scale Patterns of Climate-Related Shifts in Planktonic Diatoms from North American and European Lakes. *Glob. Change Biol.* 14, 2740–2754.

Rumrich, U., Lange-Bertalot, H., and Rumrich, M. (2000). *Diatoms of the Andes*. Königstein, Germany: Koeltz Scientific Books.

Sagredo, E. A., Moreno, P. I., Villa-Martínez, R., Kaplan, M. R., Kubik, P. W., and Stern, C. R. (2011). Fluctuations of the Última Esperanza Ice Lobe (52°S), Chilean Patagonia, during the Last Glacial Maximum and Termination 1. *Geomorphology* 125, 92–108. doi:10.1016/j.geomorph.2010.09.007

Saunders, K. M., Roberts, S. J., Perren, B., Butz, C., Sime, L., Davies, S., et al. (2018). Holocene Dynamics of the Southern Hemisphere westerly Winds and Possible Links to CO2 Outgassing. *Nat. Geosci* 11, 650–655. doi:10.1038/s41561-018-0186-5

Schittek, K., Forbriger, M., Mächtle, B., Schäbitz, F., Wennrich, V., Reindel, M., et al. (2015). Holocene Environmental Changes in the highlands of the Southern Peruvian Andes (14° S) and Their Impact on Pre-columbian Cultures. *Clim. Past* 11, 27–44. doi:10.5194/cp-11-27-2015

Schneider, C., Glaser, M., Kilian, R., Santana, A., Butorovic, N., and Casassa, G. (2013). Weather Observations across the Southern Andes at 53°S. *Phys. Geogr.* 24, 97–119. doi:10.2747/0272-3646.24.2.97

Shin, J., Ahn, J., Chowdhry Beeman, J., Lee, H. G., and Brook, E. J. (2021). Millennial Variations of Atmospheric CO2 during the Early Holocene (11.7–7.4 Ka). *Clim. Past Discuss.* 2021, 1–22.

Simms, A. R., Bentley, M. J., Simkins, L. M., Zurbuchen, J., Reynolds, L. C., Dewitt, R., et al. (2021). Evidence for a "Little Ice Age" Glacial advance within the Antarctic Peninsula - Examples from Glacially-Overrun Raised Beaches. *Quat. Sci. Rev.* 271, 107195. doi:10.1016/j.quascirev.2021.107195

Smol, J. P. (1983). Paleophycology of a High Arctic lake Near Cape Herschel, Ellesmere Island. *Can. J. Bot.* 61, 2195–2204. doi:10.1139/b83-238

Solari, M. A., Le Roux, J. P., Herve, F., Airo, A., and Calderon, M. (2012). Evolution of the Great Tehuelche Paleolake in the Torres del Paine National Park of Chilean Patagonia during the Last Glacial Maximum and Holocene. *Andean Geology.* 39, 1–21. doi:10.5027/andgeov39n1-a01

Spratt, R. M., and Lisiecki, L. E. (2016). A Late Pleistocene Sea Level Stack. *Clim. Past* 12, 1079–1092. doi:10.5194/cp-12-1079-2016

Steinhilber, F., Beer, J., and Fröhlich, C. (2009). Total Solar Irradiance during the Holocene. *Geophys. Res. Lett.* 36. doi:10.1029/2009gl040142

Sterken, M., Roberts, S. J., Hodgson, D. A., Vyverman, W., Balbo, A. L., Sabbe, K., et al. (2012). Holocene Glacial and Climate History of Prince Gustav Channel, Northeastern Antarctic Peninsula. *Quat. Sci. Rev.* 31, 93–111. doi:10.1016/j.quascirev.2011.10.017

Stevenson, R. J., Hill, B. H., Herlihy, A. T., Yuan, L. L., and Norton, S. B. (2008). Algae-P Relationships, Thresholds, and Frequency Distributions Guide Nutrient Criterion Development. *J. North Am. Benthological Soc.* 27, 783–799. doi:10.1899/07-077.1

Stockmarr, J. (1971). Tablets with Spores Used in Absolute Pollen Analysis. *Pollen et Spores* 13, 615–621.

Street-Perrott, F. A., Barker, P. A., Swain, D. L., Ficken, K. J., Wooller, M. J., Olago, D. O., et al. (2007). Late Quaternary Changes in Ecosystems and Carbon Cycling on Mt. Kenya, East Africa: a Landscape-Ecological Perspective Based on Multi-Proxy lake-sediment Influxes. *Quat. Sci. Rev.* 26, 1838–1860. doi:10.1016/j.quascirev.2007.02.014

Tjallingii, R., Röhl, U., Kölling, M., and Bickert, T. (2007). Influence of the Water Content on X-ray Fluorescence Core-Scanning Measurements in Soft marine Sediments. *Geochem. Geophys. Geosystems* 8. doi:10.1029/2006gc001393

Toggweiler, J. R., Russell, J. L., and Carson, S. R. (2006). Midlatitude Westerlies, Atmospheric CO2, and Climate Change during the Ice Ages. *Paleoceanography* 21, n/a. doi:10.1029/2005pa001154

Toggweiler, J. R., and Russell, J. (2008). Ocean Circulation in a Warming Climate. *Nature* 451, 286–288. doi:10.1038/nature06590

Tolotti, M., Corradini, F., Boscaini, A., and Calliari, D. (2007). Weather-driven Ecology of Planktonic Diatoms in Lake Tovel (Trentino, Italy). *Hydrobiologia* 578, 147–156. doi:10.1007/s10750-006-0441-4

Torres, M. E., Hong, W.-L., Solomon, E. A., Milliken, K., Kim, J.-H., Sample, J. C., et al. (2020). Silicate Weathering in Anoxic marine Sediment as a Requirement for Authigenic Carbonate Burial. *Earth-Science Rev.* 200, 102960. doi:10.1016/j.earscirev.2019.102960

Trauth, M. H. (2015). "Time-Series Analysis," in *MATLAB® Recipes for Earth Sciences*. Editor M. H. Trauth (Berlin, Heidelberg: Springer Berlin Heidelberg), 151–213. doi:10.1007/978-3-662-46244-7_5

Tuhkanen, S. (1992). The climate of Tierra del Fuego from a vegetation geographical point of view and its ecoclimatic counterparts elsewhere. *Acta Botanica Fennica* 145, 1–64.

Turney, C. S. M., Jones, R. T., Fogwill, C., Hatton, J., Williams, A. N., Hogg, A., et al. (2016). A 250-year Periodicity in Southern Hemisphere westerly Winds over the Last 2600 Years. *Clim. Past* 12, 189–200. doi:10.5194/cp-12-189-2016

Van Daele, M., Bertrand, S., Meyer, I., Moernaut, J., Vandoorne, W., Siani, G., et al. (2016). Late Quaternary Evolution of Lago Castor (Chile, 45.6°S): Timing of the Deglaciation in Northern Patagonia and Evolution of the Southern Westerlies during the Last 17 Kyr. *Quat. Sci. Rev.* 133, 130–146. doi:10.1016/j.quascirev.2015.12.021

Viaggi, P. (2021). Quantitative Impact of Astronomical and Sun-Related Cycles on the Pleistocene Climate System from Antarctica Records. *Quat. Sci. Adv.* 4, 100037. doi:10.1016/j.qsa.2021.100037

Villa-Martínez, R., and Moreno, P. I. (2017). Pollen Evidence for Variations in the Southern Margin of the westerly Winds in SW Patagonia over the Last 12,600 Years. *Quat. Res.* 68, 400–409.

Weltje, G. J., and Tjallingii, R. (2008). Calibration of XRF Core Scanners for Quantitative Geochemical Logging of Sediment Cores: Theory and Application. *Earth Planet. Sci. Lett.* 274, 423–438. doi:10.1016/j.epsl.2008.07.054

Wennrich, V., Minyuk, P. S., Borkhodoev, V., Francke, A., Ritter, B., Nowaczyk, N. R., et al. (2014). Pliocene to Pleistocene Climate and Environmental History of Lake El'gygytgyn, Far East Russian Arctic, Based on High-Resolution Inorganic Geochemistry Data. *Clim. Past* 10, 1381–1399. doi:10.5194/cp-10-1381-2014

Whitlock, C., Moreno, P. I., and Bartlein, P. (2017). Climatic Controls of Holocene Fire Patterns in Southern South America. *Quat. Res.* 68, 28–36. doi:10.1016/j.yqres.2007.01.012

Wille, M., and Schäbitz, F. (2008). Late-glacial and Holocene Climate Dynamics at the Steppe/forest Ecotone in Southernmost Patagonia, Argentina: the Pollen

Record from a Fen Near Brazo Sur, Lago Argentino. *Veget Hist. Archaeobot* 18, 225–234. doi:10.1007/s00334-008-0194-2

Wilson, C. R., Michelutti, N., Cooke, C. A., Briner, J. P., Wolfe, A. P., and Smol, J. P. (2012). Arctic lake Ontogeny across Multiple Interglaciations. *Quat. Sci. Rev.* 31, 112–126. doi:10.1016/j.quascirev.2011.10.018

Winder, M., Reuter, J. E., and Schladow, S. G. (2009). Lake Warming Favours Small-Sized Planktonic Diatom Species. *Proc. R. Soc. B.* 276, 427–435. doi:10.1098/rspb.2008.1200

Wittkop, C., Swanner, E. D., Grengs, A., Lambrecht, N., Fakhraee, M., Myrbo, A., et al. (2020). Evaluating a Primary Carbonate Pathway for Manganese Enrichments in Reducing Environments. *Earth Planet. Sci. Lett.* 538, 116201. doi:10.1016/j.epsl.2020.116201

Yuan, X., and Yonekura, E. (2011). Decadal Variability in the Southern Hemisphere. *J. Geophys. Res. Atmospheres* 116. doi:10.1029/2011jd015673

Zolitschka, B., Anselmetti, F., Ariztegui, D., Corbella, H., Francus, P., Lücke, A., Maidana, N. I., Ohlendorf, C., Schäbitz, F., and Wastegård, S. (2013). Environment and climate of the last 51,000 years - new insights from the Potrok Aike maar lake Sediment Archive Drilling prOject (PASADO). *Quaternary Science Reviews* 71, 1–12. doi:10.1016/j.quascirev.2012.11.024

Zolitschka, B., Fey, M., Janssen, S., Maidana, N. I., Mayr, C., Wulf, S., Haberzettl, T., Corbella, H., Lücke, A., Ohlendorf, C., and Schäbitz, F. (2018). Southern Hemispheric Westerlies control sedimentary processes of Laguna Azul (south-eastern Patagonia, Argentina). *The Holocene* 29, 403–420. doi:10.1177/0959683618816446

Conflict of Interest: The authors declare that the research was conducted in the absence of any commercial or financial relationships that could be construed as a potential conflict of interest.

Publisher's Note: All claims expressed in this article are solely those of the authors and do not necessarily represent those of their affiliated organizations or those of the publisher, the editors, and the reviewers. Any product that may be evaluated in this article, or claim that may be made by its manufacturer, is not guaranteed or endorsed by the publisher.